Imperial College London

Department of Materials

Effects of Processing on Microstructure and Indentation Response of AlN doped SiC

Naeem Ur-Rehman

January 22, 2012

Submitted in part fulfilment of the requirements for the degree of

Doctor of Philosophy in Department of Materials

Imperial College London

Declaration

I herewith certify that all material in this dissertation which is not my own work has been properly acknowledged.

Naeem Ur-Rehman

Abstract

Sintering of silicon carbide (SiC) requires high temperature and pressure due to the covalent nature of its bonding. Therefore, sintering additives are used to lower the sintering temperature and to control the microstructure.

In this work, role of aluminium nitride (AlN) and carbon in pressure assisted densification is studied as the literature was not clear on whether AlN always induces liquid phase sintering (LPS). It is shown that mixing suffices to produce green bodies in which AlN is present as individual particles. When heated above 1700 °C the AlN redistributes to grain boundaries and triple junctions through vapour transport and grain boundary diffusion, which causes the onset of densification. Addition of AlN and carbon together leads to microstructure more consistent with solid state sintering (SSS) than with LPS which was induced with the addition of yttria and AlN.

Nano-indentation was used to measure hardness as a function of strain rate and temperature. It was found that hardness increases 0.8 GPa per decade strain rate and decreases with increasing temperature. Since in the absence of cracking hardness is a function of

stiffness and yield stress, nano-indentation was used to calculate the Peierls stress (12 $\pm$ 1 GPa), activation energy (1.1 $\pm$ 0.3 eV) and the activation volume (1.44×10^{-29} m^3) of dislocation glide in SiC. Grain size was found to have a minimal effect on plasticity of the material when indents are small.

Consistent with widely reported trends, the hardness was found to decrease when higher loads are used. It is argued that this decrease in hardness is due to an increase in crack length relative to the indent size. An empirical model, based on dimensional analysis, describes the observed decrease in hardness rather well.

Observations of a new damage mechanism after unloading of large load indents are presented and a mechanism is proposed.

in the loving memory of

my late grandfather

Mr. Hafiz Saif-Ur-Rehman (1930 – 2010)

Acknowledgments

First of all, I would like to acknowledge my parents for their love, continuous support and help. I would never have been able to achieve so much without you. I would like to thank my supervisors, Dr. Luc Vandeperre, Professor Bill Lee and Professor Peter Brown for all the help, motivation and support. Luc has been incredible in the amount of time he dedicated towards me. I dont remember a time when I needed his help and he was not there. That includes the time for even a friendly chat to take my mind off work. Professor Lees critical analysis of my work kept me on my toes throughout my PhD. Special thanks for reading my thesis (with the magnifying glass) to spot every irregularity that there was. I really learnt a lot from it. I would have had a very boring PhD if Peter was not around. All those crazy ideas that we discussed will one day be tried hopefully. I still remember your first advice to me that Common sense is your worst enemy. My teachers in Pakistan Mr. Zafar Abbas, Mr. Tahir Hussain and Mr. Zafar Iqbal are thanked for making me believe in myself.

I would also like to acknowledge the excellent groups of both Professor Bill Lee and Dr. Luc Vandeperre. The help of Drs. Rafael Sa, Doni Daniel and Vineet Bhakhri is highly appreciated. My friend and office neighbour Jianye (David) Wang has provided me lots of help with academic and non academic stuff i.e. Photography of some events as well as countless and endless discussions about the possible release date and features of whatever the late Steve Jobs was deciding to launch next.

You will be glad to know that my conversion has been complete from PC to mac as I am planning to buy the big machine soon (after getting robbed off my beloved iPhone and Macbook Pro). I would also like to thank Tayyab Subhani for so many detailed discussions on indentation size effects and fracture toughness. The help of Constantin Ciurea is appreciated however; I am still not convinced that the moon landing was faked.

I would also like to acknowledge those idiot robbers who snatched my laptop a day before submission and hence made me go through my thesis once again. I found so many small mistakes that otherwise would have gone undetected. So thank you too!

My special thanks to all the technical staff at Imperial. Dr. Mahmoud Ardakani, Mr. Richard Chater, Mr. Richard Sweeney, Mr. Benjamin Chan, Mr Garry Stakalls, Dr Ivelin Valkov, and Mrs Ecaterina Ware all helped me a great deal.

My friends are part of my strong support network. Mutahir (The macromaster, your help with excel is highly appreciated) Faizan (the Bureaucrat), Ammar (the politician), Raju (Cheers for help with Matlab), Sara, Sana (An URDU loving doctor), Rumeza (cheers for proof reading my Literature Review just a couple of days after passing your own viva) and Mariam (for being such a great friend, reading my thesis over and over again and providing me great advice whenever I got into trouble) are only a few to name. You deserve special mention for all the great times that we had together. Even the bad and stressful days in your company were fun.

Ahsan: I am so lucky to have you as my friend and brother. Your valuable advice and selfless support kept me going even in the darkest of the days.

A man looses hope when he has no one to turn to for support. I never lost hope as I had a brilliant support network including my parents, friends, work colleagues and supervisors. Thank you all.

Contents

1. Introduction **36**

2. Literature Review **39**

2.1. Effects of processing on the microstructure of SiC . . . 39

2.1.1. Boron, carbon and aluminium as sintering additives 40

2.1.2. Alumina, yttria and silica as sintering additives 50

2.1.3. Use of aluminium nitride (AlN) as a sintering additive 54

2.1.4. Effects of sintering schedule on sintering and microstructure of SiC 61

2.2. Use of indentation tests to measure mechanical properties 67

2.2.1. What is hardness? 67

2.2.2. Measuring the resistance to plastic flow 70

2.2.3. Measurements of toughness 72

2.2.4. Indentation size effects 76

2.3. Conclusions 81

3. Experimental Methods **83**

3.1. Powder mixing 83

3.2. Pellet pressing 86

3.3. Sintering and Densification 87

3.3.1. Pyrolysis of powders 87

3.3.2. Hot pressing (HP) 88

3.3.3. Spark plasma sintering (SPS) 90

3.3.4. Density measurements 91

3.3.5. Compositions and sintering schedules 93

3.4. Characterisation techniques 94

3.4.1. Scanning Electron Microscopy (SEM)[114] . . . 94

3.4.2. Energy Dispersive X-ray Spectroscopy 97

3.4.3. Focused Ion Beam (FIB) and Secondary Ion Mass Spectroscopy(SIMS) [115, 116] 100

3.4.4. Transmission Electron Microscopy (TEM) [117] 102

3.4.5. TEM sample preparation method 103

3.4.6. Homogeneity of AlN doped SiC 105

3.4.7. Polytype determination from XRD [119] 109

3.4.8. Etching and grain size measurement 112

3.5. Macro and micro indentation 114

3.6. Nano-indentation 115

3.6.1. Extraction of hardness and Young's modulus results from nano-indentation experiments 116

3.6.2. Area and load calibrations 118

3.6.3. Sources of error in nanoindentation experiments 121

3.6.4. Elevated temperature nano-indentation experiments 122

4. Sintering and Microstructure 123

4.1. Introduction 123

4.2. Homogeneity of AlN in AlN-SiC powder mixture and sintered samples 125

4.3. Effects of composition on sintering and microstructure of SiC 133

4.3.1. Effects of additive systems on densification and microstructure of SiC 134

4.3.2. Effect of level of AlN additions 142

4.4. Effects of time on sintering 147

4.5. Conclusions 151

5. Small scale indentation 155

5.1. Effects of microstructure on hardness and stiffness . . . 157

5.2. Measurement of plasticity parameters 161

5.2.1. Development of model to measure plasticity parameters of SiC 162

5.2.2. Obtaining the data for the model using nano-indentation 167

5.2.3. Incorporation of data into the model to measure the plasticity parameters 177

5.3. Conclusions 181

6. Large scale indentation **184**

6.1. Effects of microstructure on hardness 185

6.2. Effect of microstructure on cracking in SiC 188

6.3. Effect of indentation cracking on hardness of SiC . . . 197

6.4. Comminuta ejection 205

6.4.1. Effects of indentation load on comminuta ejection 206

6.4.2. Effects of amount of AlN in α-SiC samples on critical load for comminuta ejection 208

6.4.3. Mechanisms of comminuta ejection 209

6.5. Conclusions 211

7. Conclusions and further work **217**

7.1. Conclusions 217

7.2. Further work 219

A. Polytypes **246**

B. Densities Table **247**

C. Hardness **248**

List of Figures

2.1. Schematic of four common polytypes of SiC. The change in the length of c-axis in the unit cell can be observed. AlN has the crystal structure of 2H. 41

2.2. The microstructures of samples sintered by Ermer et al. [16] 43

2.3. A schematic showing the locations of SiC, silica and C. Carbon lies outside so reaction between silica and carbon does not affect the contacts that are forming between SiC particles unlike SiC-silica reaction. 45

2.4. Microstructures of SiC sintered samples containing (a) 3 wt% C and (b) 0.5 wt% C as sintering additives by Clegg [14] 46

2.5. 1 wt% excess carbon. Carbon inclusions are defects in the material (shown by arrow). Image taken from Ziccardi and Haber [19] 47

2.6. Literature data from various researchers [24, 26–28] suggesting a trade off between hardness and toughness of SiC. 50
2.7. Liquid phase sintered alpha-SiC. Image taken from Rixecker et al. [41]. Presence of Liquid phase on the grain boundaries can be seen as a bright phase. Additionally, inside the grains a brighter rim surrounds darker cores. Core and Rim has been pointed out by the arrows. . . 55
2.8. Tentative SiC-AlN phase diagram given by Zangvil and Ruh [7]. 57
2.9. Nano-indentation hardness data for the grain bundaries and the bulk of grains from Blog et al. [49]. x-axis refers to various sintering additives and techniques used. (see [49] for details) 58
2.10. Microstructure of sintered SiC samples containing 2.5wt% AlN and 0.5wt% boron carbide with and without carbon. Carbon additions lead to finer grains. Presence of a grain boundary phase is visible. Images from Pabit et al. [26]. 60
2.11. The effect of temperature on microstructure. Increase in temperature leads to grain growth. Images from Pabit et al.[26]. Again a grain boundary phase is present . . 60

2.12. TEM micrographs obtained on the samples sintered by SPS. (a) Pure SiC(6H polytype diffraction pattern in the bottom right hand corner), (b) SiC+C+B. Images from Maitre et al. [15] 64
2.13. A schematic of various cracks that are formed in and around the indent during and after the indentation. Images taken from Cook and Pharr [85] 74

3.1. SEM images of α-SiC from suppliers and AlN powders taken using SEM 5610 at Imperial college London . . . 84
3.2. Rotary evaporator. (1) Rotating flask, (2) Water tub, (3) Condensor. (4) Cooling water and circulation pump), (5) Liquid collecting flask, (6) Vacuum pump tube, (7) Power supply for water circulation pump 85
3.3. TGA traces of α-SiC, α-SiC + resin and α-SiC + resin + AlN. 88
3.4. A schematic of sintering tool used in the Hot Press. . . 90
3.5. Schematic showing the heating rates and temperatures used in various sintering schedules to densify SiC. . . . 95
3.6. Schematic diagram showing various signals that can be used for imaging and chemical composition of samples in SEM. SE: Secondary Electrons, BSE: BackScattered Electrons, PE: Primary Electrons, AE is Auger Electrons 98
3.7. Images showing various stages of FIB sectioning to make TEM samples 106

3.8. A schematic showing how the reduction in the area affects the standard deviation. 107
3.9. A schematic explaining Bragg's Law. 110
3.10. Schematic of nanoindenter showing various components. 115
3.11. A schematic of indenter tip showing h_c, h_t and h_e. . . . 116
3.12. A schematic of the load vs displacement curve. 117

4.1. Graph showing level of homogeneity achieved in samples. SPS-sintered sample was SPS for 5 minutes at 2100 °C. Interrupted sample was heated in HP to 1700 °C. The green pellet was uniaxially pressed pellet. All samples had the composition of SiC + 3 wt% C + 3.75 wt% AlN. The black lines are theoretical predictions for the standard deviations as a function of particle size. . . . 126
4.2. Graph showing level of homogeneity achieved during various stages of sintering from cold pressed pellet to a fully sintered sample. This graph is simply a section taken from the graph given in figure 4.1 at the area of 16 μm^2. All samples contained 3.75 wt% AlN and 3 wt% C. The starred sample was SPSed at 2100 °C whereas all other samples were hot pressed. 127
4.3. Electron image taken in FIB from a partially sintered sample at 1850 °C. The densification has clearly progressed significantly. 128

4.4. FIB image and SIMS map from the same area of α-SiC with 3 wt% C and 3.75 wt% AlN SPSed at 2100 °C. (a) Electron image (b) SIMS map of aluminium. White dots are where the Al signal was detected in the SIMS map. 129
4.5. SIMS maps of SiC samples with various amounts of AlN and 3 wt% C. (a), (b) and (c) are SPS sintered for 5 minutes at 2100 °C containing 0.75, 2.5 and 3.75 wt.% AlN whereas (d) is sintered using HP−Dwells sintering schedule which contains 3.75 wt.% AlN. Al is more homogeneously distributed in (d). Black dots show the position of initial AlN particles. (Image taken from [123]) 130
4.6. TEM micrograph showing an Al profile across a grain boundary in an α-SiC sample containing 3 wt% C and 3.75 wt% AlN SPSed at 2100 °C for 5 minutes. 131
4.7. TEM image of an SiC sample containing 3 wt% C and 3.75 wt% AlN SPSed at 2100 °C for 5 minutes and corresponding EDX data from the locations marked in the image. All amounts are in wt%. 132
4.8. Pressure vs temperature graph showing the stable phases of AlN solid, Al and N_2 gasses. 1 mbar is a typical pressure applied during vacuum sintering and hence above 1700 °C AlN should decompose and evaporate. 133

4.9. The graph showing the changes in the vacuum during hot pressing with dwells. Losses in the vacuum at various temperatures are evidence of chemical reactions evolving or using gas at those temperatures. 135
4.10. Densificaiton curves of SiC samples containing only C, only AlN and C + AlN HPed with intermediate dwells. (see table 3.3 for details about sintering schedule) . . . 136
4.11. The SEM micrograph of α-SiC sample containing 3 wt% C and 3.75 wt% AlN sintered using HP-dwells schedule. 137
4.12. TEM image of α-SiC sample containing 3 wt% C and 3.75 wt% AlN sintered using HP-dwells schedule. . . . 137
4.13. HRTEM of a grain boundary in α-SiC sample containing 3 wt% C and 3.75 wt% AlN sample sintered using HP-dwells schedule. There is no evidence of presence of glassy phase. 138
4.14. TEM image of an SiC sample containing 3 wt% C and 3.75 wt% AlN SPSed at 2100 °C for 5 minutes. Selected area electron diffraction pattern and corresponding EDX data from the locations marked in the image. All amounts are in wt.%. 139
4.15. HRTEM image of SPS sintered sample containing carbon and 3.75 wt% AlN. The grain boundaries are clean and there is no evidence of liquid phase. 140
4.16. SEM micrograph of sample SiC sample containing only 3.75 wt% AlN sintered using HP-Dwells schedule. . . . 141

4.17. TEM image of SiC + 3.75 wt% AlN sample HPed with dwells. The grain boundary does not show the presence of the liquid phase. 142
4.18. TEM image of SiC + 3.75 wt% AlN sample HPed with dwells. The grain boundary does not show the presence of the liquid phase. 143
4.19. TEM micrograph of 3 wt% yttria doped SiC with 3.75 wt% AlN SPS sintered at 1900 ° C showing the presence of liquid phase. 144
4.20. The effects of amount of AlN on the relative densities of SPSed SiC samples. AlN does not have an effect on the relative density. 145
4.21. Micrographs of α-SiC samples with 3 wt% carbon and various amounts of AlN. All samples were sintered using SPS at 2100 °C for 5 minutes. Image (d) taken from [123] 146
4.22. Graph shows effects of the amount of AlN on grain size. The trend lines above and below the values are plotted at 95% predictability. 147
4.23. Change in 6H polytype content with the change in the amount of AlN in α-SiC + 3 wt% C SPS samples. . . . 148
4.24. Densification curves for samples sintered using various sintering schedules. All samples had the composition of α-SiC + 3 wt% C + 3.75 wt% AlN. 149

4.25. Micrographs of (a) First attempt (image taken from [123] and (b) Repeated experiment of the sample that nominally contained α-SiC, 3 wt% C and 3.75 wt% AlN. They were both sintered using the HP cycle with intermediate dwells. 150
4.26. 6H content as a function of the time spent at sintering temperature for three α-SiC samples all containing 3 wt% C and 3.75 wt% AlN. Increasing time at sintering temperature increases 6H to 4H polytype transformation. 152
4.27. Time spent at sintering temperature for three α-SiC samples all containing 3 wt% C and 3.75 wt% AlN. Increasing time at sintering temprature increases grain size. 153

5.1. hardness as a function of applied load for samples with different grain size and compositions. All samples were SPSed at 2100 °C for 5 minutes. 157
5.2. Effect of grain size on nano-hardness. The hardness of SPS as well as HP sintered SiC samples is given. The hardness at zero of x-axis is the hardness of 6H−SiC and 4H−SiC single crystals for comparison. 159

5.3. Increasing time spent at sintering temperature reduces the hardness. Both sample types had the same composition of α-SiC + 3 wt% C + 3.75 wt% AlN. HP60 spent 60 minutes at sintering temperature (2045 °C) whereas SPS only spent 5 minutes at sintering temperature (2100 °C). 161

5.4. Schematic showing relationship between strain γ, Burgers' vector b and the dimensions of the sample. 163

5.5. A schematic to show in physical terms the projected activation volume, V_a and dislocation movement. Activation energy Q is the energy required for the dislocation to move from one plane to the next. The arrow shows the direction of shear flow stress τ. 166

5.6. SEM image of a nano-indent made using 200 mN load in the sample containing 2.5 wt%AlN and 3 wt% C produced by SPS. No cracks can be seen at the corners of the indent. 168

5.7. Graph showing the effect of strain rate and temperature on hardness for both coarse (8.6 ± 3.3 μm) (SiC with + 3.75 wt% AlN and some carbon sintered using HP-D sintering schedule (see table 3.3) and fine grained (1.7 ± 0.3 μm) (SiC + 2.5 wt% AlN + 3 wt% C SPSed for 5 minutes at 2100 °C) SiC. Hardness values are for 200 mN load and calculated from unloading slope. . . . 170

5.8. A schematic of load vs displacement curves produced at two different strain rates. Strain rate effects disappear as the hardness is calculated from unloading. 171
5.9. Elastic modulus versus applied load. The sample tested was the fine grained (1.3 ± 0.3 μm) SiC sample with the composition of SiC + 3 wt% C and 3.75 wt% AlN SPSed for 5 minutes at 2100 °C. 172
5.10. Hardness against strain rate showing that hardness for instantaneous hardness values increases with increasing strain rate for a change in load based strain rate calculation. Fine grains are 1.7 μm and coarse grains are 8.6 μm. Lines on the plot are the predicted change in hardness with strain rate using the model developed. . 173
5.11. Hardness against strain rate showing that hardness increases with increasing strain rate. f is fine grained SiC, c is coarse grained SiC. 4H and 6H are single crystals of the 4H and 6H SiC polytypes respectively. 174
5.12. Various models [63, 79, 81, 82, 145–148] and equations used to convert hardness into Yield stress. 176
5.13. Plot of shear flow stress against the strain rate can be used to calculate the activation volume from the gradients of the curves. the sample tested is SiC + 3.75 wt% AlN and some carbon sintered using HP-Dwells sintering schedule (see table 3.3 for details) with the grain size of 8.6 μm. 179

5.14. Plot of shear flow stress against temperature. The shear flow stress at 0 K is the Peierls stress whereas the activation volume can be calculated from the slopes of the curves. 180

5.15. Plot of shear flow stress against temperature. The drop in shear flow stress with increasing temperature is predicted by model and data correlates well with the literature [127, 149]. 181

5.16. Plot of hardness against temperature. The drop in hardness with increasing temperature predicted by the model correlates well with the literature [127, 149] for SiC single crystals 182

6.1. Graph showing a reduction in hardness measured using 5 Kg load with increasing porosity. All samples had the composition of α-SiC + 3 wt% C + 3.75 wt% AlN sintered using various HP and SPS schedules. The published data is taken from Slustker et al.[156]. 186

6.2. Graph showing how the hardness varies with load for different amounts of AlN. The samples were made by using SPS at 2100 °C for 5 minute.s and all contained α-SiC starting powder and 3 wt% C. 187

6.3. Graph showing a comparison between the sample with large grain size (with 0wt% carbon) and the sample with fine grains (with 3 wt% carbon). The large grained sample drops in hardness much more rapidly then the sample with fine grains. Both samples were sintered using HP-D sintering schedule. SPSed sample had 3 wt% yttria and 3.75 wt% AlN in SiC. 188
6.4. Cracking in and around the indent made using 5 kg load. (a) Sample with no carbon, (b) Sample with carbon. Both samples were sintered using HP-D schedule and contained α-SiC and 3.75 wt% AlN 189
6.5. Graph showing a comparison between the sample that spent one hour on the sintering temperature (HP60) and a sample that only spent 5 minutes (SPS). HP-D sample spent half an hour however, it spent longer time at the temperature above 1800 °C then the HP60 sample.The hardness at small scale is higher for SPSed sample. . . 190
6.6. Graph showing indentation toughness of an α-SiC sample containing 3 wt%C and 2 wt% AlN SPSed for 5 minutes as calculated using Niihara [96], and Anstis et al.[77] approaches. 192
6.7. Graph shows that there is little difference between the c/a ratios of these samples differing in the amount of AlN from 0.75 wt% to 3.75 wt%. All samples were sintered using SPS for 5 minutes. 193

6.8. Graph of c/a ratio as a function of time spent above 1800 °C during sintering showing a reduction in c/a ratio which translates into increased toughness with increase in time spent above 1800 °C. All samples had the composition of α-SiC + 3 wt% C and 3.75 wt% AlN. . 194
6.9. Graph comparing c/a ratios of samples containing liquid phase or not. 195
6.10. Cracks in various samples starting from the corners of indents. All cracks go around the grains. 196
6.11. Measured hardness of various samples plotted against load. For sintering schedule, please see table 3.3. All samples contained SiC. All samples except 0C-3.75-HPD contained 3 wt%C whereas C was replaced by yttria in 3Y-3.75-SPS sample. 198
6.12. Schematic showing effect of cracking on the size of indent(a) No cracking on the indent corners (b) Cracking on the corners of indents. 199
6.13. Graph of Log of crack length and diagonal length of indent against the log of applied load for three different loads to measure the critical load F_{crit}. 203
6.14. Diagram showing the hardness data from SiC samples. The curve represents the model propsed in this study. The dotted line is the power law fit which is given for comparison. 204

6.15. (a), (b) and (c) shows SEI of inside indents that have ejected the comminuta after unloading whereas (d) is a close up of inside of indent shown in (c) The sample was SiC + 3 wt% C + 3.75 wt% AlN sintered using HP-D schedule (see table 3.3) 206
6.16. SEI of the indented surface of a sample with composition of SiC + 3 wt%C + 2 wt% AlN SPSed. 207
6.17. Plot of indentation load vs % of indents with comminuta ejection behaviour for α-SiC with 2 wt% AlN and 3 wt%C SPSed sample. The critical load F_{crit} is defined as load at which 50% of total indents eject comminuta. 208
6.18. Graph showing effects of amount of AlN on the sample's critical load of ejection in the samples SPSed at 2100 °C for 5 minutes. Increasing amount of AlN increases critical load of ejection. 209
6.19. (a) The indenter moving into the sample with tensile stresses on the grain boundaries near the plastic zone and on the surface (b) Indenter travels further with compressive stresses inside the plastic zone. (a) whereas (c) Cracking and the residual stress build-up inside the indent pushing the material outwards. 213
6.20. Image showing the indent made in α-SiC with 3 wt%C and 2 wt%AlN SPSed sample using 49 N load. Surface cracking can be seen. 214

6.21. Image showing the indent made in α-SiC with 3 wt% C and 2 wt% AlN SPSed sample using 294 N load. Although it has chipped but the centre of the indent is firm with no ejection. 214
6.22. (a)Low magnification TEM image under the indent made using Berkovich indenter and 200 mN load in an SPSed sample with composition of SiC + 3 wt% C + 0.75 wt% AlN, (b) shows a close up of the crack in (a) whereas (c) shows the grain sliding 215
6.23. SEM image of an indent made in alumina showing evidence of communita ejection. Image taken from Ezra Feilden-Irving [157] 216

List of Tables

3.1. Properties of the raw powders as provided by suppliers. 85

3.2. The compositions sintered during this project 95

3.3. Table showing the in Hot Pressing schedules used with the method code that will be used to identify the sintering method used in each sample in the thesis. 96

3.4. Table showing equations to calculate various polytypes present in the SiC samples. The equations were developed by Ruska et al. [120] 111

5.1. $\star$ parameters are calculated from the equation. Attempt frequency, v was taken from Frost and Ashby [150], Burgers vector was calculated from assumption of partial dislocations [127, 151, 152]. 183

A.1. Table showing results of Polytypes calculations. All SPSed samples were sintered at 2100 °C and Hot Pressed at 2050 °C unless stated otherwise. 246

B.1. Densities of sintered samples measured using Archemedes method. The values are relative to the theoretical densities of the compositions. 247

C.1. Table showing Hardness of all the samples. The hardness was measured using 1 Kg load on Vickers indenter converted into projected area (Berkovich). 248

Nomenclature

Symbol	Description
Roman characters (capital)	
A	Area of the sample under the indenter tip
A_0	Area of indent with no cracking
A_c	Contact area between indenter and the sample
A_l	Overlapping area between two capacitor plates
A_p	Area under the XRD peak
A_s	Area sampled in homogeneity experiments
AlN	Aluminium Nitride
ΔA	Change in area due to cracking
BF	Bright field
BSI	Backscattered electron image
C	Carbon
C_p	Capacitance
D	Distance between two atomic layers
E	Young's modulus
E_i	Young's modulus of the indenter tip
E_r	Reduced modulus
E_s	Young's modulus of the sample

Symbol	Description
EDX	Energy dispersive X-ray spectroscopy
EELS	Electron energy loss spectroscopy
F	Load applied by the indenter
F_c	Critical load above which cracking starts
	influence the hardness
FIB	Focused ion beam
H	Hardness
H_0	Hardness in the absence of cracking
H_e	Hardness corrected for elastic recovery
HRTEM	High resolution transmission electron microscopy
I_s^m	Secondary ion current of species m
I^p	Primary particle flux
K_{1C}	Fracture toughness
L	Length of the sample
L(x)	XRD Peak intensity at position x
LPS	Liquid phase sintering
M	Mass of the sample
M_w	Mass of the sample when it is fully immersed in water
N	number of dislocations
P_i	Probability of i
PET	Polyethyleneteraphalate

Symbol	Description
Q	Activation energy
S	Initial slope of the indenter unloading curve
SEI	Secondary electron image
SEM	Scanning electron microscopy
SiC	Silicon carbide
SIMS	Secondary ions mass spectroscopy
SSS	Solid state sintering
T	Temperature
TEM	Transmission electron microscopy
V	Volume of the sample
V_a	Activation volume
XRD	X-ray diffraction
Y	Yield stress
Z	Atomic number
Roman characters (small)	
a	Half the length of diagonal of indent
a_0	Material constant related to residual surface stress
a_1	Material constant related to elastic deformation
a_2	Material constant related to plastic deformation
a	Half the length of diagonal of indent
a_0	Material constant related to residual surface stress

Symbol	Description
a_1	Material constant related to elastic deformation
a_2	Material constant related to plastic deformation
b	Burgers' vector
c	Crack length measured from the cnetre of the indent
d	Interpalnar spacing
d_i	Length of diagonal of indent
d_{ie}	Correction for elastic recovery in the length of indent diagonal
h_c	Height over which material and indenter are in contact.
h_e	Elastic deflection of the indented surface
h_t	Total displacement of indenter tip
k	Boltzman constant
l	length of a green pellet
n	Reflection order
q_A	Fraction of 'A' type particles
t	time
ℓ	Distance travelled by dislocation
x	Position where the XRD peak intensity L(x) is to be calculated
x_0	XRD Peak position
z	Number of particles considered in an experiment

Symbol	Description
Greek characters	
α	SiC of non-cubic crystal structure
$\alpha^{\pm}$	Ionisation probability for positive or negative ions
β	SiC of cubic crystal structure
Γ	Width of XRD peak at half its height
γ	Shear strain
$\dot{\gamma}_e$	Elastic strain rate
$\dot{\gamma}_p$	Plastic strain rate
$\dot{\gamma}_t$	Total strain rate
ϵ	constant
ε_0	Permittivity of vacuum
ε_r	Relative static permittivity
η	Transmission of the analysis system
θ_m	fractional concentration of m in the surface layer
λ	Wavelength
μ	micro
ν	Poisson ratio
ν_i	Poission ratio of indenter
ν_s	Poission ratio of sample
ξ	Equation fitting parameter
ρ	Density
ρ_w	Density of the water
ϱ	Shape factor including particle size and packing

Symbol	Description
σ	Standard Deviation
τ	Shear flow stress
τ_p	Peierls' stress
Υ	Constant that depends on the shape of indenter tip and applied load F.
φ	Equation fitting parameter
χ	constant of proportionality
ψ	constant of proportionality
ω	Dislocation velocity
y_m	Sputter yield
Derivatives	
$\frac{d\gamma}{dt}$, $\dot{\gamma}$	Strain rate
$\frac{d\ell}{dt}$	derivative of ℓ with respect to time
$\frac{dF}{dt}$	Loading rate

1. Introduction

Silicon carbide (SiC) is a ceramic with many commercial applications e.g. as the main structural material in telescopes for space exploration, as an abrasive for cutting and grinding, in wear parts such as bearings and atomisation nozzles, for the production of seals and valves in demanding chemical environments in the process industry, in high temperature heat exchangers and in ceramic armour plates for ballistic protection.

Due to the covalent nature of the atomic bonding in SiC, diffusion is slow and hence sintering of SiC is difficult. In fact, without the use of sintering additives, even hot pressing SiC does not lead to high densities. However, as will be discussed in the literature review 2, addition of sintering additives allows high density to be achieved. Typical systems include boron and carbon to promote solid state sintering or the addition of mixed oxides to promote liquid phase sintering. For the latter, aluminium oxide (Al_2O_3) is sometimes replaced by aluminium nitride (AlN) to reduce the weight loss during sintering, but AlN appears to have been used also in systems where solid state sintering would be expected. It is not entirely clear whether in such systems AlN addi-

tions lead to liquid formation by reaction with the silica present on the surface of the SiC, or whether AlN is also effective in promoting solid state sintering. The first part of this research was therefore devoted to microstructure development and sintering during hot pressing of AlN doped SiC.

For many of the industrial applications, the high hardness of SiC is a key property. For example, in ceramic armour it is commonly believed that "Harder is better"[1], and a high hardness is often considered desirable to enhance the wear resistance [2] although fracture behaviour can play a key role in wear resistance too [3]. Based on the literature, summarised in a second part of the literature review (2.2), the consensus appears to be that a high hardness and a high toughness are somewhat contradictory as a high hardness is believed to require small, equiaxed, grains whereas a high toughness requires a microstructure containing at least a good fraction of elongated grains. Therefore a second part of the research was devoted to clarifying the effect of microstructure on hardness.

However, hardness values depend on the measurement method and even when the method is the same, the scale of the measurement can also influence the hardness value found. Hence, the role of the microstructure was investigated both in the case of small indentations obtained by applying loads up to 400 mN as well as in the case of larger indents up to 294 N.

During the high load indentation experiments, a new observation was made: the centre of the indent can sometimes eject after unloading. A

final part of this investigation therefore documents these observations and again tries to link it to differences in the microstructure. Hence, the structure of this dissertation is that Chapter 2 contains a literature review on sintering additives for SiC and on hardness of SiC, followed by the experimental methodologies in Chapter 3. Chapter 4 discusses the results of the sintering with specific attention to the nature of the sintering mechanism. Chapter 5 presents the results of the low load indentation together with an interpretation of what controls the small scale hardness and Chapter 6 presents the results of the higher load indentation experiments together with a proposed model to describe the change in hardness with load. Chapter 7 describes the new observations of ejection from the centre of the indent and proposes a mechanism for this process. Finally Chapter 8 summarises the achievements and contains suggestions for further work.

2. Literature Review

This literature review has been divided into two parts. The first section is a review of the effects of sintering on the microstructure of SiC, whereas the second section, the use of indentation to characterise materials is discussed as well as theories which have been proposed to explain the observation that the measured hardness decreases with indent size.

2.1. Effects of processing on the microstructure of SiC

Silicon carbide (SiC) is a covalently bonded material with a theoretical density of 3.21 Mg m^{-3}. SiC is found in a range of polytypes. Cubic SiC is known as β-SiC whereas all other crystal structures, including several forms of hexagonal and rhombohedral, are grouped together and are known as α-SiC. The hexagonal crystal structure also exists in several types. There are various [4, 5] ways to describe the polytypes. Ramsdell notation [5] uses a number followed by a letter. The letter gives information about the crystal structure (i.e. C is for cubic, H

is for hexagonal, R is for rhombohedral) and the number represents the number of layers along the c axis per periodic cycle. Different polytypes have slightly different physical, mechanical and electrical properties [6]. Although a large number of polytypes exist, the most frequently occuring are 2H, 4H, 6H, 15R and 3C. The different polytype structures are schematically shown in figure 2.1.

These polytypes transform from one to another depending on the sintering additives, temperature and time at higher temperatures [7]. There are two types of mechanisms by which these transformations take place. The first are slow solid state mechanisms i.e. via diffusion or dislocations which are generally found in single crystals whereas the fast transformation mechanisms occurs through vapour, surface or liquid phase diffusion and are more common in polycrystalline compacts and powders. Fast transformation is usually accompanied by other phenomena such as grain growth. It is difficult to distinguish between the different types of transformation mechanisms experimentally[4].

2.1.1. Boron, carbon and aluminium as sintering additives

Different additives are used to enhance the diffusion to make it easier to sinter SiC. The most common sintering additives used to densify SiC are carbon and boron and/or aluminium. Prochazka and Charles [8, 9] first introduced boron and carbon in the early 70s. Several hypotheses explain how boron and carbon help the sintering of SiC. One

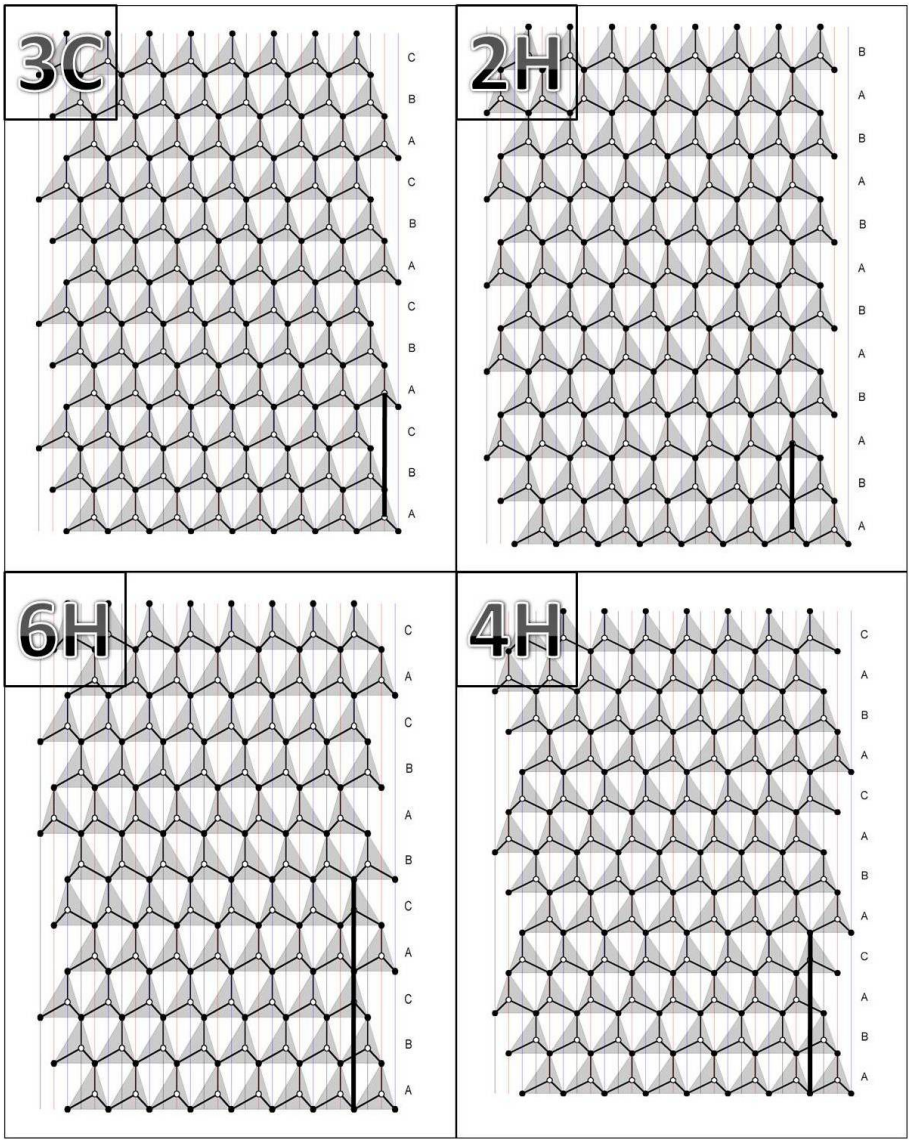


Figure 2.1.: Schematic of four common polytypes of SiC. The change in the length of c-axis in the unit cell can be observed. AlN has the crystal structure of 2H.

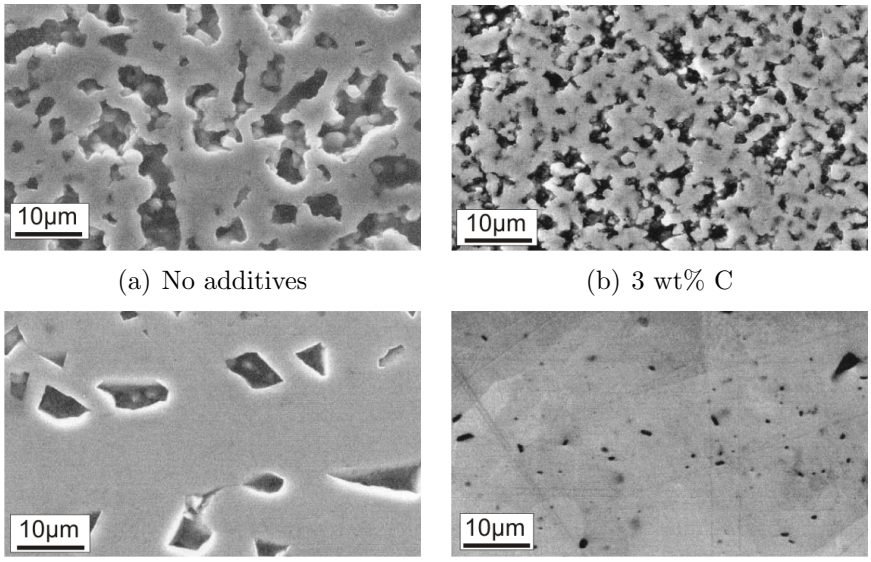
hypothesis is that boron and carbon introduce defects into the SiC structure which results in enhanced lattice diffusion. The hypothesis formulated by Prochazka and Charles [8] mentions that boron lowers the grain boundary energy and hence modifies its properties. Gu et

al. [10] detected boron on the grain boundaries and concluded that boron plays a double role at the grain boundary for promoting densification. It improves grain boundary diffusivity as well as maintaining a covalent grain boundary by replacing Si and bonding with C from the SiC compound. This supports Prochazkas hypothesis. However, the reduction in the grain boundary energy is yet to be verified. Carbon increases the self diffusion of SiC by a factor of 100 [11]. Similar numbers have been found for boron [12].

The role of boron in sintering of SiC was discussed by Stobierski and Gubernat [13]. They used various amounts of boron (0 to 4 wt%) with 3 wt% carbon to sinter SiC and showed that depending on the amount of boron added, its role changes. The densification increased with increasing amount of boron until it reached the solubility limit of boron in SiC. Increasing the boron amount even further lead to discontinuous grain growth and curved grains were considered an evidence of presence of liquid phase. They found that the optimum amount of boron at which the process remains solid state and does not lead to discontinuous grain growth is in the range of 0.2 to 0.5 wt.%. These findings were supported by the work of Clegg [14] and Maitre et al. [15].

Addition of boron alone, as found by Ermer and Wieslaw [16] , leads to excessive grain growth. The grains elongated to approximately 30 μm. The density increased to 95% with closed porosity. Some carbon granules were detected within the grains and SiC decomposition was also detected by 3% weight loss.

Carbon addition without boron did not change the densification significantly. The densities achieved were about 80% of theoretical compared to 70% for undoped samples. However, the porosity was well dispersed which lead to a higher Weibull modulus. Decomposition of SiC was less than that of boron-doped samples with a weight loss of about 1%. Moreover, finer grains with an average size of less than 5 μm were present. Analysis with the EDX showed that grains were still covered in carbon. When boron and carbon were replaced by boron carbide, a liquid phase formed due to the reaction between the boron carbide and the surface silica on the SiC particles. Examples of the microsctuctures obtained are shown in figure 2.2.



(a) No additives (b) 3 wt% C

(c) 0.5 wt% B (d) 0.5 wt% B, 3 wt% C

Figure 2.2.: The microstructures of samples sintered by Ermer et al. [16]

When both carbon and boron were added as sintering additives, the densities achieved were 99% of the theoretical. The grain size was

relatively smaller with the length of grains in the elongated axis to be around 30 μm as compared to 100's of μm in the sample with no carbon. Ermer and Wieslaw [16] concluded that both boron and carbon have their own roles in helping with the sintering. Boron modifies the grain boundary properties whereas carbon forms inclusions that limit the grain growth.

Another role of carbon in sintering was discussed by Clegg [14]. He proposed that carbon could be used to remove silica from the SiC surface to stop the SiC-silica reaction from taking place. Silica is present on the surface of the SiC particles because of the oxidation of SiC [17]. This oxidation varies with particle size and processing conditions. Small particle sizes leads to higher oxygen contents because of the higher surface area. Exposure to oxygen at high temperature also leads to enhanced oxidation. The silica-SiC reaction leads to release of gases from the SiC, which results in porosity and breaking of bonds that are being formed during sintering. Two possible reactions were proposed by Clegg [14].

$$SiO_2 + 2SiC = 3Si + 2CO \tag{2.1}$$

$$2SiO_2 + SiC = 3SiO + CO \tag{2.2}$$

Equation 2.1 has Si as its product, whereas equation 2.2 has SiO gas as its product . When carbon is added, it reacts with the silica and removes it. This reaction takes place at 1400 °C before the silica-SiC

reaction becomes thermodynamically favourable so there is no silica left to react with SiC. Volatile gases still come out of the specimen however instead of coming out from underneath the silica layer on the powder as is case with the silica-SiC reaction, gases come out from near the surface of the powder which does not lead to breaking of the initial contacts that are formed between the SiC particles. A schematic explaining the reactions between SiC, SiO_2 and C is given in Figure 2.3.

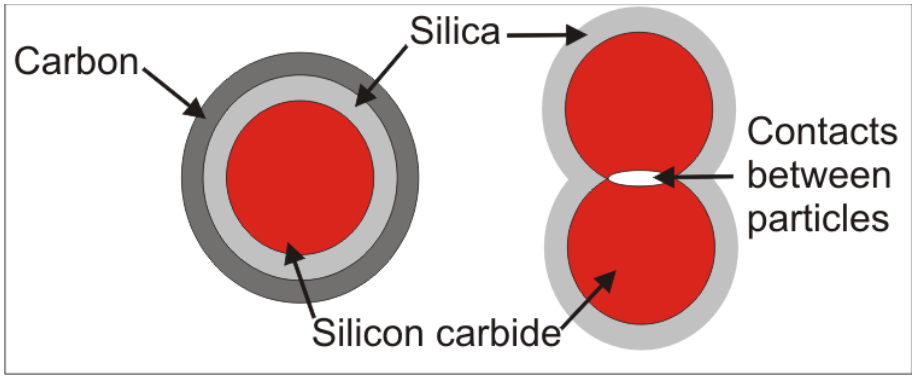
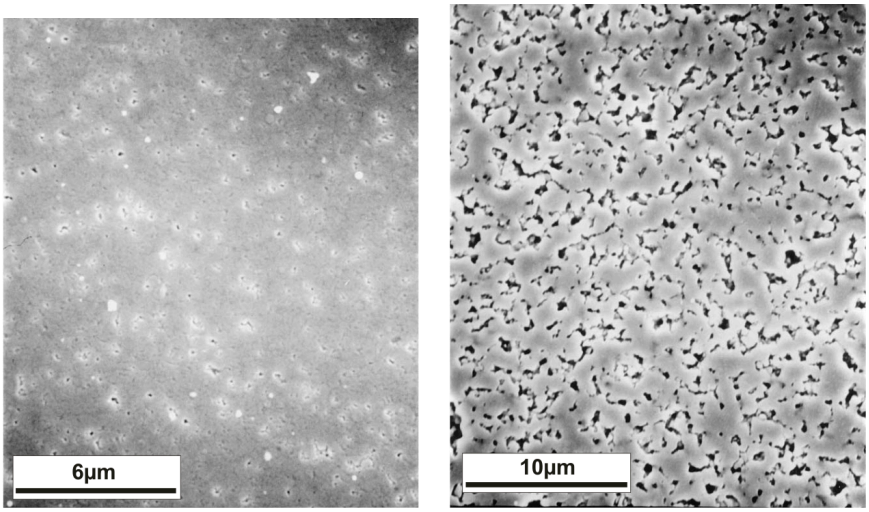


Figure 2.3.: A schematic showing the locations of SiC, silica and C. Carbon lies outside so reaction between silica and carbon does not affect the contacts that are forming between SiC particles unlike SiC-silica reaction.

As shown in figure 2.4 avoiding the SiC-silica reaction leasd to small well dispersed pores, whereas the SiC-silica reaction causes a disrupted microstructure to form, which does not heal much during sintering.

Raczka et al. [18] confirmed the results of Clegg [14] that carbon restricts the grain growth in SiC by showing that increasing the amount of carbon in the sample led to a finer grain size (less than 10 μm and a higher fracture toughness 5.18 $\pm$ 0.46 MPa$\sqrt{m}$. Hardness measured



(a) SiC with 3 wt% C (b) SiC with 0.5 wt% C

Figure 2.4.: Microstructures of SiC sintered samples containing (a) 3 wt% C and (b) 0.5 wt% C as sintering additives by Clegg [14]

using Knoop indenter and 10 N load for a sample with 3 wt% C was 23.8 $\pm$ 0.44 GPa. However, Ziccardi and Haber[19] has suggested that it is also important that there is no excess carbon present in the sample. This is because a common defect found in the materials that contain carbon is the presence of carbonaceous particulates as can for example be seen in figure 2.5. These are defects in the material and lead to detrimental mechanical performance. Any badly mixed carbon can lead to similar sorts of defects. Ziccardi and Haber [19] reported as much as a 20% reduction in hardness as a result of increasing excess carbon. However, the authors did not comment on the grain size in relation to the changes in the excess carbon amount. Increasing amounts of excess carbon also lead to higher scatter in the hardness data. This might be due to not being able to achieve homogeneity with higher

carbon contents.

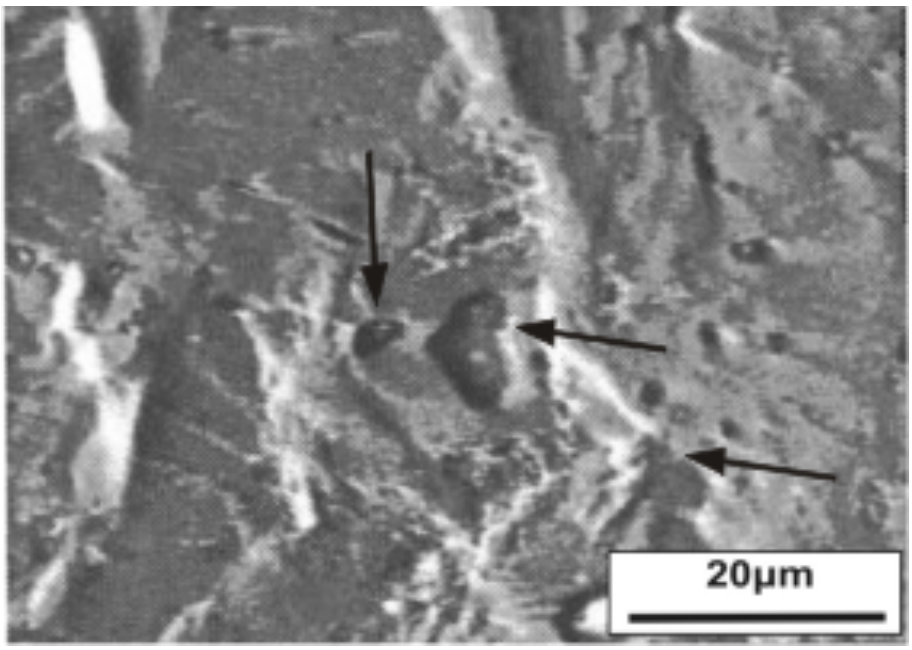


Figure 2.5.: 1 wt% excess carbon. Carbon inclusions are defects in the material (shown by arrow). Image taken from Ziccardi and Haber [19]

Ziccardi and Haber [19] argued that similar compositions of SiC sintered under identical conditions give different mechanical properties and microstructures because of the various forms of carbon applied by different manufacturers. These include, carbon black, resins, surfactants and even carbon nano-tubes. They behave quite differently during sintering and so produce different microstructures.

The sintering with boron and carbon is solid state sintering since no evidence for the presence of liquid is found in the final microstructure. The typical temperatures for this sintering are in the range of 2000 °C to 2200 °C.

Usually carbon and boron doped SiC has fine grained (1-4 μm) and equiaxed microstructure [9]. It has good high temperature creep and oxidation resistance [20]. However, it suffers from very low fracture toughness (3-4 MPa$\sqrt{m}$) [21] although carbon and boron are known to encourage the β to α-SiC transformation which can induce the formation of elongated grains.

To reduce the sintering temperature as well as to increase the fracture toughness, aluminium (Al) in combination with boron and carbon have been used to sinter SiC. Together this system of additives is known as ABC-SiC system. The idea was that Al will reduce the amount of sintering additives neded to sinter SiC hence improving its high temperature properties. The addition of Al lead to an improvement in the fracture toughness and a fracture toughness of 9 MPa$\sqrt{m}$ was reported by Cao et al. [22] for a β-SiC starting powder. The transformation from β to α-SiC lead to elongated grains resulting in higher toughness due to crack bridging.

The amount of Al added has an impact on the microstructure and the resulting mechanical properties. Zhang et al. [23] found that increasing Al from 3 wt% to 5 wt% resulted in an increase in the aspect ratio from 4.7 $\pm$ 1.6 to 23.2 $\pm$ 6.8. However, the proportion of elongted grains decreased until the amount of Al reached 7 wt% where elongated grains disappeared. The sample with elongated grains had fracture toughness valuse in excess of 5 MPa$\sqrt{m}$. The toughness decreased to 3.8 MPa$\sqrt{m}$ for the quiaxed sample measured using indentation fracture toughness with indents made using 10 kG load. Zhang et al.

[23] also found that the high toughness was linked to the presence of amorphous film present on the grain boundaries which they observed using High Resolution Transmission Electron Microscopy (HRTEM). Hardness measured using 4.9 N load were similar to the hardness of boron and carbon system [18]. However, the standard deviations of the hardness results were not mentioned by Zhang et al. [23]. Work of Pabit [24] showed that the addition of Al lead to a reduction in hardness from 25 GPa to 20 GPa when measured using Vickers indenter and 1 Kg load. Ray et al.[25] also found that there was a drop in hardness from 20 GPa to 13 GPa with a decrease in the amount of Al from 0.6 wt% to 4 wt%. He suggested that this is due to the formation of the intergranular film which allows the grains to slide. This film has been suggested to increase the toughness (from 2.7 ± 0.1 to 6.1 ± 0.3 MPa$\sqrt{m}$ [25]) of SiC [23].

As the amount of Al was increased above 4 wt%, the hardness increased again but the toughness dropped. Hence there is a trade off between high hardness and high toughness as can be seen from figure 2.6. Al seems to discourage the β to α-SiC transformation by forming a film on the grains; however it does encourage the transformation of 6H into the 4H polytype[4].

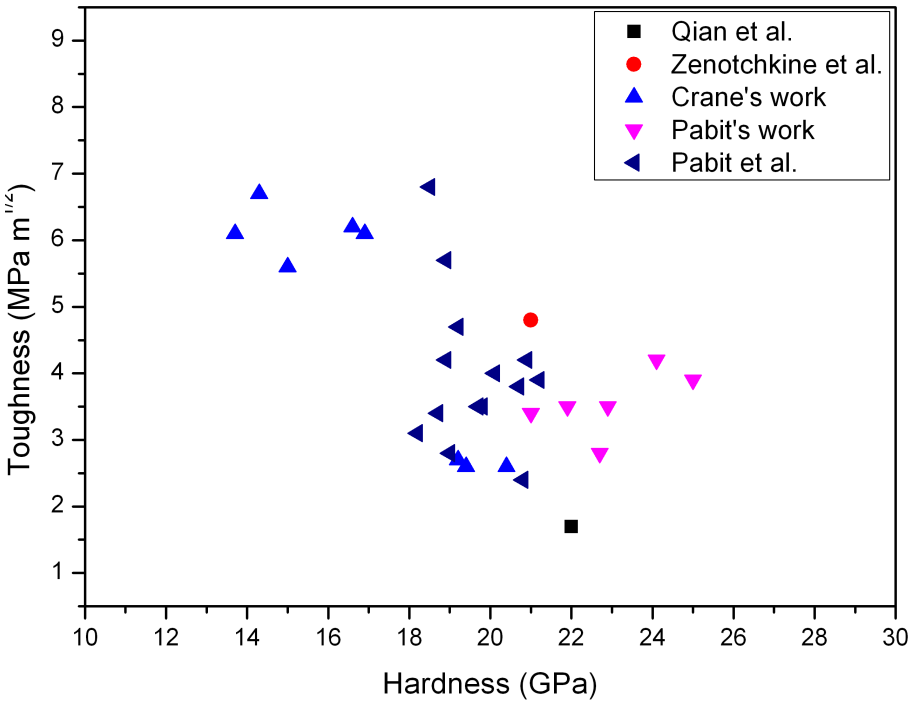


Figure 2.6.: Literature data from various researchers [24, 26–28] suggesting a trade off between hardness and toughness of SiC.

2.1.2. Alumina, yttria and silica as sintering additives

The motivations to use oxides (alumina Al_2O_3, yttria Y_2O_3, silica SiO_2) as sintering additives were to reduce the sintering temperature as well as to increase the toughness of SiC. The toughness was found to improve through the addition of a secondary phase. Kim and Kim [29] found that increasing the amount of secondary phase leads to increased crack deflection angle resulting in increase in fracture toughness.

Chen [30] found that addition of oxides into SiC as sintering aids makes SiC tougher. His argument was that in liquid phase sintering,

these oxides form a secondary phase on the grain boundaries and tripple junctions. There is a thermal expansion mismatch between both phases and as a result internal residual stresses are present. These lead to a weaker interface and hence the fracture mechanism is intergranular. Extensive crack deflection occurs during failure, which increases the toughness of SiC compared to the SiC doped with boron and carbon.

Omori and Takei [31] developed liquid phase sintered silicon carbide (LPS-SiC) in 1980s. According to Liu and Fu [32], Omori and Takei were the first to use alumina and yttria as sintering additives. Since then a number of oxide mixtures have been tried. The main advantage of Liquid Phase Sintered (LPS) SiC is considered to be greater control over microstructure and hence mechanical properties. The basis of this microstructure control is linked to the β to α-SiC transformation; however, this transformation is linked to the ratios of α to β-SiC in the starting powders. Additive system, temperatures and other sintering conditions also play a role in this transformation. This transformation is important for fracture toughnessbecause transformation from β to α normally leads to elongated grains.

Alumina reacts with the surface silica and forms a liquid. It also forms an oxycarbide melt at higher temperature due to the dissolution of SiC [33]. Chen [30] also found that sintering at high temperatures for longer times lead to decomposition of SiC. They concluded this by observing the presence of large pores present near the surface of the samples. The decomposition of SiC during sintering with Al_2O_3

was also observed by Ihle et al. [34]. They suggested that the reaction products include CO, SiO, Al_2O_3 and Al based on the weight loss. The possible reactions are given below.

$$Al_2O_3 + SiC = Al_2O_{(g)} + 3SiO_{(g)} + CO_{(g)} \tag{2.3}$$

$$3Al_2O_3 + 5SiC_{(solid)} = Al_2O_{(g)} + 3SiO_{(g)} + 5CO_{(g)} + 3Al_{(melt)} + Al_{(gas)} + 2Si_{(melt)} \tag{2.4}$$

Equation 2.3 was proposed by Lee and Kim [35] whereas equation 2.4 is given by Ihle et al. [34]. Similar reactions to Ihle et al. [34] were also observed by Gomez et al. [36] when Al_2O_3 was added in conjunction with carbon.

Ihle et al. [34] also showed that if the sintering is carried out in CO environment then the SiC-Al_2O_3 reaction can be suppressed. This shows that CO is indeed one of the reaction products.

If Y_2O_3 is used as a sintering additive then appreciable gas phase reaction with SiC is not detected. It also does not form enough liquid phase for complete densification. Ihle et al. [37] found that depending on temperature and atmosphere, silicon carbide and yttrium oxide react to form silicides and yttrium carbides. These can result in the decomposition of the samples after sintering. However, these reactions can be suppressed if an Ar/CO atmosphere is used.

Chen [30] also found that using Al_2O_3 on its own does not yield

good results because liquid phase does not form below 2060 °C which is the melting point of alumina. However, if it is used in conjunction with yttria in a ration consistent with the eutectic in the alumina-yttria system then liquid phase is observed at lower temperatures which helps with the densification. The formation of an yttrium-aluminium-garnet (YAG) phase was observed on the grain boundaries which is believed to improve the toughness of SiC. A toughness value of about 8 MPa$\sqrt{m}$ was reported by Lee and Kim [35]. However, the problem of weight loss remained. This weight loss can be reduced by reducing the time spent at higher temperatures but then β to α-SiC transformation will not have time to occur extensively and therefore the desired elongated grains will not form. Another solution is the use of a powder bed. The powder bed is present to preferentially decompose in place of the sample. While powder beds are effective in reducing weight loss, they make the processing complicated and are difficult to combine with pressure assisted densification methods.

Strecker et al. [38] showed that the use of yttria and silica as a sintering additive system is inadequate to densify SiC as silica reacts with SiC hence there is none left to influence densification at the sintering temperature. Clegg [14] found that this reaction is complete at 1900 °C and the reaction is detrimental to the densification.

2.1.3. Use of aluminium nitride (AlN) as a sintering additive

The use of AlN as a sintering additive has been either as a replacement for Al in the ABC-SiC system or as a replacement for Al_2O_3 in the liquid phase sintering of SiC. The reason for the use of AlN as a replacement for Al in the ABC system is to improve the hardness of the ceramic which Ruh and Zangvil [39] reported to be around 26 GPa (converted from Knoop hardness using 700 g of load) but it results in slightly lower toughness values 4.5 MPa$\sqrt{m}$. This was beneficial for the cutting tool and armour applications of SiC. Adding Al resulted in higher toughness (9 MPa$\sqrt{m}$) [22] but the hardness was affected [24]. Equiaxed grains on the other hand improved hardness.

The reason for the replacement of Al_2O_3 by AlN was to reuduce the weight loss during sintering and hence the need for a powder bed. Strecker et al. [38] observed that the weight loss with Al_2O_3/Y_2O_3 system was much more severe than the weight loss associated with the AlN/Y_2O_3 system. The first to try AlN as a sintering additive for SiC were Storm and Chia [40]. They found that a powder bed was not required with AlN. However, Rixecker et al. [41] showed that thermal decomposition also takes place but it can be successfully suppressed by a slightly higher partial pressure of nitrogen without the need for a powder bed. They showed that a fracture toughness of 8 MPa$\sqrt{m}$ can be achieved at high temperature by LPS-SiC because of anisotropic grain growth of α-SiC shown in figure 2.7. This toughness figure is in

agreement with the figure of 8 MPa$\sqrt{m}$ reported by Lee and Kim [35] who used Al_2O_3-Y_2O_3 additive system.

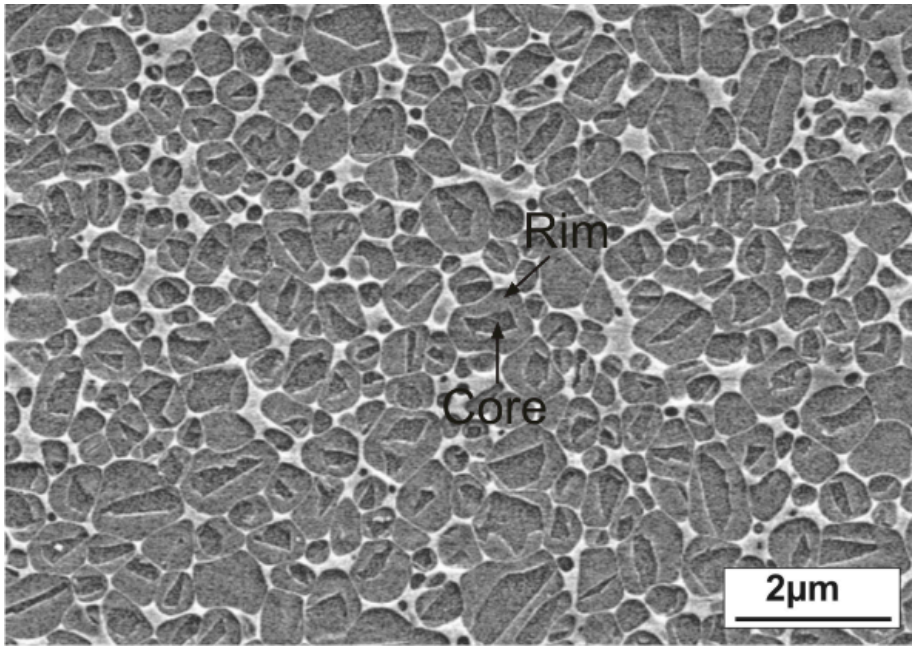


Figure 2.7.: Liquid phase sintered alpha-SiC. Image taken from Rixecker et al. [41]. Presence of Liquid phase on the grain boundaries can be seen as a bright phase. Additionally, inside the grains a brighter rim surrounds darker cores. Core and Rim has been pointed out by the arrows.

Another interesting feature of the microstructure in figure 2.7 is the presence of a 'core-rim' structure. Various explanations are given for the presence of this structure. The explanation given by Rixecker et al. [41] was that the rims are slightly richer in oxygen. This oxygen could be present due to the silica on the surface of the SiC or due to oxidation of the AlN and or due to the added yttria. Another explanation could be that the rim is evidence of the formation of AlN-SiC solid solution, which has been reported in literature frequently [7, 39, 42–47].

The formation of this solid solution between AlN and SiC has received a lot of attention as a controlling mechanism of the microstructure and properties of SiC. The phase diagram (see figure 2.8) also suggests that different polytypes are stable at different compositions and temperatures. Strecker et al. [38] did not see this transformation. and attributed this to the short time (30 minutes) spent at sintering temperature, i.e. there had not been enough time for the transformation to take place.

Attempts have been made to use AlN as a replacement for yttria in the alumina-yttria system of SiC sintering additives. The motivation was that alumina is known to form the elongated grains whereas AlN promotes finer equiaxed microstructure, so their combination could provide a composite microstructure. [48]

Pan et al. [42] found that AlN and SiC form a solid solution at around 1800 °C. High densities were achieved by pressureless sintering at 2100 °C for 1 hour in an Ar atmosphere. They argued that since the vaporisation rate of AlN far exceeds that of SiC, AlN particles would redistribute and deposit on the surface of SiC grains. This process continues until all the AlN particles disappear and allows a layer of AlN-SiC solid solution to form on the edge of the SiC grains. They also argue that this restricts the grain growth of SiC grains in the directions which were coated with AlN-SiC solid solution. So the final grain shape was elongated. Pan et al. [42] argued that AlN will completely diffuse into SiC grains provided enough time at temperature is allowed. Otherwise, the solid solution only forms near the grain boundaries. They

identified the SiC grains to be of the 4H type, a bending strength of 420 MPa and fracture toughness to be 4.40 MPa$\sqrt{m}$. According to the tentative phase diagram by Zangvil and Ruh[7] given in figure 2.8 the formation of this solid solution results in the polytype transformation of SiC from 6H to 4H. Increasing the amount of AlN leads to more and more transformation until eventually there is complete transformation from 6H to 2H which is the normal hexagonal stacking sequence and also the crystal structure of pure AlN.

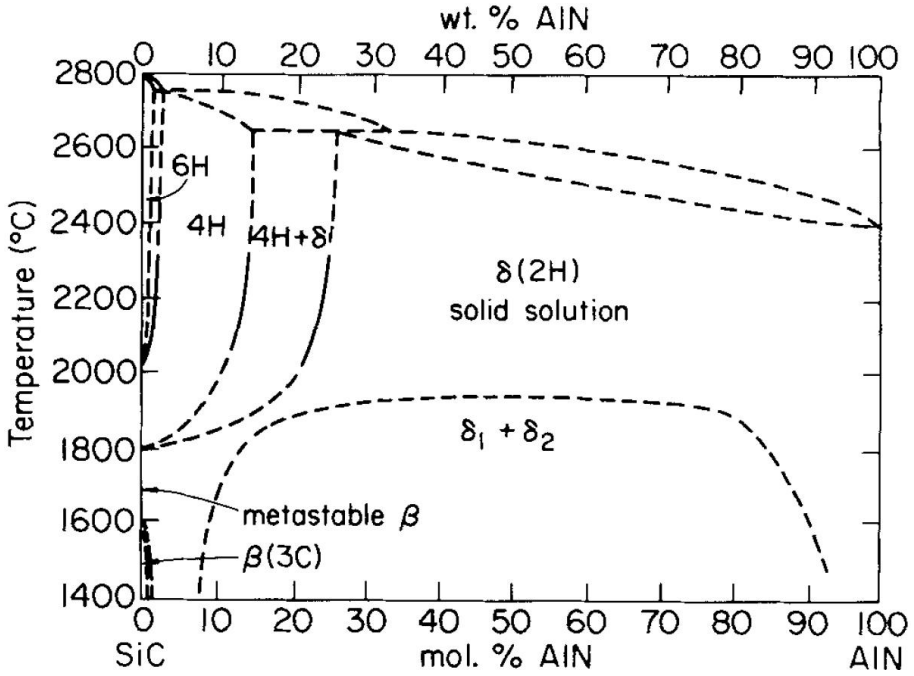


Figure 2.8.: Tentative SiC-AlN phase diagram given by Zangvil and Ruh [7].

It has been reported that the rims have slightly lower hardness compared to the cores of SiC[49, 50] suggesting that perhaps cores are pure SiC whereas rims are enriched with impurities leading to a reduction in hardness. Balog et al. [49] found that there was a difference

of around 2 GPa between the nano-hardness of cores and rims of SiC. However, the indent size was small (3.5 mN load) making it more prone to measurement error espacially when such small indents are made on a rough etched surface near grain boundaties, which were not defined in the paper. Their data suggested that, in fact, the hardness of cores and rims was similar. There were only a few indents available for the examination and some of them were found to be near the grain boundaries.

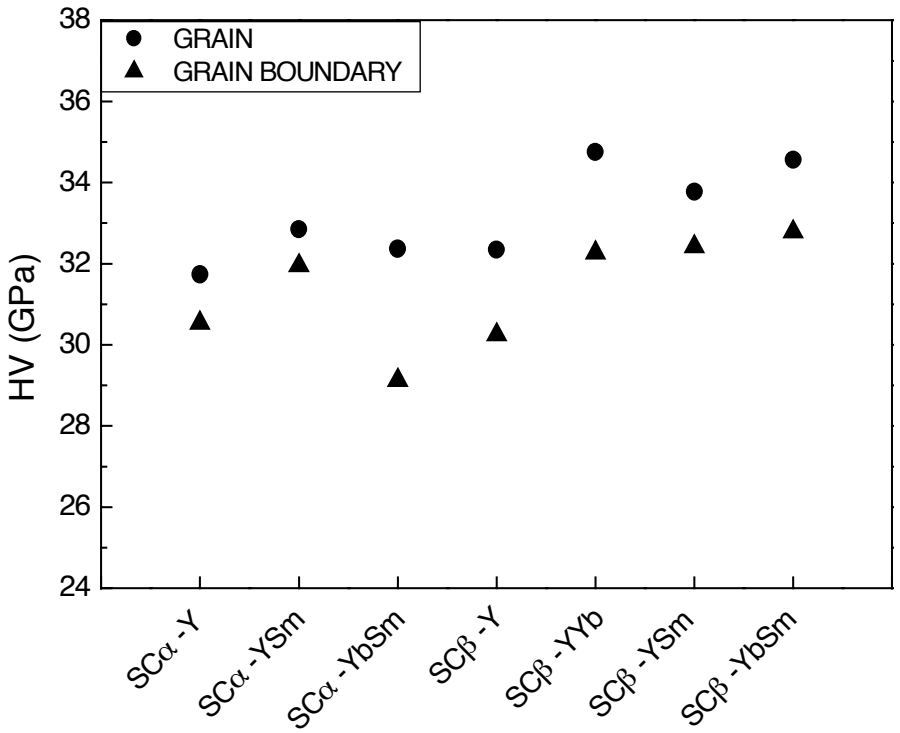


Figure 2.9.: Nano-indentation hardness data for the grain bundaries and the bulk of grains from Blog et al. [49]. x-axis refers to various sintering additives and techniques used. (see [49] for details)

Balog et al. [49] also reported that there was no effect of grain bound-

ary phases on the nano-hardness of SiC. It was also found that the hardness of rims depended on the concentration of AlN in the rims by Ruh and Zangvil[39] who measured the hardness through micro-indentation using a Knoop indenter at 700 g load where perhaps cracking was influencing the indent size. However, secondary phase results in reduction in hardness of SiC due to the micro-cracking due to residual stresses arising from the differences in the thermal expansion coefficients between various phases[51]. This is why Huang et al. [52] proposed that the minimum amount of additives should be used but the importance of high homogeneity was stressed.

Pabit et al. [26] hot pressed 14 compositions of SiC, AlN, C, B and B_4C at between 1900 °C and 2200 °C. Carbon was added in the form of phenolic resin, while all other materials were in powder form. Samples that did not contain carbon and boron carbide reached 99.5% of theoretical density. Aluminium resulted in large grains compared to addition of AlN, which restricted the grain growth and closed the pores at lower temperature. Increasing the sintering temperature lead to grain growth in the samples that did not contain any sintering additives apart for 1.65 wt% pure Al as shown in Figures 2.10 and 2.11.

Polytype studies on the samples containing Al suggested that increasing the sintering temperature lead to the transformation of SiC from 6H to 4H which was in agreement with the work of Page [4]. The 6H to 4H transformation increased by increasing the amount of Al whereas increasing the amount of AlN actually lead to a reduction in the amount of transformation of polytypes from 6H to 4H. This is

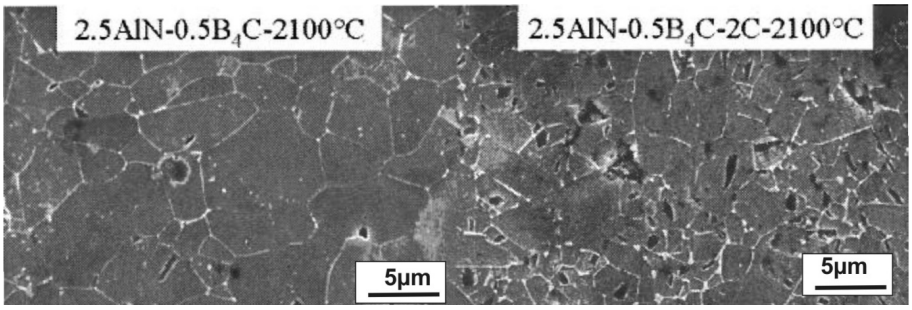


Figure 2.10.: Microstructure of sintered SiC samples containing 2.5wt% AlN and 0.5wt% boron carbide with and without carbon. Carbon additions lead to finer grains. Presence of a grain boundary phase is visible. Images from Pabit et al. [26].

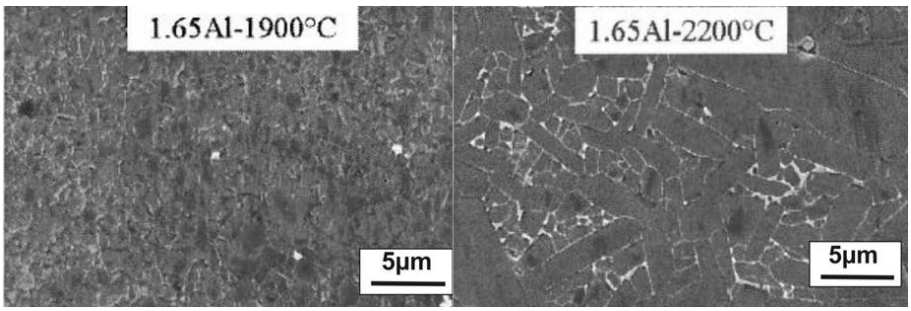


Figure 2.11.: The effect of temperature on microstructure. Increase in temperature leads to grain growth. Images from Pabit et al.[26]. Again a grain boundary phase is present

not consistent with the work of Zangvil and Ruh [7] according to which 6H polytype of SiC should transform to 4H at the compositions tested under equilibrium conditions. There was no polytype transformation for the sample that did not contain Al in any form.

Pabit [24] found that SiC with Al additives sintered at higher temperatures had elongated grains (see Figures 2.10 and 2.11) which were capable of bridging cracks and hence enhance the toughness. However, B_4C and C addition or Al added SiC sintered at lower temperatures

lead to equiaxed grains. SiC-AlN had predominantly intergranular fracture but its toughness was lower than the Al doped sample due to the absence of elongated grains. SiC with 2.5 wt% AlN and B_4C and C showed low toughness (3.5 ± 0.1 MPa$\sqrt{m}$ and it failed primarily through transgranular crack propagation. Fracture toughness was found to be correlated to the product of the aspect ratio times the square root of the grain size times the volume fraction of the bridging grains assuming that all the intergranular grains bridge the crack in line with the model developed by Zenotchkine et al. [27].

In conclusion, where AlN is used as a replacement for Al_2O_3 in mixed oxide sintering additive systems, it reduces the weight loass by not reacting with SiC so readily but is still capable of forming liquid phase by reacting with other oxides present in the system. When ALN replaces Al in sintering additives consisting of combination of Al, boron and/or carbron and B_4C, it is less clear how its presence influences sintering.

In these systems, the presence of AlN instead of Al appears to reduce the formation of elongated grains and therefore also enhances the hardness.

2.1.4. Effects of sintering schedule on sintering and microstructure of SiC

It is not just the additives that determine the microstructure in the final product. As mentioned earlier, Pan et al. [42] and Pabit et al. [26] have found that the time spent at sintering temperature can have

an effect on the microstructure as well as the sintering temperature itself. Also it has been suggested by Ray et al. [47] that the heating rate influences the densification curves in pressure assisted sintering.

Time spent at sintering temperature increases the grain size [26] whereas increasing the sintering temperature also leads to coarser grains [26, 53, 54]. Intermediate dwells are used to allow certain reactions to reach completion and to allow the gaseous products of these reactions to escape [14].

Ray et al. [47] found that increasing the heating rate during sintering of SiC by 15 °C min^{-1} results in an increase of 100 °C in the densification temperature. They also observed a change in microstructure as a result of the change in heating rate. Zhou et al. [55] also reported that faster heating rates (400 °C min^{-1}) favoured the 4H polytype. They carried out their experiment using Spark Plasma Sintering (SPS) method.

SPS is a non-conventional sintering technique. It is known by varous names including Field Assisted Sintering Technique (FAST) and Pulse Electric Current Sintering (PECS). while the formation of a plasma during the process is debatable, the term SPS will be used in this thesis as it is still the most widely recognised acronym to describe this method of sintering.

The principle of operation of SPS is that an electric field is applied across the sample and the current passes through the powdered particles. A very good review of SPS is given by Munir et al. [56]. The resistance in the contacts between particles generates heat (Joule heat-

ing) where heating rates of up to 600 °C min^{-1} can be applied. Sintering can be carried out at lower temperature due to the application of heat concentrated at the contacts between particles. If the powdered particles are non-conducting than the current passes through the die containing the powder and gets hot, which then acts as a heating element. This is similar to conventional hot pressing where the heat is applied to the die which than heats up the powder inside. Pressure can also be applied in SPS. This fast processing method is helpful if the formation of secondary phases is to be avoided during sintering [57].

Maitre et al [15] showed that SPS can be used to sinter SiC without using sintering additives. They reached relative densities of 97.5% by sintering SiC at 1950 °C for 5 minutes. The heating rates used were 100 °C min^{-1} and the load of 100 MPa. Reducing the load to 40 MPa, the heating rate to 40 °C min^{-1} and the sintering temperature to 1850 °C resulted in a reduction in the density of pure SiC to 92%. They argued that these results are due to the characteristics of the SPS heat treatment such as self heat generation because of microscopic electric discharge between the particles which results in high speed mass and heat transfer. This results in transport only occurring at the particle surfaces and contacts. Also the rapid densification could be correlated to the mechanisms with faster kinetics such as diffusion or time dependent processes such as plastic deformation.

Their Transmission Electron Microscopy (TEM) results showed fine equiaxed grains and the polytype was found to be primarily 6H. The short time span did not allow excessive grain growth. However, the

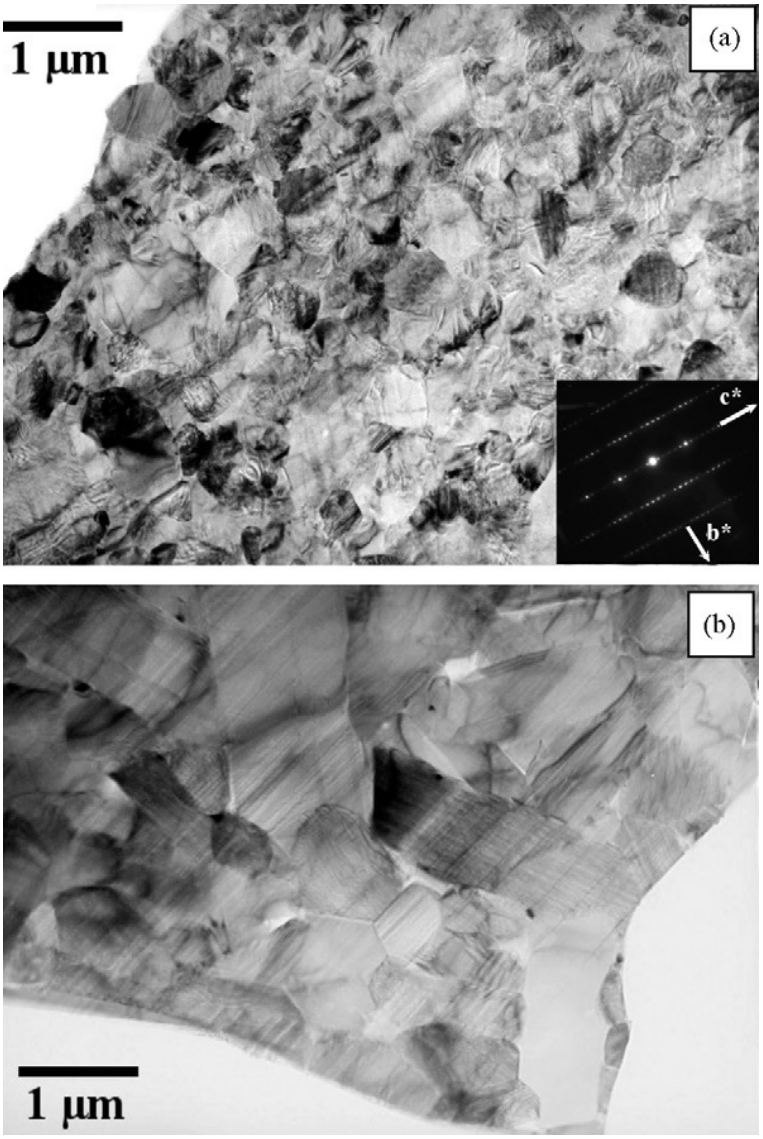


Figure 2.12.: TEM micrographs obtained on the samples sintered by SPS. (a) Pure SiC(6H polytype diffraction pattern in the bottom right hand corner), (b) SiC+C+B. Images from Maitre et al. [15]

addition of free boron and free carbon led to even higher relative densities (98.8%). Spatially resolved Electron Energy Loss Spectroscopy (EELS) of the grain boundary showed that in the case of free boron, a

monolayer of boron was present on grain boundaries which enhanced grain boundary diffusion. This helps in sintering. It also promotes point defects in α-SiC lattice which again enhances diffusion. In the case of boron carbide, it forms a liquid phase by dissolving the silica present on the surface of the SiC powder particles. This liquid phase was present on the grain boundaries and enhanced the grain boundary migration. It promoted abnormal grain growth as well. They also agreed that the addition of free carbon leads to the reduction of surface silica as was claimed by Clegg [14]. The TEM images from Maitre et al. [15] are shown in 2.12.

Another interesting observation from the literature on the SPS sintering is the apparent reduction in the sintering temperature [58]. Lee et al. [58] reported sintering SiC using SPS at 1670 °C using 40 MPa pressure as compared to 1950 °C using pressureless sintering. Zhou et al. [55] sintered SiC with aluminium carbide and boron carbide at 1600 °C using 47 MPa pressure. However, it is not clear whether it is due to the applied pressure which is usually very high compared to the pressure applied in a hot press or if it is due to the temperature inside the die being higher. The temperature is usually measured from the surface of the die with a pyrometer which would be significantly lower then the actual temperature at the particle contacts.

Attempts have been made to either measure or calculate the actual temperature of the powder inside the die. Molenat et al. [59] tried to use FEM to predict the temperature inside the die during the sintering using SPS. They carried out sintering using three different materials be-

longing to conductors (TiAl), insulators (Alumina) and semi-conductor (SiC) catagories of materials to see the effects of conductivity of the samples on the temperature differences between outside and inside the die. They measured the temperature on the outside using a pyrometer whereas the temperature inside the die for TiAl was measured using the phase transformation in this material which takes place above a specific temperature. The temperature inside the die for alumina was measured by K-thermocouples were placed at various distances away from the sample. The temperature measurements inside the die for SiC were carried out using a platinum thermocouple. They found the differences between the temperature of the external wall of the die and the sample to be around 100 °C. They also showed that the difference in the temperature was more (4.2%) for the semi-conductor material compared to the insulator and conductor materials (2.2%). However, the results of a temperature study by Yucheng and Zhengyi [60] found that actually the temperature difference between the inside and the outside of the die for a conducting material is lower then that of semi-conductor and insulator. For the later , the difference may reach values as high as 450 °C under certain conditions. They measured the temperatures of the inside of the samples using thermocouples in the centre of the samples as well as on the boundary between the sample and the die as well as on the outside of the die. Tiwari et al. [61] also agree with the conclusions of Yucheng and Zhengyi [60] with regards to the temperature differences between inside the sample and the die being more for insulators than a conducting materials. Grasso et al. [62]

studied the effects of pressure on the temperature distribution during the spark plasma sintering. They found that increasing the pressure leads to small reduction in the temperature distribution.

2.2. Use of indentation tests to measure mechanical properties

2.2.1. What is hardness?

Measuring hardness is quite simple and has been performed for over a hundred years [63]. Moh's introduced a set of 10 materials and defined the hardness of a material by checking which of the reference materials could scratch it. Since then hardness has beeen characterised using various indentation tests which are similar in practice.

Typically, an indenter is pushed into the surface of a sample with a certain load and the size of the impression left by the indenter on the surface is measured. Then the hardness is simply defined as applied load over the (projected) area of this impression; which is given by equation 2.5.

$$H = \frac{F}{A} \tag{2.5}$$

where F is applied load, H is hardness and A is the projected area of the impression on the surface of the sample.

A range of indenters have evolved historically: the Vickers pyra-

mid, the Berkovich pyramid, spheres, and elongated pyramaids such as Knoop. Different indenter shapes give different hardness values for the same applied load [64, 65]. The most commonly used geometries for ceramics are four-sided Vickers, three-sided Berkovich and Knoop indenters. For the former two, the projected area increases in the same way with distance from the tip of the indenter and therefore they are often considered to be equivalent. Assuming perfect tip shapes, the expressions for Vickers indenter and Berkovich indenter shapes are given in equations 2.6 and 2.7 respectively [66].

$$A = 4h^2 tan^2\theta \tag{2.6}$$

$$A = 3\sqrt{3}h_t^2 tan^2\theta \tag{2.7}$$

where A is the area of indent, h_t is depth of the indenter and tan θ is the half angle of the indenter tip. The angle for vickers is 68° and for berkovich is 65.3°. If these angles are put into their respective equations then the resultant expression is the same for both of them. This makes both equations 2.6 and 2.7

$$H = \frac{F}{24.5h_t^2} \tag{2.8}$$

where H is the hardness, F is the applied load in Kg and h is the depth of the indenter.

The use of a three sided Berkovich indenter is preferred over the

4 sided Vickers indenter for nano-indentation since it is practically impossible to grind a four-sided pyramid which meets perfectly at a single point.

The knoop indenter [67] is also used to measure the hardness. It is similar to the Vickers indenter except that the Pyramid has unequal lengths such that one diagonal is 7 times smaller then the other. It is used for studying highly brittle materials as it causes less damage then the Vickers indenter.

A spherical indenter is also used sometimes. Spheres also reduce the chances of cracking due to lack of stress concentrators [68]. However, the depth to area ratio is not constant due to its spherical shape [66]. It is also dificult to measure the area accurately due to the lack of corners.

Micro and macro indentation is carried out using Vickers indenter tips where the load applied is large and the impression left on the surface of the sample can be measured using an optical microscope hence hardness can be measured. On the other hand, nano-indentation is used where small loads are applied and the size of the indent is measured through the knowledge of the shape of the tip and the depth it goes into the solid using depth sensing techniques. This method was developed by Oliver and Pharr [69]. This method also calculates the stiffness of the material using the initial slope of the unloading curve.

The plastic deformation during indentation has been used quite effectively to measure the yield stress of the material. Various attempts have been made to link the hardness with the yield stress of the ma-

terial. The validity of these models, however depends on the ratio of stiffness to yield stress of materials. Tabor [63] went as far as to say that hardness is simply the measure of the yield stress in metals and he found that hardness is 3 times the yield stress. Swain and Hagan [70] argued that the plastic deformation in a brittle material can be observed at room temperature giving as an example a scratch test on glass.

However, apart from the plastic and elastic deformation, hardness can also be influenced by phase transformation [71–74], densification [75], or porosity [76] in the sample.

Cracking has been observed in ceramics during and after the indentation. This cracking has been used to measure the toughness [21], [77], as well as to measure the defect distribution [78].

2.2.2. Measuring the resistance to plastic flow

Tabor [63] pointed out that mean pressure between the indenter and the sample (in his case a metal) can be used to measure the hardness as pressure is simply load over the area. Since the impression made in the metal is permanent, he argued that there must be a connection between the mean pressure and yield stress.

Tabor [63] argued that the indentation process is similar to the compression test where only 1/3rd of the hydrostatic pressure is used in the plastic deformation. He [63] also noticed that work hardening takes place when the metals deform during the indentation process hence as

the strain increases, yield stress increases. Therefore, he carried out experiments on work hardened metals in the region where yield stress is nearly independent of the plastic strain and found that the hardness for metals is 3 times the yield stress for a rigid perfectly plastic solid. It is used quite commonly to calculate the yield stress from hardness in metals. However, Marsh [79] from his work on brittle glasses found that perhaps Tabor's approximation for yield stress and hardness is not true for ceramics due to their high yield strength relative to their elastic modulus. He concluded that the conversion factor between hardness and yield stress depends on the plastic flow in that particular material.

While Marsh [79] offered an explanation for thecause of the change, he was not capable of quantifying the effect and had to resort to fitting to experimental data. Johnson [80] introduced a different treatment and predicted that the proportionality between hardness and yield strength would depend on yield strength to elastic modulus and the inclination angle of the indenter.

Finite element calculations carried out by Cheng and Cheng [81] tried to find the middle way between the Johnson [80] and Hill et. al.[82] work. They carried out simulations of indentation with various yield stresses and Young's modulus values. They confirmed that the ideas following on from Marsh [79] were correct but none of the descriptions was very accurate. Vandeperre et al. [83] introduced a different modification to the expanding cavity model to account for the lower amount of material displaced with Y/E increases due to surface deformation. Their treatment agreed reasonably with the finite

element calculations of Cheng and Cheng [81] for ceramics.

The relationships between yield stress and hardness has been found for various classes of materials including ceramics. This can be exploited to measure the yield strength of ceramics near room temperature, which is very difficult to do in any other way.

2.2.3. Measurements of toughness

Any process that induces cracks to form, should in principle also allow to measure the resistance to crack propagation. Since in ceramic materials, cracking near indents is very common, it is not surprising that methods have been developed to determine the toughness of ceramics from indentation cracks. The process of crack formation and propagation has been explained by Lawn and Wilshaw [84] and is summarised below.

Firstly, cracks have to initiate and then in a second stage these cracks propagate. The initiation of the cracks is either from pre-existing flows or from a stress concentration. Sharp indenters such as Vickers or Berkovich indenters cause a strong stress concentration near their top and therefore generate cracks at lower loadsciteMorris:2004th. In the case of a sharp indenter (conical, pyramidal) the crack starts from the bottom of the indent roughly from the edge of the plastic zone as the tensile stresses there are highest. As the load is increased, the crack grows. This crack is known as the median crack. In the next stage when the unloading starts, this median crack closes and the side

branches from the median cracks grow. These cracks eventually end up on the surface and are a cause of chipping. These cracks are known as lateral cracks. Various median cracks can appear at the same time depending on the flows as well as the loading and stresses forming a star like pattern on the surface and various chippings [84].

Another type of cracking is the cracks on the surface. They form during loading as well as after the unloading from the corners of the indents. If the cracks only exist near the surface, they are known as lateral cracks of the Palmqvist type. Sometimes these cracks join up underneath and through the indent and are then termed half-penny cracks. Schematic of various cracking systems are shown in figure 2.13.

Cracking from the indentation is an indication of the toughness of the material. Shorter cracks occur in tougher materials. This has been exploited by various researchers to find the indentation toughness of the material through the method of indentation. The main motivation has been the relative ease of the testing method unlike other traditional toughness measurement methods of 3 point and 4 point bending tests and the problem of introducing a sharp notch. Also it is useful in measuring the toughness of small samples where traditional toughness measurement methods cannot be applied [86].

Various equations have been derived linking size of the indent, crack lengths, load applied and modulus of the material. Dub and Maistrenko [87] have reviewed the expressions used for measuring toughness. Various researchers [77, 88–94] have found relationships between the crack lengths c, size of indent a, hardness H, modulus E, and applied loads

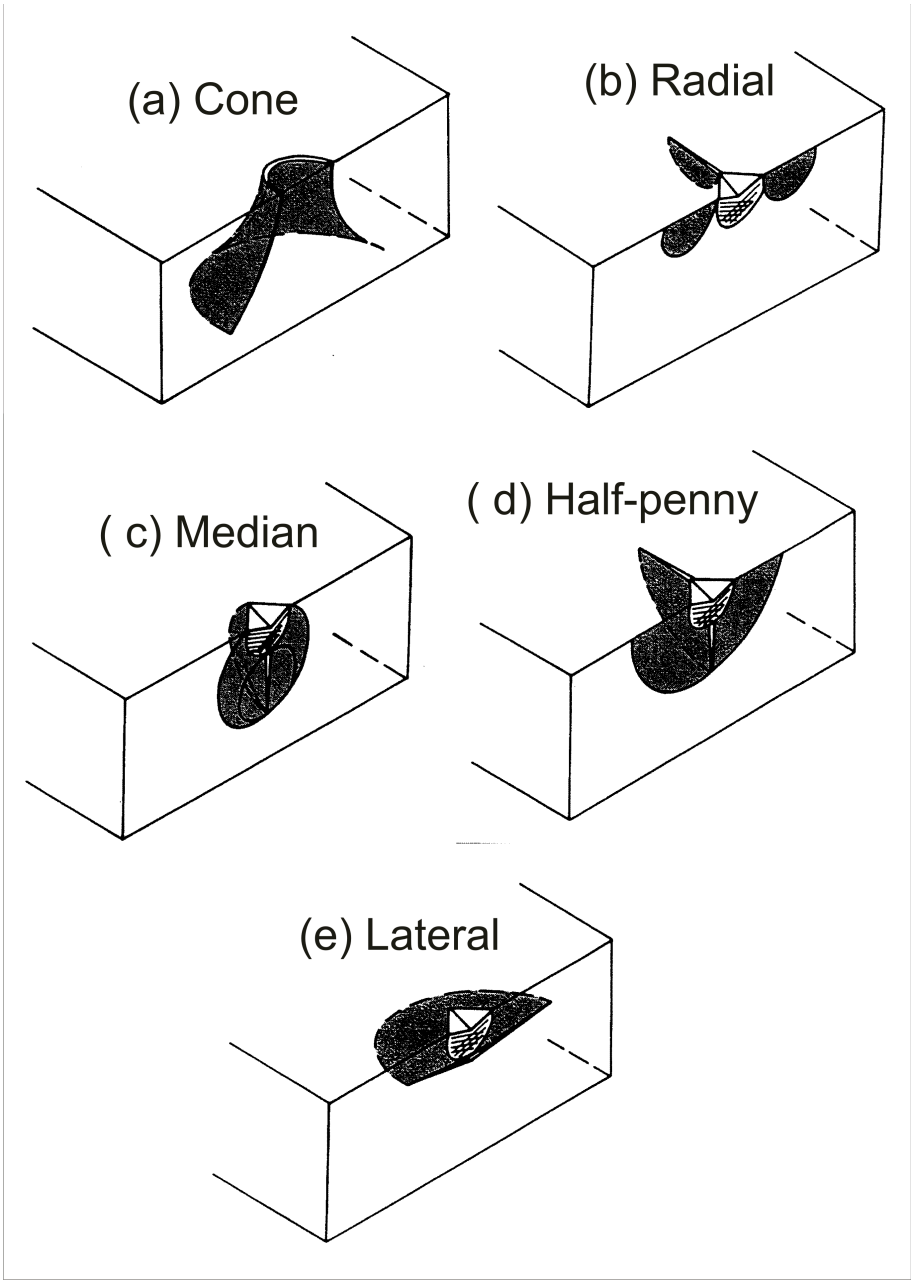


Figure 2.13.: A schematic of various cracks that are formed in and around the indent during and after the indentation. Images taken from Cook and Pharr [85]

F. Lewis et al. [95] proposed the equation 2.9

$$K_{1C} = \left(\frac{1}{7}\right) \cdot \frac{F}{c^{\frac{3}{2}}} \tag{2.9}$$

where K_{1C} is fracture toughness, F is the applied load and c is crack length measured from the centre of the indent.

However, more advanced equations incorporate the hardness and the size of indent to measure the toughness.

Most commonly used methods include the method of Niihara [96] and Anstis et al.[77] given in equations 2.10, 2.11 and 2.12. However, these different equations and models make different assumptions related to the crack systems.

$$K_{1C} = 0.016 \cdot \sqrt{\frac{E}{H}} \cdot \frac{F}{c^{\frac{3}{2}}} \tag{2.10}$$

where E is youngs modulus, H is hardness, F is applied load and c is the crack length.

The value of 0.016 has been calculated from fitting the literature data onto the model. It is only valid in a specific load regime. For better accuracy of the results, calculation of this fitting parameter will have to be carried out for the material being tested in the appropriate load regime.

Niihara [96] tried to solve this problem by deriving two separate equations for two different crack systems.Niihara [96] found that in the presence of Palmqvist cracks, the correlation between crack lengths, c and the toughness was better using

$$K_{1C} = 0.018Ha^{\frac{1}{2}} \left(\frac{E}{H}\right)^{\frac{2}{5}} \cdot \left(\frac{c}{a-1}\right)^{\frac{-1}{2}} \tag{2.11}$$

whereas when the crack system becomes a half-penny crakc-which requires higher loads

$$K_{1C} = 0.028Ha^{\frac{1}{2}} \left(\frac{E}{H}\right)^{\frac{1}{2}} \cdot \left(\frac{c}{a}\right)^{\frac{-3}{2}} \tag{2.12}$$

is a more accurate expression, where E is modulus of the material. Niihara [96] developed the equations for the short Palmqvist cracks that have low c/a ratios.

These last two equations 2.12 and 2.11 are used most often for measuring indentation.

Their experiments showed that equation 2.12 correlates well with the data where the c/a ratio are greater then 2.5 whereas the equation 2.11 correlates well with the data where the c/a ratio is less then 2.5 (i.e. short cracks). This gets more complicated as the crack systems change with increasing load. Palmqvist cracks get longer with load and eventually become 'half-penny' cracks as was found by Jones et al. [97]. The use of this equation requires detailed knowledge of the crack system present in the sample at the load at which the toughness measurements are being carried out. It makes this test complicated.

2.2.4. Indentation size effects

Measured hardness drops with increasing the load [49]. This simply means that the ratio of size of indent and load is not constant. This

reduction in hardness with load and therefore also with the size of the indent is termed the Indentation SIze Effect (ISE)[49]. Although the initial work on plastic deformation did not predict the drop in hardness when it is controlled by plastic flow [63] however, Tabor [63] did find an increase in hardness with reduction in load in metals. He argued that the surface of metals is harder then the bulk. When small loads are applied, only the surface layers are being indented and hence the higher hardness. Since then, various explanations have been given in the literature. A few approaches used to quantatively describs ISE are Mayer's power law([98] (equation 2.13), Proportional Specimen Resistance (PSR) (equation 2.14) Modified Proportional Specimen Resistance (MPSR) [99], Elastic recovery theory [100] and Hays and Kendall approach [101].

Mayer's ([98] power law is data fitting model to describe the relationship between the hardness and size of indent

$$F = \varphi d_i^{\xi} \tag{2.13}$$

where F is the applied load, d is the length of diagonal, φ and ξ are fitting parameters. Li and Bradt [102] suggested that the load and diagonal of the indent are related through a polynomial relationship given in equation 2.14

$$F = a_1 d_i + a_2 d_i^2 \tag{2.14}$$

where F is applied load, d_i is length of indent diagonal and a_1 and

a_2 are parameters constant for material related to elastic and plastic deformation properties respectively [103].

Gong et al. [99] proposed that PSR model could be improved by adding an extra a_0 term to take residual surface stress into account. This (MPSR) model is given in equation 2.15

$$F = a_0 + a_1 \cdot d_i + a_2 \cdot d_i^2 \tag{2.15}$$

Hays and Kendall [101] suggested a minimum load in Knoop hardness above which the permanent deformation takes place. However, perhaps this model is valid for very small laods (in mN scale) and it does not describe the ISE at micro or macro indentation region.

Elastic recovery theory is based on the elastic recovery of the indent once the indeter is removed. Tarakanian et al. [100] suggested that the measured indentation size should be corrected for this elastic recovery using the following equation 2.16.

$$H_e = \Upsilon \frac{F}{(d_i + d_{ie})^2} \tag{2.16}$$

where H_e is the hardness corrected for the elastic recovery, d_ie is the correction in the indent size d_i due to the elastic recovery, Υ is a constant which depends on the shape of the indeter tip and F is applied load. However, they did not comment on its applicability at higher loads. It does not explain the indentation size effects.

Various Plastic flow controlled ISE have been proposed. These include the theory of Strain Gradient Plasticity [104], Dislocation Starva-

tion Theory, elastic recovery theory [103] and the deformation through discrete bands proposed by Bull et al. [98].

Strain Gradien Plasticty (SGP) has been used as an explanation for indentation size effects.[104–108]. Fleck et al. [105] proposed that increase in hardness at the smaller depths in metals can be explained by the large strain gradient which necessitates the formation of geometrically necessary dislocations. Gao and Huang[104] has defined them as the dislocations necessary to acccomodate the lattice curvature in the event of non uniform plastic deformation. The density of these dislocations is higher in the small indents than in the larger ones which makes it harder for the dislocations to move in the small indents making it harder for plastic deformation to take place and hence the sample appears harder.

Ren et. al. [109] experimented with magnisium oxide (MgO) single crystal, polycrystalline MgO and yttria stabilized zolycrystalline cubic zirconia (YCPZ) at high temperatures and found that ISE reduce with increasing temperature. They concluded that this is do with the H/E ratio where H is hardness and E is Young's modulus. E remains constant with increasing temperature whereas H drops considerably hence H/E ratio changes leading to a change in the ISE behaviour. They plotted H/E against the Power Law and PSR model and found that they were correlated. They also plotted the H/E of various other materials (SiC, Al_2O_3, B_4C, TiC, Silver steel) and found that they all correlated to both of these models. They concluded that elastic recovery is responsible for ISE in these materials under the conditions

of the test (Temperature of 20 °C to 600 °C for MgO single crystal, YCPZ) as this provided the best fit for the data. However, they did not comment on the presence of any cracks in the indents.

Peng et al. [110] analysed nanoindentation data from soda-lime glass, zirconia (ZrO_2) and silicon nitride using Power Law, PSR and MPSR. They concluded that all of these models give similar answers as the empirical equations used in these models are very similar. They argued that Power Law and PSR models just describe the trends whereas meaning of parameters in MPSR model are much more complex then originally proposed.

Apart from the plasticity effect on the increase in hardness at lower loads, one school of thought is that the drop in hardness with increasing load is simply due to the cracking in ceramics [111]; a review of which is given by Sangwal [112]. Sangwal reported that there is a correlation between the crack lengths and the drop in hardness suggesting that perhaps the cracking is the cause of ISE.

The argument is that indentation response of the material depends on the load. At small loads, indentation response is elastic and plastic deformation. However, as the load is increased, the indent starts to crack. The cracking provides a stress relaxation mechanism and opens up the indent allowing the indenter tip to penetrate deeper. These cracks grow as the applied load increases until the crack length reaches a steady state. This is correlated to the drop in hardness, which is quite severe initially but then a steady state is reached.

A considerable amount of literature exists on this issue however, the

real origin of ISE is a controversial topic. Perhaps there are various reasons and the significance of any particular theory depends on the material itself.

2.3. Conclusions

SiC is known to be difficult to sinter due to the covalent bonding, low self diffusion and the surface silica. It has been sintered using carbon and boron as sintering additives resulting in a low toughness (around 4 MPa$\sqrt{m}$). Al was introduced in the system in conjunction with boron and carbon leading to improvements in toughness through the formation of an amorphous film on the grain boudaries.

SiC was also sintered through a pressureless route using combination of oxides (alumina, yttria, silica) as additives at their eutectic compositions to reduce the sintering temperature. The toughness values obtained were close to those obtained in the ABC system. However, they all had problems with reaction with SiC leading to various gases and reaction products which were detrimental for the sintering process hence the need for the powder bed.

When AlN was used as a replacement for alumina, the powder bed was not needed. It was also used as a replacement for Al in ABC system for the purpose of improving the hardness response of SiC. The literature suggests that the use of AlN as a sintering additive in SiC is found to be beneficial in improving the mechanical properties due to the formation of the SiC-AlN solid solution. However, the exact

mechanism of the densification or the formation of the solid solution has not been studied.

It has also seen that hardness is a system property; it depends not only on the material being tested but also on the properties and shape of the indenter. However, the variety of responses means that hardness tests also offer opportunities to measure a range of material properties: the resistance to plastic flow, the elastic modulus and the toughness. The hardness measured at different loads with the same indenter is also different and although there is a wide range of explanations, this topic remains controversial.

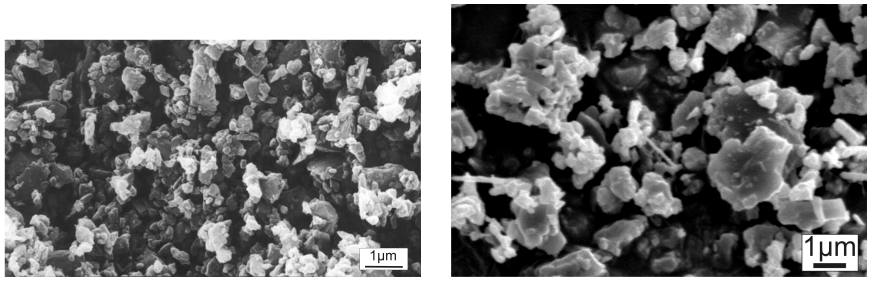
SiC is one of the hardest ceramics. However, it it is brittle. Attempts have been made to improve its toughness using various densification and reinforcement methods. The use of AlN as a sintering additive has been an interesting one because of the solid-solution it forms with the SiC. However, the effect of this solid solution on toughness and hardness needs to be investigated.

3. Experimental Methods

This chapter contains an overview of the experimental techniques and methodologies that have been used to determine how AlN redistributes in the microstructure, the sintering of AlN doped SiC and its response to indentation at different scale.

3.1. Powder mixing

One of the most fundamental aspects of ceramic processing is achieving a homogeneous mixture of the ingredients since poor mixing leads to variations in the microstructure. The raw materials used to produce powders mixtures in this work include α-SiC powder (type UF15 from H.C. Starck), an AlN powder (type C from H.C. Starck), yttria powder (Yttrium oxide powder 99.99% pure from Ventron Alfa Produkte.Karlsruhe, Germany) and a phenolic resin powder (CR-96 Novolak, Crios Resinas, Brazil). To produce mixtures, powders were weighed in the quantities required for the compositon that is being prepared. Silicon carbide powder was put into a beaker and slurry was made by adding methyl ethyl ketone (MEK). The beaker was placed on



(a) α-SiC (b) AlN

Figure 3.1.: SEM images of α-SiC from suppliers and AlN powders taken using SEM 5610 at Imperial college London

a magnetic stirrer. Then the rest of the ingredients were slowly added into this slurry. Phenolic resin, where needed, was always added as a last component. The stirring continued for 10 minutes after the addition of all the ingredients.

Mixing was carried out using a ball mill. Silicon nitride (Si_3N_4) balls of 10mm diameter were used as milling media. They were weighed to be 1.5 times the total amount of powders (e.g. 75 grams of milling media to 50 grams of powder). Milling media and slurry containing powders was put in a PET (PolyEthylene Terephthalate) bottle, sealed and placed on a ball mill.

After 24 hours of mixing, the slurry containing powders and milling media was poured out of the bottles through a sieve to remove the milling media. The slurry was then dried using a rotary evaporator (BUCHI Rotavapor®-210/215 Buchi Labortechnik AG, Switzerland). (see Figure 3.2)

The rotary evaporator evaporates the liquid in the slurry with the aid of heat and vacuum while rotating the sample to avoid caking of

Table 3.1.: Properties of the raw powders as provided by suppliers.

Powder	**α-SiC**	**AlN**	**Y_2O_3**
Grade	H.C. Starck UF-15	H.C.Starck C	Alfa Aesar 99.99% REO
Oxygen content (wt%)	1.5	0.1	-
Specific surface area (m^2 g^{-1})	14-16	4-8	-
Green density at 100 MPa (g cm^{-3})	1.55-1.75	—-	—-
Particle size (μm)			10
D 90%	1.2	0.2-0.35	
D 50%	0.55	0.8-1.8	
D 10%	0.2	2.3-4.5	



Figure 3.2.: Rotary evaporator. (1) Rotating flask, (2) Water tub, (3) Condensor. (4) Cooling water and circulation pump), (5) Liquid collecting flask, (6) Vacuum pump tube, (7) Power supply for water circulation pump

the drying slurry.

The water temperature was set at 90 °C and rotation speed of the flask was 80 rpm (dial setting 4 on the instrument). At the start of the drying, vacuum was created within the chamber and then the vacuum pump was turned off. The vacuum pump was turned on again when most of the liquid had evaporated but the powder in the flask was still slightly damp. This removed the last remaining liquid and fully dried the powder. The dried powders contained soft agglomerates from the rolling movement inside the evaporation flask. In mixtures containing phenolic resin, the agglomerates were found to be harder, and these were broken up using a pestle in a mortar before use.

3.2. Pellet pressing

Uniaxial pressing tests were carried out to assess the processing characteristics of the powder after milling and drying. A stainless steel die with internal diameter of 12 mm was used and the applied pressure ranged between 37 MPa to 740 MPa. The pellets remained under pressure for 20 seconds before releasing the pressure and removing the pellets from the die. The density ρ, was calculated by measuring their diameter ϕ, height l, and mass m, as given in Equation 3.1.

$$\rho = \frac{m}{\frac{\pi d^2}{4} \cdot l} \tag{3.1}$$

The rule of mixtures was used to calculate the theoretical densities

of the pressed pellets:

$$\rho(total) = f(AlN)\rho(AlN) + f(SiC)\rho(SiC) \tag{3.2}$$

where ρ (total) is the theoretical density of the composition, ρ (AlN) is the theoretical density of AlN (3.3 Mg m^{-}3), f (AlN) is the volume fraction of AlN in the composition, ρ (SiC) is the theoretical density of SiC (3.21 mg m^{-3}) and f (SiC) is the volume fraction of SiC in the sample. The theoretical density of yttria was taken as 4.8 Mg m^{-3}). The density of resin was not taken into account.

Measured densities were divided by calculating theoretical densities and multiplying by 100 to find the percentage theoretical densities.

3.3. Sintering and Densification

3.3.1. Pyrolysis of powders

For compositions containing phenolic resin, the resin was pyrolysed prior to the sintering. To guide the selection of the pyrolysis temperature, thermogravimetric measurements were carried out. Powdered samples of α-SiC (particle size of 0.5 μm), α-SiC with 3 wt% C (around 6 wt% resin), and α-SiC with 3 wt% C and 3.75 wt% AlN (particle size of 0.8 μm) were heated up to 1500 °C at 1 °C min^{-1}in a standard TGA (NETZSCH STA449C Jupiter).

The TGA traces given in figure 3.3 show that the resin starts to char around 400 °C and AlN starts to oxidise at around 700 °C as can be

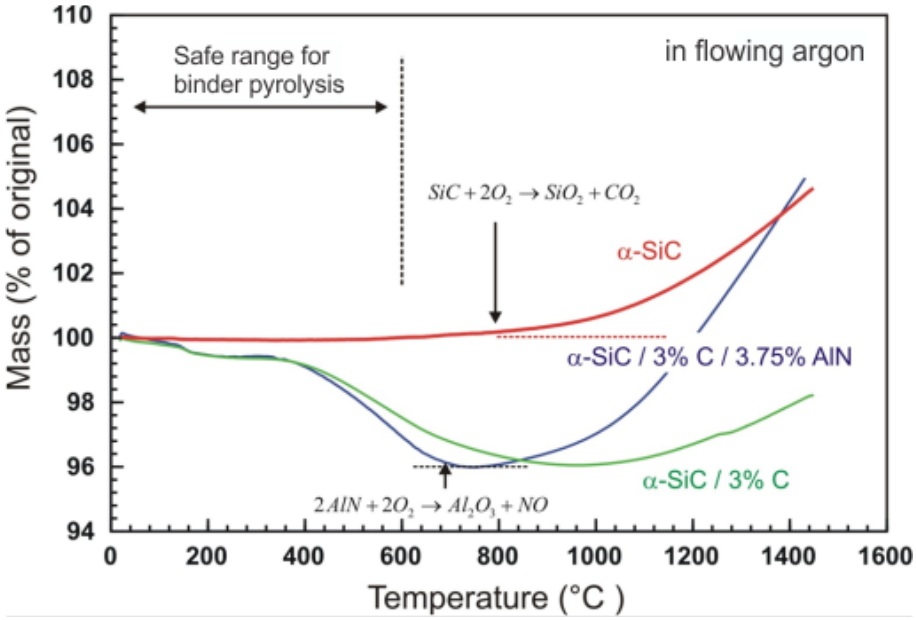


Figure 3.3.: TGA traces of α-SiC, α-SiC + resin and α-SiC + resin + AlN.

seen from the increase in mass for the mixture containing AlN in figure 3.3. In order to limit the risk of oxidising the AlN, the temperature to char was set at 600 °C. Pyrolysis consisted of heating the powder in flowing argon to 600 °C at 10 °C min^{-1}. The furnace was held at 600 °C for 2 hours before cooling it at 25 °C min^{-1} until natural cooling by convection prevailed.

3.3.2. Hot pressing (HP)

HP is a technique used to sinter ceramics, which are difficult to densify. It involves applying pressure at temperature to assist sintering. The experiments were carried out in a FCT hot-press at the Department of Metals and Materials Engineering, Katholieke Universiteit Leuven

(KUL) in Belgium. The temperature was controlled by a pyrometer (Impac 140) and a Mitutoyo micrometer follows the ram movement during processing. The sintering tool of the hot press is shown in Figure 3.4. A graphite heating element surrounds this tool and pressure is applied from the top by a cooled hydraulic ram. Ram movements were recorded during sintering to estimate the density during sintering. The sample size was a 30 mm diameter disk with varying thickness between 3-5 mm. In the later stages of the research, a large size (60 mm diameter) sample of SiC was sintered using a similar FCT hot press at FCT in Germany.

For the first trial, the graphite pieces were coated with BN to avoid sticking of the sample to the die material. However, upon unloading after cooling, the sample could not be removed from the graphite cylinder. Hence, for the rest of the trials, a circular disc of graphite paper was placed above and below the SiC powder. Despite this, the samples continued to adhere to the graphite die discs.

Three different sintering schedules were tried to densify SiC. The details of the sintering schedules used in this thesis are given in table 3.3. HP was also used to partially sinter two SiC samples. They were heated to 1700 °C and 1850 °C in HP and then cooled as fast as the hot press allowed (around 100 °C min^{-1} initially).

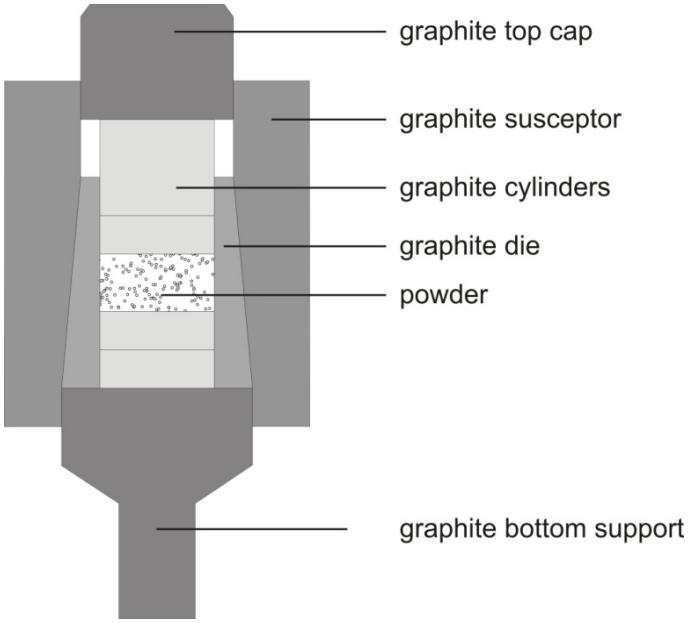


Figure 3.4.: A schematic of sintering tool used in the Hot Press.

3.3.3. Spark plasma sintering (SPS)

In SPS, ideally the green body itself is the heating element. A voltage is applied across the green body so that a current flows through it. Relatively high electrical resistance at the contacts between the particles means they heat up locally where diffusion is needed, which accelerates the diffusion and formation of necks. The lower thermal mass of the system allows for higher heating and cooling rates, and pressure can also be applied. In the case of samples with low electrical conductivity, the current flows through the die which then indirectly heats the sample.

Powder is placed in a graphite die and a graphite paper is wrapped between die and powder to avoid sample sticking to the die. It is lightly pressed by using a cold uni-axial press. Then this setup is placed in the

SPS. Ram movement, vacuum level, time, currents and temperature of the die were recorded automatically which were used to plot the densification curves.

Initial SPS trials were performed at KUL in Belgium. However, most of the SPS work was carried out at the Nanoforce laboratory in Queen Mary University of London. Discs of 20mm diameter with a thickness of around 3 to 5mm were sintered. the sintering schedule is given in table 3.3.

3.3.4. Density measurements

Initial estimates of the density of the sintered samples were made during the sintering experiments by recording the ram movements of the sintering equipment as mentioned earlier (section 3.3.2). Detailed density measurements were required to establish the level of porosity in the sintered samples. For this purpose, Archimedes' method was used.

Density is simply mass (M) of the sample divided by its volume (V):

$$\rho = \frac{M}{V} \tag{3.3}$$

The Archimedes principle states that any object immersed in water will feel an upward force equal to the volume of the displaced water. This force is called buoyancy.

$$M_w = (\rho - \rho_w)V \tag{3.4}$$

where M_w is mass of sample when it is fully immersed in water, ρ is

the density of the sample and ρ_w is the density of the water.

Eliminating volume from equation 3.4 using equation 3.3 and solving for ρ gives:

$$\rho = \left(\frac{M}{M_w - M}\right)\rho_w \tag{3.5}$$

However for a porous body, water can penetrate into the open pores and reduce the volume of the water displaced yielding increased and optimistic density values. This problem can be overcome by allowing the sample to saturate and taking the volume of the water in the pores into account during the calculations.

In this method, first the mass of the dry sample was measured. The samples were left in a drying furnace at 120 °C overnight before the dry mass measurements were made. Then the sample was immersed in water and allowed to saturate. This process was made more efficient by employing a vacuum pump and forcing out any air bubbles present in the pores. The mass of the sample when it was saturated and submerged in the water were measured. The mass of the saturated sample was also measured after taking it out of the water and carefully removing the water from the surface of the sample. Now the only water left in the sample is that in the open pores. Equation 3.6 can be used to calculate the density of the sample including the open porosity in the volume.

$$\rho = \left(\frac{M}{M_w - M_s}\right)\rho_w \tag{3.6}$$

where ρ_w is the density of water, ρ is sample density, M is the mass of dry sample, M_s is the mass of saturated sample and M_w is the mass of submerged sample.

Then this density can be divided by the theoretical density to calculate the relative density of the sample as a percentage of the theoretical density. The theoretical density was calculated by using the rule of mixtures on the nominal compositions and the theoretical density of AlN and SiC as given in equation 3.2.

The error in the density measurements comes from the error in measuring the mass. Also, if there are any pores that the water has not penetrated or the moisture in the dry sample lead to inaccuracies in results. The use of furnace to dry the sample and the use of vacuum pump to saturate the sample in water reduces the error.

The errors are associated with measuring the mass of the sample. The dry mass measurement error is the error of instrument ($\pm$ 0.0005 g) however, the error associated with the submerged mass is around 5 mg from experience of fluctuations in the mass during experiment.

3.3.5. Compositions and sintering schedules

SiC was hot pressed with addition of only AlN, AlN and carbon and only carbon. All these samples were sintered at 2045 °C using a hot pressing method. However, the sintering schedules differed in the heating rates, dwell times and intermediate dwells. A sintering schedule based on some literature [113] data with 30 minute dwells at 1700 °C

and 1850 °C (HP-Dwells) was initially tried. Intermediate dwells were used to allow the sample to reach equillibrium after certain chemical reactions at these hold temperature. Two further sintering schedules used were different in the time spent at the sintering temperature (HP-60 and HP-30). These sintering schedules were tried to see the effect of time at the sintering temperature on the AlN redistribution. Two interrupted sintering cycles were also tried to see the intermediate stage of AlN redistribution. Samples were sintered at 1700 °C and 1850 °C before cooling.

SPS was used to sinter samples containing SiC + 3.75 wt% AlN, and SiC + 3 wt% C + various amounts of AlN ranging from 0.75 to 3.75 wt%. The sintering temperature used was 2100 °C and the time spent at sintering temperature was 5 minutes.

A reference sample that shows the presence of liquid phase was sintered with AlN and yttria using SPS at 2100 °C as well as 1900 °C for 5 minutes. Details of the sintering schedules are given in the table 3.3 whereas the details of the compositions have been provided in table 3.2.

3.4. Characterisation techniques

3.4.1. Scanning Electron Microscopy (SEM)[114]

In SEM, a beam of electrons is accelerated towards the sample and images are formed by collecting either back-scattered electrons or sec-

Table 3.2.: The compositions sintered during this project

SiC type	wt%AlN	wt%C	wt%yttria
α-SiC	0	3	0
α-SiC	0.75	3	0
α-SiC	1.5	3	0
α-SiC	2	3	0
α-SiC	2.5	3	0
α-SiC	3.75	3	0
α-SiC	3.75	0	0
α-SiC	3.75	0	3

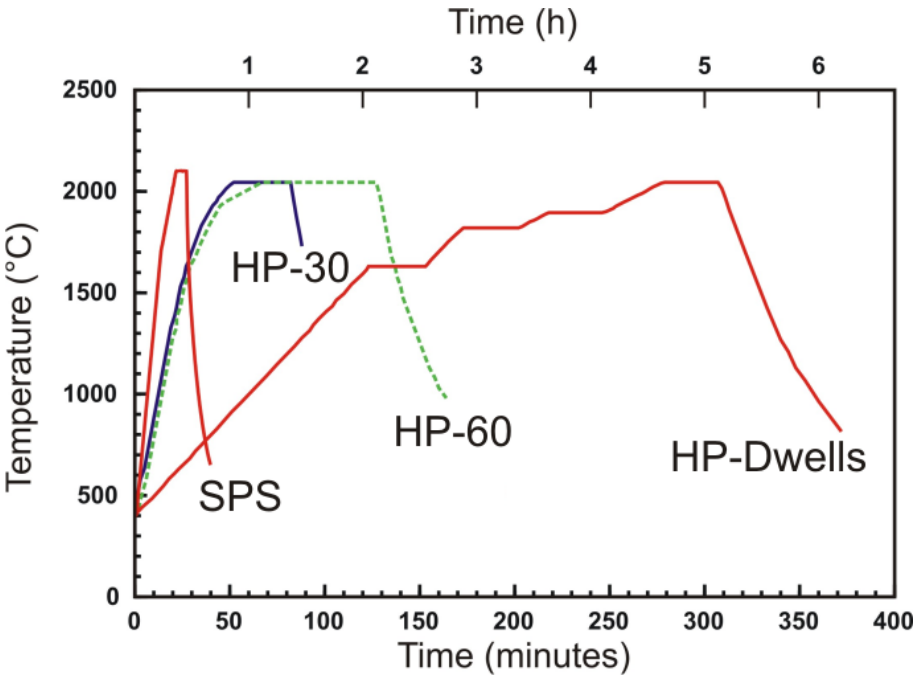


Figure 3.5.: Schematic showing the heating rates and temperatures used in various sintering schedules to densify SiC.

ondary electrons. Back scattered electrons are those that have simply bounced back off the atoms of the sample. They are high energy electrons and they are responsible for mass number contrast in the back-Scattered electron Image (BSI). Secondary electrons are electrons that

Table 3.3.: Table showing the in Hot Pressing schedules used with the method code that will be used to identify the sintering method used in each sample in the thesis.

Method code	Description
HP-Dwells	388-1630 °C, 10 °C/min, 6 kN load 1630 °C, 30 minutes, 6 kN load 1630-1820 °C, 10 °C/min, 6 kN load 1820 °C, 30 minutes, 10 kN load 1820-1895 °C, 5 °C/min 15 kN load 1895 °C, 30 minutes, 15 kN load 1895-2045 °C, 5 °C/min 15 kN load 2045 °C, 30 minutes, 15 kN load 2045-388 °C, 50 °C/min, 15 kN load
HP-60	388-1630 °C, 50 °C/min, 6 kN load 1630-1930 °C, 20 °C/min, 15 kN load 1930-2045 °C, 5 °C/min 15 kN load 2045 °C, 60 minutes, 15 kN load 2045-388 °C, 50 °C/min, 15 kN load
HP-30	388-1630 °C, 50 °C/min, 6 kN load 1630-2045 °C, 50 °C/min, 15 kN load 1930-2045 °C, 5 °C/min 15 kN load 2045 °C, 30 minutes, 15 kN load 2045-388 °C, 50 °C/min, 15 kN load
HP-1700C	388-1630 °C, 50 °C/min, 6 kN load 1630-1700 °C, 50 °C/min, 15 kN load 1700-388 °C, 50 °C/min, 15 kN load
HP-1850C	388-1630 °C, 50 °C/min, 6 kN load 1630-1850 °C, 50 °C/min, 15 kN load 1850-388 °C, 50 °C/min, 15 kN load
SPS	450-1700 °C, 100 °C/min, 5 kN load 1700-2100 °C, 50 °C/min, 10 kN load 2100 °C, 5 minutes, 18.97 kN load 2100-450 °C, 100 °C/min, 18.97 kN load

have been knocked off the atoms of the sample due to their interaction with the incident beam. Secondary Electron Images (SEI) give more information about the surface topography since the secondary electrons come from the outer 5-10 nm whereas BSI gathers information from as deep as 50 nm below the surface. X rays come from a few μm deeper into the sample. However, the exact depths of interaction volume depends on the voltage applied and the mass number of the sample. A diagram of interaction between incident beam and the sample is given in figure 3.6.

The instrument used in this study included a JEOL JSM5610 and a JEOL JSM6400 were used for EDX analysis and imaging. Sintered samples were polished using diamond paste (3 and 1 μm particle size) after grinding using diamond grinding wheels with grit size, 600, 800, and 1200. Green pellets and fracture surfaces were not ground or polished. Samples were then attached to aluminium sample holders using silver paint or double sided carbon tape. Samples were gold coated before the analysis using an EMITECH K550 gold coater.

3.4.2. Energy Dispersive X-ray Spectroscopy

Interaction between accelerated electrons and the sample leads to some of the electrons within the sample being forced out of their orbit into a lower orbit. They emit some radiation, which can be detected. This radiation can be detected with either Energy Dispersive or Wavelength Dispersive X-ray detectors. In EDX, the emitted photons are collected

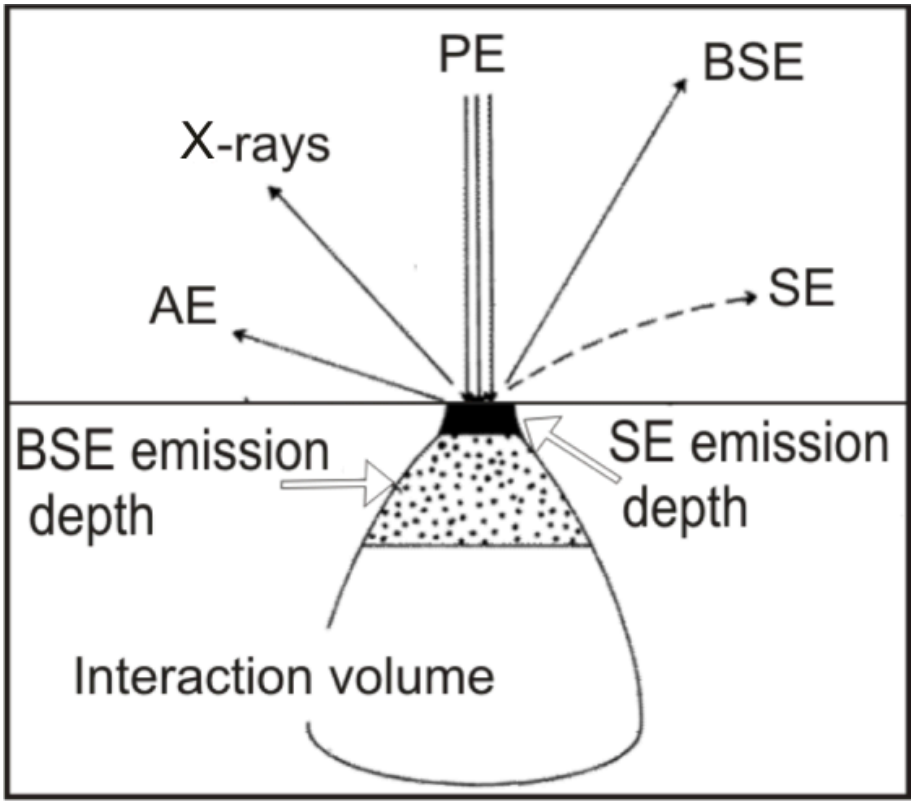


Figure 3.6.: Schematic diagram showing various signals that can be used for imaging and chemical composition of samples in SEM. SE: Secondary Electrons, BSE: BackScattered Electrons, PE: Primary Electrons, AE is Auger Electrons

as a function of their energy using EDX detectors which consist of a crystal cooled using liquid nitrogen. Absorption of a photon in the crystal leads to free electron becoming conductive hence an electric charge is produced. The X-ray absorption is thus converted into the electric charge of proportional size to the energy of the X-ray. The spectrum of photon intensity is analysed to get chemical information from the region of the sample under the electron beam.

The energy of the X-rays is detected, thus allowing the atoms in the

sample to be identified using Mosley's Law.

$$E(keV) = K(Z-1)^2 \tag{3.7}$$

where E is the energy of the X-ray, K is a constant and Z is the atomic number of the corresponding atom that X-ray has been emitted from.

Since the number of X-rays for specific atoms increases with concentration, estimates for the concentration of each type of atom are obtained. However, the accuracy of the results depends on the surface finish and the electrical conductivity of the sample. Bombardment of electrons on the surface leads to surface charging. More electrically conducting samples show better results so that for semi-conductors or non-conducting samples, a layer of gold, carbon or platinum can be applied to conduct the electrons away.

The principle of operation of EDX in the TEM is the same as in the SEM. However, the number of photons detected is quite low due to the small thickness (less then 100 nm) of the sample. The sample thickness has to be around 100 nm to make use of EDX in TEM as the sample always has to be electron transparent.

The second problem is the selection of area for the analysis is not very accurate which makes the analysis of specific locations quite challenging. Also, the spatial resolution of EDX is poor compared to the SE and BE electron signal. This is because of the depth from which the X-rays can escape from the sample. Also, some of the low energy X-rays are absorbed by the sample and the window of the detector. This

leads to inaccuracies in the measurements. This can be improved by using a better (thin windowed) detector. The detector used in the current work was a Ultra-thin window silicon detector which was available on both SEM and TEM (TEM 2010 system as well as SEM JSM840 and JSM6400). For the SEM, the sample surface roughnes can lead to inaccuracies in the measurements as well.

This method was the basis of finding the homogeneity level of AlN in SiC matrix which is described in section 3.4.6.

3.4.3. Focused Ion Beam (FIB) and Secondary Ion Mass Spectroscopy(SIMS) [115, 116]

FIB is similar to an SEM but instead of exciting the sample with an electron beam, a gallium (Ga^+) ion beam is used. The surface of the sample is bombarded with these ions and they result in sputtering of the atoms of the sample as their energies are considerably more then the energies usually associated with the electrons in the SEM. This makes the FIB a milling machine that can be used to cut sections out of the material at particular locations. This technique is now widely used to produce electron transparent sections for TEM analysis.

In SIMS, gallium ions knock out secondary ions and molecules from the surface. These secondary ions are detected using a magnetic sector detector as a mass-to-charge ratio by mass spectrometer. Apart from ions, electrons are also released as a result of the ionic collisions. Images can be made by either collecting electrons or ions.

The sputtering of the surface depends on various factors. The yield of secondary ions is strongly dependent on the electronic state of the material being analysed which leads to the complications for quantative analysis. Equation 3.8 is the SIMS basic equation.

$$I_s^m = I_p y_m \alpha^{\pm} \theta_m \eta \tag{3.8}$$

where I_s^m is the secondary ion current of species m, I_p is the primary particle flux, y_m is the sputter yield, $\alpha^{\pm}$ is the ionisation probability to the positive or negative ions, θ_m is the fractional concentration of m in the surface layer and η is the transmission of the analysis system.

y_m and $\alpha^{\pm}$ are two fundamental parameters. y_m increases with the mass, charge and energy of primary particle. The crystallinity and the topography of the sample surface also affects the sputtering yield.

This technique was employed as a characterisation tool to produce images of the microstructure and concentration maps of Al on the surface. It was also used to produce TEM samples by cutting and milling the samples with the ion beam, the details of which are given in the TEM sample preparation section (3.4.5). The samples were attached to an aluminium sample holder using silver tape to avoid the charge build-up on the sample surface that would affect the experiment. Low energy beams of 115 pA current were used and two types of information were retrieved: images formed by the secondary electrons and Al maps based on secondary ion yield. The SIMS used in this particular study was an fei FIB-SIMS 200T.

3.4.4. Transmission Electron Microscopy (TEM) [117]

TEM is another technique where an electron beam interacts with the sample and resultant effects give information about the microstructure. It works by analysing the interaction of the electron beam with the sample as it passes through it.

The interactions between sample and the electron beam can be divided into two categories: elastic and inelastic interactions. In elastic events, only the trajectories of the electrons are affected but their energies do not change. This results in the emission of forward diffracted and transmitted electrons as well as backscattered electrons. Inelastic interactions result in the transfer of energy to the sample however, the electron trajectories remain the same as before the electron interaction. This leads to the generation of heat in the sample as well as secondary electrons, auger electrons and X-rays.

Elastically and inelastically scattered electrons, secondary electrons and backscattered electrons are used for imaging whereas inelastically scattered electrons are also used for chemical analysis due to the characteristic energy loss during their interaction with the sample. This technique is known as (EELS) which has not been used in this study. However, the characteristic X-rays have been used for energy dispersive x-ray spectroscopy (EDX).

Lattice images are produced using High Resolution Transmission Electron Microscopy (HRTEM). The transmitted beam and one of the

diffracted beams are combined. The phase interference between both beams yields the periodic intensity fringes in the image. Under the appropriate conditions, the intensity of these fringes and the atomic planes from which the electrons are diffracted have one to one correspondence. In which case, the spacing of fringes and the atomic planes spacings are equivalent.

This is a powerful technique making it possible to examine the grain boundaries and phase interfaces. Lattice images were used to examine the grain boundaries to determine the presence of any intergranular phases. This means that both grains have to be in zone (i.e. atomic planes should lie parallel to the electron beam) for this experiment to be successful. The fringes from both grains are observed near the boundary. If there is an amorphous film present then these fringes will be absent whereas if there is a crystalline phase present then the fringes of distinctly different appearence will be observed.

The images were acquired with the help of Drs. Doni Daniel, Mahmoud Ardakani and Finn Giuliani.

3.4.5. TEM sample preparation method

For a material to be analysed in the TEM, the sample has to be thin enough that electrons can pass through it (around 100 nm). The sample has to fit in a 3mm diameter holder. Two sample preparation methods were used.

The first method uses traditional cutting, grinding, dimpling and

than finally ion polishing to cut and thin a section down to electron transparency.

The sample is cut to less than 3 mm diameter. Then it is ground to around 100 μm. This procedure is carried out using a grinding wheel and the sample is turned over during the grinding to make sure both sides are parallel. Then this around 100 μm thick section is dimpled using diamond paste in a dimpling tool (Gatan Dimple Grinder Model No. 656) until the centre of the dimple is around 15 μm thick. This dimpled sample is glued onto a 3mm diameter copper ring and placed in a Gatan Precision Ion Polishing System (PIPS) Model 691 which uses argon ions to mill the sample. There were two ion guns and the angle of the attack and the energy of ions can be changed to increase or decrease their efficiency. The beam was tilted by 6 $^\circ$ and the voltage was 3.5 keV. The angle of attack was gradually reduced to 2.5 $^\circ$ and the current was reduced to 2.5 keV. The sample was rotated at 4 rpm to achieve homogeneous milling and o avoid the formation of fringes. Argon gas was used as a source of ions. Its flow was controlled to give 16 μA current. The sample is taken off the ion polisher when a small hole appears in the centre of the dimple.

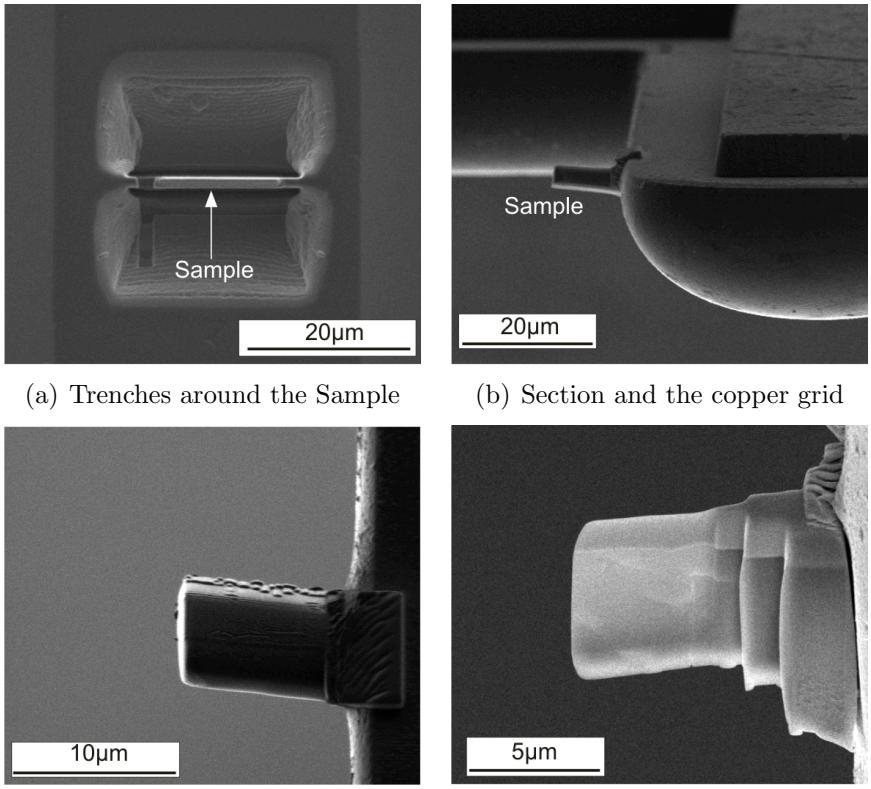
In the second method, a focused ion beam is used to prepare TEM sections from specific location i.e. under an indent or at a phase of interest.

In this technique, gallium ions are used to cut the section from the bulk of the sample. Since the gallium ions are destructive to the sample, a layer of platinum is applied before milling and cutting to protect

the surface of the sample as can be seen in Figure 3.7(a). A trench is dug on both sides of the sample as can also be seen in Figure 3.7(a). Then the sample is tilted and cut from three sides leaving it attached to the bulk from one side. The sample is attached to a needle by welding needle and sample together by depositing platinum. Once the section is attached to the needle, it is separated from the bulk by cutting the remaining side. The needle is taken away to a copper grid and the sample is welded to the copper grid using the platinum. Then the sample is separated from the needle by cutting it off using gallium ions. The samples welded to the grid can be seen in Figures 3.7(c) and 3.7(b). Finally, the sample is thinned to electron transparency using gallium ions which can be seen in Figure 3.7(d).

3.4.6. Homogeneity of AlN doped SiC

The pressed pellets were analysed using microprobe analysis in a (JEOL 840JSM) SEM and in later stages of work using a (JEOL 6400JSM) SEM. The samples were given around 10 nm thick gold coating before SEM analysis to stop the build-up of electric charge on the surface of the samples due to bombardment and absorption of charged particles. A qualitative analysis of the distribution of AlN in SiC matrix was carried out by mapping Al and Si on the surface of a pressed pellet using the EDX function in SEM. However, to quantitatively assess the homogeneity of the distribution of AlN in SiC matrix, a methodology inspired by the work of Zaspalis and Kolenbrander [118] was used.



(a) Trenches around the Sample

(b) Section and the copper grid

(c) Section attached to copper grid

(d) A close-up of section

Figure 3.7.: Images showing various stages of FIB sectioning to make TEM samples

The analysis consists of measuring the Al to Si ratio over increasingly smaller areas of the sample. This reduction in the area is analogous to reducing the number of particles analysed in a given measurement.

A large area analysis will detect the same amount of Al as the average amount for every trial. As the area analysed is reduced, each trial will yield varying amounts of Al that will lead to an increase in standard deviation. However the average Al detected for large number of trials will be the same as the overall sample average. The trend will continue for further reductions in the area analysed. A schematic of this is given

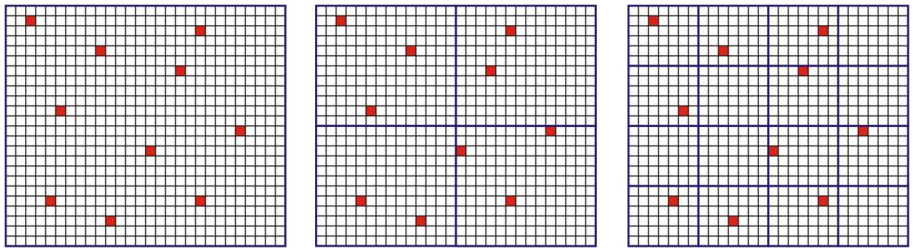


Figure 3.8.: A schematic showing how the reduction in the area affects the standard deviation.

in figure 3.8. It can be seen that as the area analysed is reduced, the variation in the amounts of Al and Si detected increases hence the standard deviation increases however the average amount detected for sufficiently large measurements remains the same as the overall average Si and Al in the sample.

To quantify the expected variation in the standard deviation, a model was developed in which the homogeneity is described by 2D packing of particles of a given size. It is assumed that the particles are circular and are closely packed. This allows the conversion of a measured area in a number of particles using equation 3.9

$$z \sim \varrho A_s \tag{3.9}$$

where z is the number of particles considered, A_s is the area and ϱ is the shape factor which also includes the particle size and packing of these particles. The value of ϱ used was is the ratio of the total area to area occupied by the particles assuming close packing which changes with the change in the particle size. Hence measuring a given area corresponds to determining the fraction of AlN particles when

drawing z particles out of a collection of particles with a fraction of q_A being AlN.

If a sample of n particles is taken out of a mixture of two powders A and B, in which q_A is the fraction of A type particles then the probability P that i particles will be of type A is given by equation 3.10

$$P_i = (1 - q_A)^{z-i}(q_A)^i \cdot \frac{z!}{(z-i)! \cdot i!} \tag{3.10}$$

It can also be shown using the probability distribution that the average composition measured is independent of the number of particles sampled in the measurement and is equal to the composition of the sample:

$$\bar{q_A} = \sum \frac{i}{z} P_i = q_A \tag{3.11}$$

provided that sufficiently large number of measurements are carried out. As the particle size gets smaller the number of measurements required to obtain an accurate result increases.

The standard deviation on the average fraction of particles A is given by equation 3.12

$$\sigma = \sqrt{\sum \left(q_A - \frac{i}{z}\right)^2 \cdot P_i} \tag{3.12}$$

and it does depend on the number of particles included in a single measurement. Substituting P_i yields:

$$\sigma_{1p} = \sqrt{q_A(1 - q_A)} \tag{3.13}$$

and therefore the standard deviation

$$\sigma_z = \frac{\sqrt{q_a(1 - q_a)}}{\sqrt{z}} \tag{3.14}$$

Since z is proportional to area analysed, plotting the standard deviation against area measured allows the determination of a characteristic size for AlN agglomerates.

3.4.7. Polytype determination from XRD [119]

XRD was carried out to check the crystal structure of AlN, as well as the SiC polytypes present in α-SiC powder. It is important because as discussed in the Chapter 2, the different polytypes have slightly different mechanical characteristics and it is known that during sintering these polytypes transform and in doing so influence the microstructure development.

XRD is a technique that is used to get information about the phases present in materials. X-rays are generated when high speed electrons collide with a metallic target. Most of their energy is used up in heating the metallic target hence the target is usually water cooled. Some energy is used up in generation of X-rays. This X-ray beam (incident beam) in pointed towards the sample to be analysed. These X-rays diffract from the planes in the sample. Constructive interference takes place when Bragg's law:

$$n\lambda = 2dsin\theta \tag{3.15}$$

is satisfied, where λ is the wave length of X-rays (for Cu Kα, it is 1.54 $\mathring{A}$), n is the reflection order, and sinθ is the angle between the planes and the X-rays as explained in figure 3.9.

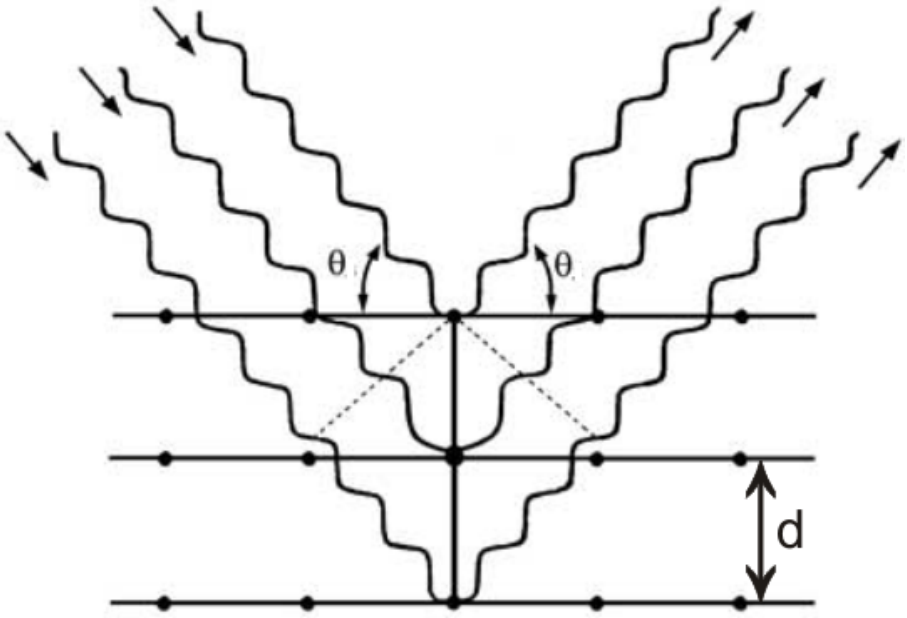


Figure 3.9.: A schematic explaining Bragg's Law.

XRD experiments were carried out with Cu Kα radiation on a Philips diffractometer model number PW 1729. The step size was 0.040° with a counting time of 1 second for the standard scan of SiC and AlN powders. The sintered samples were polished with diamond suspension with the particle size of 1 μm whereas the powdered samples were packed into small disc shaped moulds and their surfaces were flattened with a glass slide. For the polytype determination in SiC more detailed

scans were carried out between 30-45° 2θ in which the scan time was increased to 4 seconds. The Ruska et al. [120] method was used to calculate the polytypes from the XRD data. This method uses XRD peak intensities to work out the fractions of each polytype present in the system. A set of equations describing the height of a set of peaks was developed and finding the best solution to this simultaneous set of equations therefore allows determination of the polytype content. It is clear from table 3.4 that only the 15R, 6H, 4H and 3C polytypes are considered as these are the most common.

Table 3.4.: Table showing equations to calculate various polytypes present in the SiC samples. The equations were developed by Ruska et al. [120]

15R		**6H**		**4H**		**3C**		**Peak**	**d(nm)**
3.2a			+	9.9c			=	A	0.266
11.2a	+	22.12b					=	B	0.263
26.0a			+	38.9c			=	C	0.257
31.1a	+	59.2b	+	25.1c	+	100.0d	=	D	0.251
		20.22b	+	34.1c			=	E	0.235
2.4a	+	6.5b			+	13.1d	=	F	0.217

The intensities of the peaks were determined by fitting Lorentzian peaks to the data:

$$Ł(x) = \frac{A_p}{2\pi} \times \frac{\Gamma}{(x - x_o)^2 + (\Gamma/2)^2} \tag{3.16}$$

where Γ is peak width at half of its height, x_0 is the peak position, x is the position where intensity, L(x) is to be calculated and A_p is the area under the peak given by equation 3.17

$$A_p = L(x_0) \cdot \frac{\pi\Gamma}{2} \tag{3.17}$$

The L(x) value calculated was used in the equations given in table 3.4. to work out the fraction of each polytype present in the system. The error associated with this method is estimated to be around 10% because of the over deteminent system of equations (6 equations, 4 unknowns). All equations are solved simultaneously and errors are reduced in all of them which results in an inaccurate result. There are errors associated with the XRD technique as well including; preferred orientation and detection of higher order peaks.

3.4.8. Etching and grain size measurement

The shapes and sizes of grains in a sintered SiC ceramic determine most of its mechanical properties. Therefore it is essential to measure the grain size.

The first step towards measuring the grain size is to make the grains visible. The grains are not readily observable in a sintered silicon carbide sample. The sample needs to be either thermally or chemically treated in order to see the grains. Any chemical or thermal treatment applied to the sample may react differently with the bulk of the grains and grain boundaries due to the difference in the chemistry of these regions. The chemical or thermal treatment applied to samples in order to make their grains visible is known as etching and the chemical used for this purpose is known as etchant or etching solution.

The chemical etching solution used was a Morakami solution consisting of 40 wt% distilled water, 30 wt% potassium hydroxide (KOH) and 30 wt% potassium ferricyanide $K_3[Fe(CN)_6]$

Sintered samples were fine polished to 1 μm or better using a diamond particle suspension. Then the etching solution was prepared. The ingredients were weighed at the required quantities. The water was poured into the glass beaker, which was placed on a hot plate. Once the water started to boil, KOH was slowly introduced into the water while the solution was stirred with a glass rod. Then potassium ferricyanide was also added into this boiling solution while the stirring with the glass rod continued. Finally, the sample was put into this boiling solution and a glass lid was placed on top of the beaker to stop the evaporating water from leaving the beaker and changing the composition in the beaker. The sample was left in this boiling solution for 90 to 180 seconds. The sample was put under the running water to remove any etching solution from the surface of the sample.

The etched samples were then examined using SEM. A line intercept method was used to measure the grain size. A line is drawn on the image and the number of grains it cuts through are counted. The scale bar on the image is used to determine the total length of the line in microns. The length of this line is divided by the number of grains it cuts through and multiplied with the conversion factor of 1.58 [121] to get the average size of a grain. 4 images at 2 different magnifications were used and in total around 400 grains were analysed for each sample.

In the case of samples with elongated grains or platelets, twenty

large grains were taken and their width and length were measured. The aspect ratio was calculated by dividing average length by the average width of these large grains.

3.5. Macro and micro indentation

Indentation of sample using loads above 1N was carried out with a Zwick/Roell Indentec ZHV Type micro hardness tester with a Vickers tip whereas the macro indentation was carried out using a Zwick/Roell Indentec Type 6030LKV Vickers Hardness testing machine with the load range starting from 10 N. 20 indents were made in each sample at each load with a hold time of 10 seconds at the maximum load. The samples were polished using the method described in section 3.4.8 before hardness testing. A built-in optical microscope was used to measure the size of diagonals of indents. The hardness was calculated by measuring the area of the indent from these diagonal lengths and dividing the applied load with this area.

The so obtained Vickers hardness number was then converted into a projected area hardness by dividing by 0.9272 [63] which is the ratio between contact area and projected area of a Vicker's indenter and multiplying by gravitational constant, g (9.81 m S^{-2}).

3.6. Nano-indentation

Nano-indentation experiments were carried out using nanotest from Micro Materials Ltd. and the results were analysed using NanoTest Materials Testing Platform as well as using an in house software based on the method of Oliver and Pharr [69]. A minimum of 20 indents was made in each sample at each load. The load range for nano-indentation experiments was from 100 mN to 400 mN. A schematic is given in figure 3.10

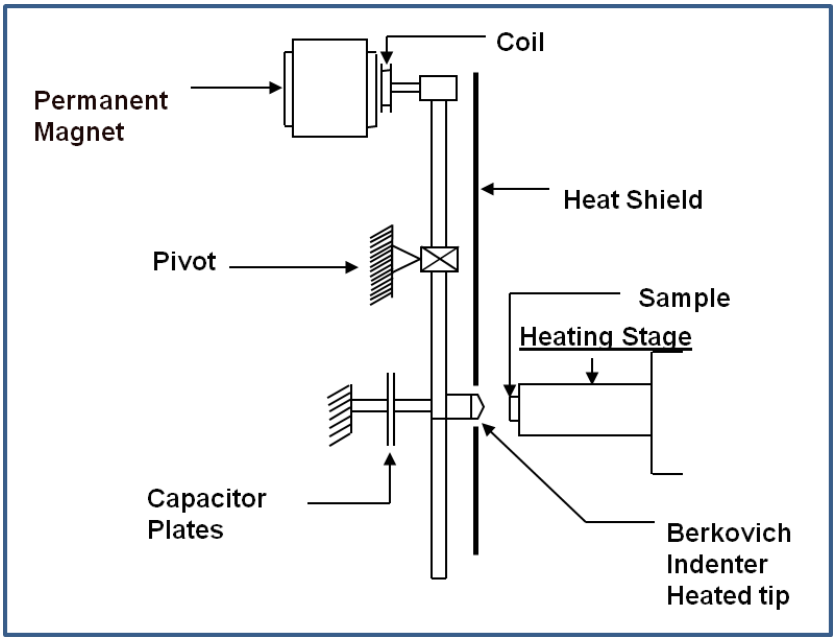


Figure 3.10.: Schematic of nanoindenter showing various components.

Nano-indentation is simply pushing the indenter tip into the surface of a sample and making a small indent (around a micrometer in size). The size of the indents is too small to be measured accurately using an optical microscope so the size is derived from data for the depth and

load recorded by the nano-indenter platform. The penetration depth is measured which can then be converted into projected area using the geometry of the indenter tip.

3.6.1. Extraction of hardness and Young's modulus results from nano-indentation experiments

The most widely used method of extracting hardness from nano-indentation experiments is the one developed by Oliver and Pharr [69].

This method recognises that the total displacement, h_t, during the indentation consists of two parts.

1: the elastic deflection of the surface, h_e

2: the distance over which material and indenter are in contact, h_c known as contact height.

These various heights and load are illustrated in the schematic in figure 3.11.

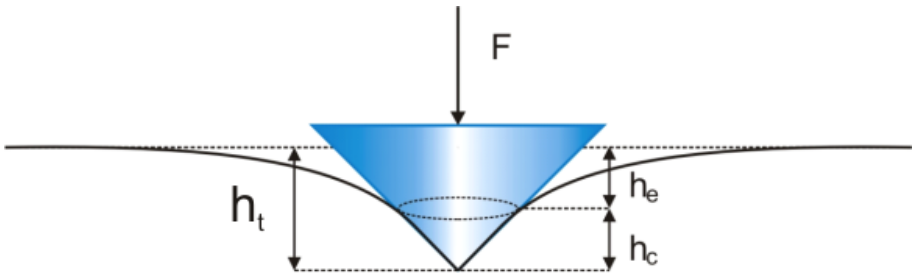


Figure 3.11.: A schematic of indenter tip showing h_c, h_t and h_e.

Since height is a function of the area of the indent, a value for the contact height, h_c must be determined. Oliver and Pharr [69] showed

using Sneddon's [122] work that there is a relationship between h_c and total height, h_t which is given in equation 3.18.

$$h_c = h_t - \epsilon \frac{F}{S} \tag{3.18}$$

where F is load of indentation, S is the slope of the unloading curve as can be seen in figure 3.12 and ϵ is a constant which is typically taken as 0.75.

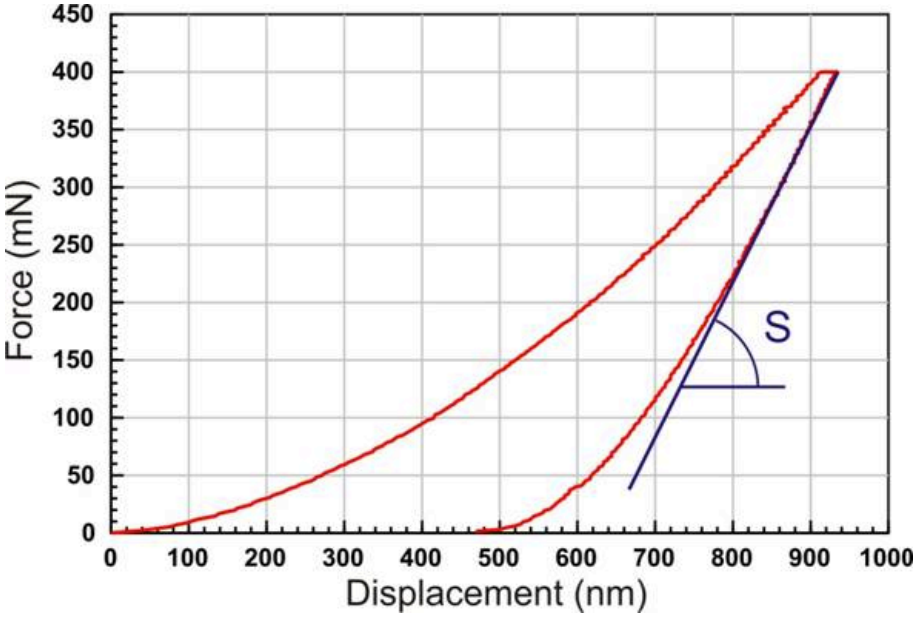


Figure 3.12.: A schematic of the load vs displacement curve.

The contact area, A_c is found from the geometry of the indenter tip and is a function of h_c. However, a calibration is required in order to take into account the 'bluntness' of the indenter tip which is described in section 3.6.2.

Once the contact height is known then the hardness can easily be calculated from equation 3.19.

$$H = \frac{F}{A_c} \tag{3.19}$$

Oliver and Pharr [69] also showed that the slope of the unloading curve, S is directly related to the reduced modulus, E_r and the contact area, A_C through equation 3.20.

$$E_r = \frac{S}{2}\sqrt{\frac{\pi}{A_c}} \tag{3.20}$$

This reduced modulus, E_r is a combined Young's modulus of both the indenter and the sample. The relationship between reduced modulus, Young's moduli of both the sample and the indenter and their Poisson's ratios is given by equation 3.21.

$$\frac{1}{E_r} = \frac{1-\nu_s^2}{E_s} + \frac{1-\nu_i^2}{E_i} \tag{3.21}$$

where E_s and ν_s are the Young's modulus and Poissons ratio of the sample and E_i and ν_i are the Young's modulus and Poisson ratio of indenter respectively. So if the E_i, ν_i and ν_s are known than E_s can be calculated.

3.6.2. Area and load calibrations

The area, A_c with respect to h_c can be found from the calibration method. The indenter tip is calibrated by indenting a fused silica sample of known Young's modulus. The contact area is then the only unknown in equation 3.20, thereby allowing the contact area to be

determined as a function of contact height. The shape of the tip used in the nano-indenter is a three sided pyramid with an inclined angle of 142.3° and a half angle of 65.3°. A few important properties of this tip include the self similarity, i.e. the deformation pattern can in principle to be expected to scale with load, as well as having the same projected area to depth ratio as the Vickers indenter tip. Its three sided geometry makes it possible to grind it to a sharp point.

Projected area, A is a function of contact height, h_c

$$A = f(h_c) \tag{3.22}$$

From the geometry of the Berkovich indenter, equation 3.23 links the height to projected area for an ideal (sharp) tip.

$$A = 24.56h_c^2 \tag{3.23}$$

If the tip is worn out and not sharp then this expression will not be true. An artificially high hardness will be given as the real h_c will be lower than the one which corresponds to the area calculated from expression 3.23.

Displacement is measured accurately by two capacitor plates. The load leads to change in the distance between both plates and as a result in the change in capacitance. This change in capacitance is measured as a load. The effect of distance between two plates on the capacitance is given in equation 3.24

$$C_p = \varepsilon_r \varepsilon_0 \frac{A_l}{s} \tag{3.24}$$

where C_p is capacitance, A_l is the overlap area of two plates, s is the separation between both plates, ε_r is the relative static permittivity which depends on the media between both plates (in case of vacuum, it is 1) and ε_0 is the electrical permittivity of vacuum which is 8.85 x 10^{-12} F m^{-1}.

Another correction that needs to be made in order to get accurate values of displacement is the thermal drift correction. This is important since capacitance is a function of temperature and the change in capacitance is measured as a change in displacement. Although the indentation is carried out in an enclosed environment with a heater to control the temperature, this measurement is necessary for accurate results. The importance of this correction is even greater for high temperature indentation. A dual heating set up is used where the indenter tip is also heated to avoid the sample cooling locally.

Even with the dual heating set up, thermal drift is corrected. This correction is made before and/or after every indent by holding the tip pushing against the sample surface with a percentage of the maximum load. This was usually 20% of the maximum load other than in some specific experiments. The indenter tip was held at that particular load for 1 minute and any changes in the displacement detected measured. This measured displacement is due to the change in temperature. This correction is than applied to that particular indent's load output.

3.6.3. Sources of error in nanoindentation experiments

Nanoindendation experiments are prone to various experimental errors which needs to be carefully considered when presenting or analysing the results. They are both to do with the sample as well as the indenter. Sample surface finish is very crucial in determining the accurate value of hardness as the total depth of an indent is in nano scale, any surface roughness can alter the results very dramatically.

The shape of the tip can be very critical. Although an area calibration is carried out in order to take into account the tip bluntness, a very rounded tip leads to an apparent reverse indentation size effect where hardness appears to increase with increasing load in the nano regime as was the case in some of the results discussed in chapter 5.

Since the load is applied through the change in the current in the nanoindenter and displacement is measured by the capacitance between two plates, the temperature in the indenter can have a large impact on the accuracy of the data especially for above room temperature indentation. A dual heating setup (heated sample stage as well as the heater inside the diamond tip so that thermal equilibrium between indenter and sample can be achieved) was used for greater accuracy.

Thermal drift was measured showed that it increases with increasing experimental time. To limit the effect of thermal drift even further, experiments were kept short where possible.

3.6.4. Elevated temperature nano-indentation experiments

Nano-indentation experiments can be carried out at elevated temperature. For this purpose, a dual heating set-up is used with one heater attached to the sample stage and the other to heat the indenter tip. This is to avoid sample cooling when in contact with the indenter tip. This also is helpful in reducing the thermal drift in the measured depth signal.

The high temperature strain rate sensitivity experiments were carried out using the following sequence: the thermal stability of the capacitative displacement sensor was measured for 1 minute before the experiment, followed by a 1 minute thermalisation period. Then the indenter load was applied at a fixed rate to the predetermined maximum load. It was held at the maximum load for 1 minute. The indenter was unloaded at the same rate as during loading. The second stability measurement was carried out at 10% of the maximum load for 1 minute. The details of loads, loading rates and temperature are given in chapter 5.

4. Sintering and Microstructure

4.1. Introduction

The overall aim of the work in this chapter is to clarify microstructure formation in AlN-doped SiC and to design processing methods for reliable production of such material.

An important aspect of any ceramic processing is the homogeneous distribution of sintering additives. Clustering of the additives leads to inhomogeneity and results in different properties in different parts of the sample. Therefore a first set of experiments was carried out to confirm that a homogeneous distribution of the AlN powder in the AlN/SiC powder mix could be achieved. To this end a methodology was developed which allowed analysis of the distribution of AlN in the samples. However, the best that can be achieved by mixing is to distribute the AlN at powder level. For activation of sintering, even better distribution of sintering additives is desirable, and hence a second stage of the experiment was to investigate how AlN redistributes

during sintering.

The second question arising from the literature review is the role of AlN in sintering and microstructure development of SiC. In LPS SiC, AlN has replaced alumina (Al_2O_3) because it reduces the weight loss during sintering [38]. However, the role of adding AlN in small quantities as a sintering additive in SiC has not been extensively studied. It is not clear whether addition of AlN alone also leads to LPS or rather aids Solid State Sintering (SSS) by providing a source of Al, which is an alternative to boron in SSS. Since AlN will only lead to a liquid phase if it can react with the silica on the surface of the SiC, it was decided to produce compositions in which AlN was added either with or without carbon as a further additive. In samples with carbon, the surface silica should be reduced [14] during heating and hence the expectation is that if AlN were only to aid LPS then the samples with carbon would be expected to show poor densification. To allow comparison with a reference material, which shows LPS, one composition which contained AlN and yttria Y_2O_3 was also produced.

Apart from the additive system, the sintering schedule is another way to control the microstructure. To investigate the effect on microstructures in AlN-doped SiC, a range of sintering schedules were used with different heating rates and dwells. Faster processing was carried out using a SPS, whereas slower processing was carried out in a HP.

This chapter is therefore divided into three parts: first the effect of mixing on the homogeneity and the measurement of the redistribution

of Al(N) will be described followed by the effect of different additive combinations and then finally the influence of the sintering schedule.

4.2. Homogeneity of AlN in AlN-SiC powder mixture and sintered samples

The distribution of AlN powder in the AlN-SiC powder mixture was studied by comparing how the standard deviation on 10 measurements of the Al content via EDS varied with the size of the area measured. As shown in figure 4.1 when large areas are analysed, the Al concentration in all areas is similar and the standard deviation for 10 measurements is approximately 0.2 wt%. When the area analysed is 10 μm^2 or smaller the standard deviation increases indicating that some areas contain more Al than others.

The results were compared with a model where the particles of different sizes were defined and their standard deviation with the reduction in the sample size was calculated.

A range of particle sizes are plotted in graph given in figure 4.1. q_A used in the model is the same as the average amounts of Al detected in SEM. At large area analyses, the variation in the standard deviation is lower then the errors associated with this experiment. As the area analysed starts to get closer to the particle size, the standard deviation due to counting effects starts to dominate. By looking at the lines for different particle sizes from the model, the size of agglomerates can be

estimated. If this is comparable to the particle size that means that the particles are randomly mixed. If the size of agglomerates is bigger than the particle size then it means that AlN particles are clustered and not homogeneously mixed in the sample.

It leads to conclusion that the AlN is distributed in agglomerates of a size similar to the AlN particle size (1 μm).

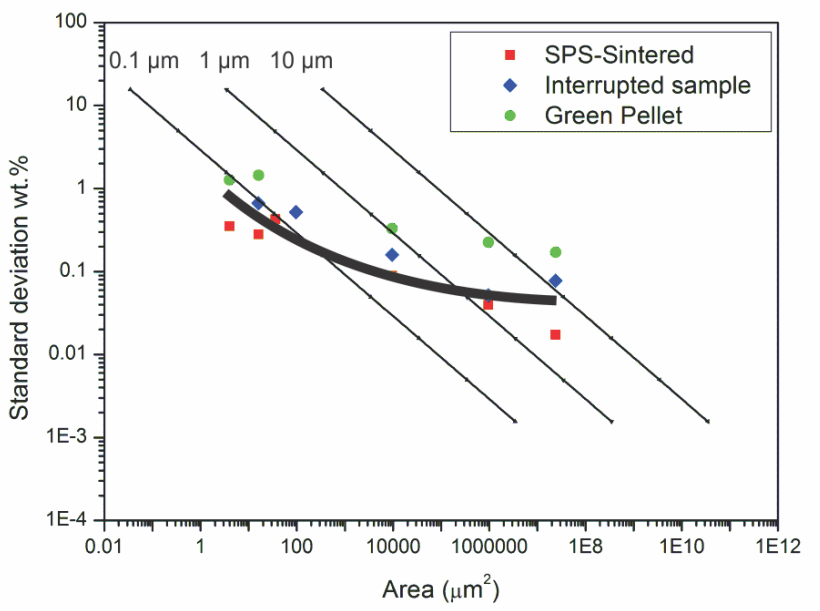


Figure 4.1.: Graph showing level of homogeneity achieved in samples. SPS-sintered sample was SPS for 5 minutes at 2100 °C. Interrupted sample was heated in HP to 1700 °C. The green pellet was uniaxially pressed pellet. All samples had the composition of SiC + 3 wt% C + 3.75 wt% AlN. The black lines are theoretical predictions for the standard deviations as a function of particle size.

Figure 4.2 illustrates how the standard deviation for an area analysed amounting to 16 μm^2 varies during heating and sintering. While AlN is homogeneously distributed in the cold pressed pellets, the decrease

in the standard deviation for a fixed area shows that the homogeneity level increases slightly for the partially sintered sample at 1700 °C whereas the sintered sample and a partially sintered sample at 1850 °C have a much better and similar level of homogeneity of AlN: the AlN is now distributed to a sub−micron level.

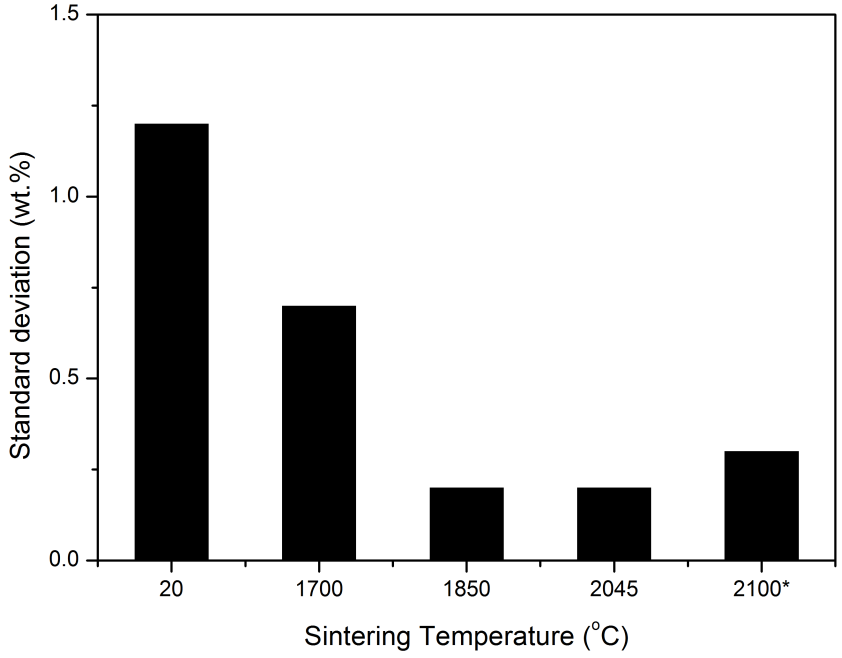


Figure 4.2.: Graph showing level of homogeneity achieved during various stages of sintering from cold pressed pellet to a fully sintered sample. This graph is simply a section taken from the graph given in figure 4.1 at the area of 16 μm^2. All samples contained 3.75 wt% AlN and 3 wt% C. The starred sample was SPSed at 2100 °C whereas all other samples were hot pressed.

The standard deviation observed in the latter samples agrees with the standard deviation observed for larger areas in the green pellets and therefore the homogeneity is better then can be ascertained with the technique used. It is therefore possible that the level of homogeneity

continues to improve as the samples are heated and during the time spent at the sintering temperature.

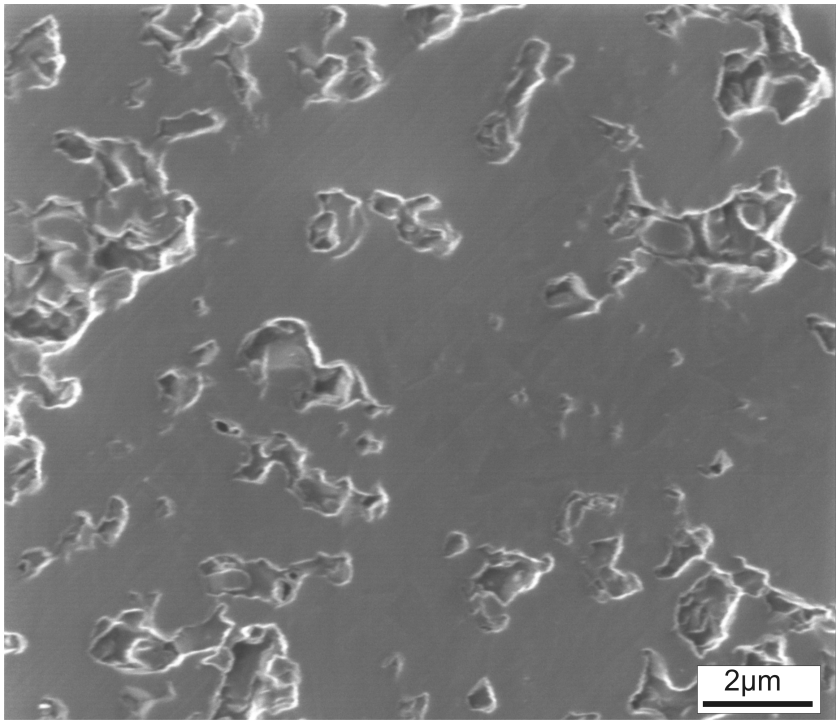
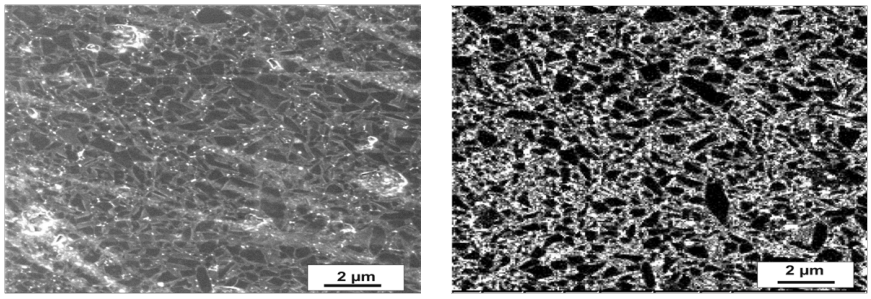


Figure 4.3.: Electron image taken in FIB from a partially sintered sample at 1850 °C. The densification has clearly progressed significantly.

A micrograph of a partially sintered sample given in figure 4.3 shows that densification coincides with the much improved redistribution of the AlN. This is confirmed by relative density of 75% whereas a sample containing no AlN only reached 66% after a complete sintering schedule (HP-dwells).

To investigate the AlN distribution even further, SIMS was used to produce maps of the Al distribution in the samples. The maps confirmed that the AlN has redistributed to a much finer level than before



(a) FIB image (b) SIMS Al map

Figure 4.4.: FIB image and SIMS map from the same area of α-SiC with 3 wt% C and 3.75 wt% AlN SPSed at 2100 °C. (a) Electron image (b) SIMS map of aluminium. White dots are where the Al signal was detected in the SIMS map.

sintering with many tiny Al-rich particles present in the microstructure (figure 4.4).

Comparing the electron images with the Al-maps suggests that the Al signal coincides with the grain boundaries and the more intense Al signal coincides with the triple junctions in the microstructure.

SIMS results from samples containing various amounts of AlN show that the Al distribution achieved was very similar as can be seen from figure 4.5. The only difference between these samples is that the samples with higher amounts of AlN show the location of initial AlN particles where the black dots are present. These dots are not visible in the sample with small amount of AlN as they are perhaps fully distributed.

An even closer look at the sintered samples using TEM (see figure 4.6) confirms the presence of Al on the grain boundaries and triple junctions. The EDX analysis performed on the samples suggests that the triple junctions are rich in Al and the concentration of Al is comparatively low inside the SiC grains as can be seen from figure 4.7.

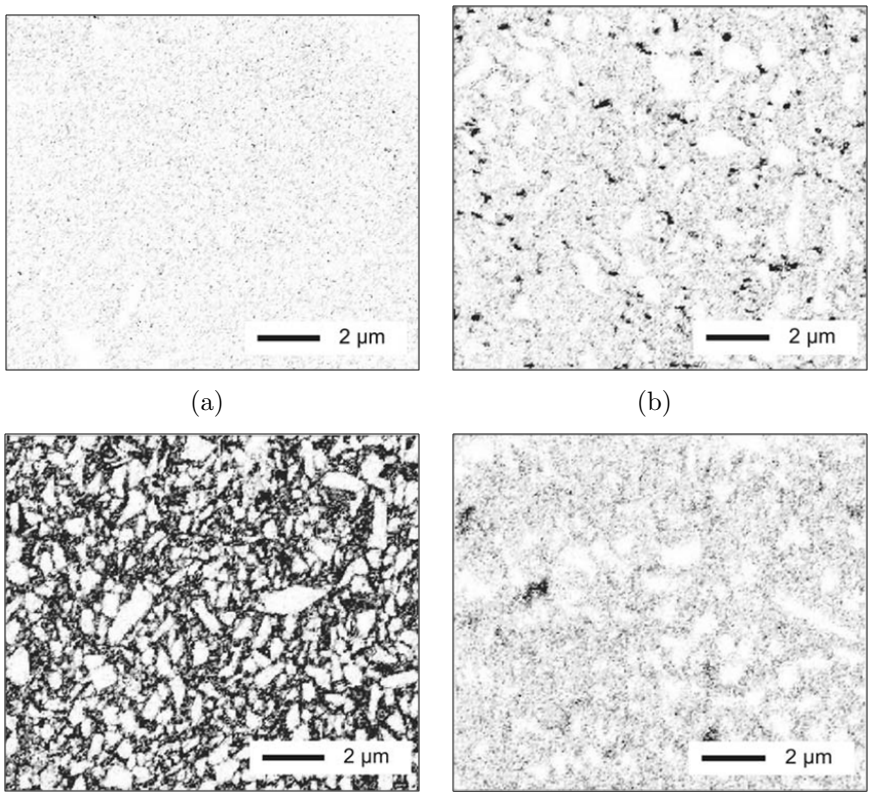


Figure 4.5.: SIMS maps of SiC samples with various amounts of AlN and 3 wt% C. (a), (b) and (c) are SPS sintered for 5 minutes at 2100 °C containing 0.75, 2.5 and 3.75 wt.% AlN whereas (d) is sintered using HP−Dwells sintering schedule which contains 3.75 wt.% AlN. Al is more homogeneously distributed in (d). Black dots show the position of initial AlN particles. (Image taken from [123])

It can be seen from this study that the AlN is fully homogeneous at temperatures as low as 1850 °C. This raises the question of the mechanisms of this re-distribution. Bulk diffusion is too slow a process [43] at such low temperature for such a quick distribution to take place because of the low diffusion coefficients in SiC and AlN. Also the Al-maps distribution profile does not support the bulk diffusion theory which

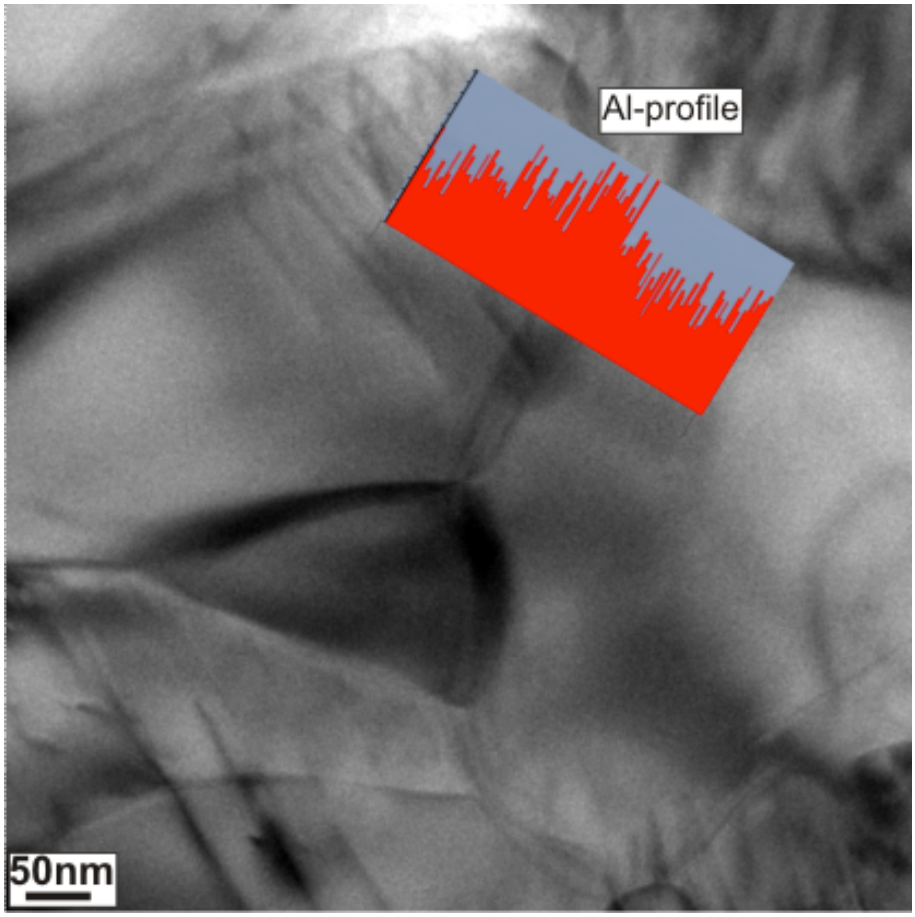
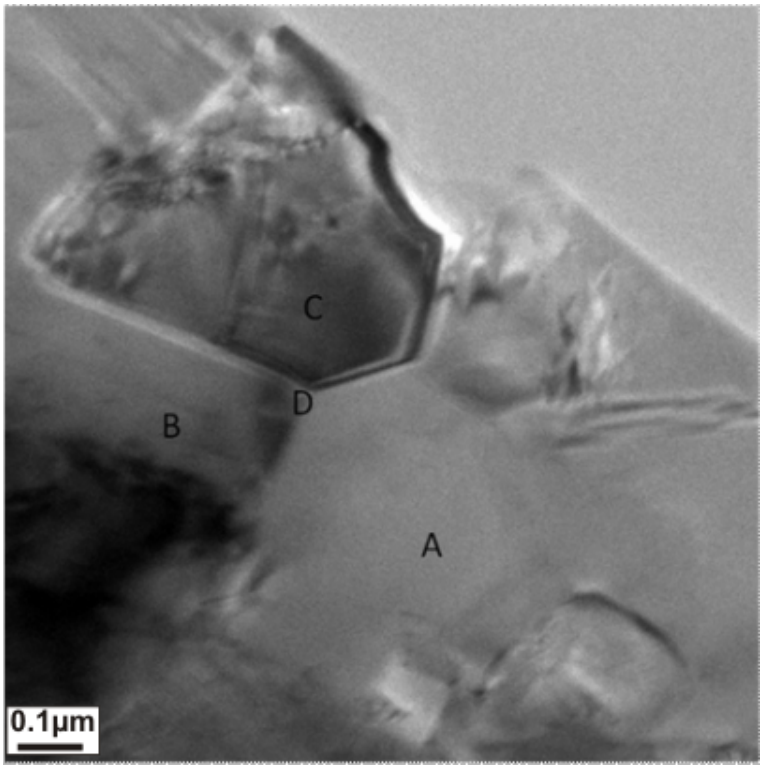


Figure 4.6.: TEM micrograph showing an Al profile across a grain boundary in an α-SiC sample containing 3 wt% C and 3.75 wt% AlN SPSed at 2100 °C for 5 minutes.

would show the AlN reducing out spherically from the AlN powder particles. This has not been the case and the Al has been found concentrated quite uniformly on the grain boundaries. A possible mechanism could be diffusion along the grain boundaries. Evaporation of AlN from AlN particles and re-condensation between the SiC grains can be another method of redistribution of AlN. Thermodynamic calculations suggest that it is possible for the AlN to evaporate at the



Location	carbon	oxygen	aluminium	silicon
A	78.3	5.43	Trace	16.25
B	78.3	4	0.08	17.7
C	74	9.6	0.16	16.2
D	76.6	6.4	0.86	16.1

Figure 4.7.: TEM image of an SiC sample containing 3 wt% C and 3.75 wt% AlN SPSed at 2100 °C for 5 minutes and corresponding EDX data from the locations marked in the image. All amounts are in wt%.

temperatures and pressures that it is exposed to during sintering as can be seen from figure 4.8 as AlN solid thermodynamically becomes unstable at the temperatures and presures applied.

Hence, in the green body the AlN is distributed at powder level, but during heating to the sintering temperature the Al(N) redistributes

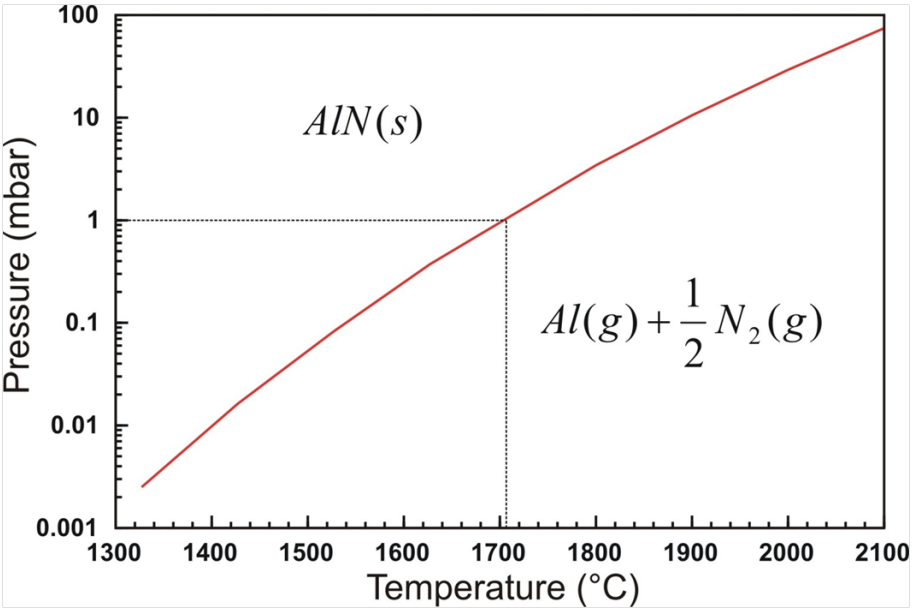


Figure 4.8.: Pressure vs temperature graph showing the stable phases of AlN solid, Al and N_2 gasses. 1 mbar is a typical pressure applied during vacuum sintering and hence above 1700 °C AlN should decompose and evaporate.

to a much finer level and collects on grain boundaries and in triple junctions. The redistribution coincides with the onset of active densification whereas densification is much more limited when no AlN is present. It is tentatively proposed that the rapid redistribution might involve transport via the gas phase.

4.3. Effects of composition on sintering and microstructure of SiC

After establishing the homogeneity of AlN in the samples, the effects of various amounts of AlN on sintering and microstructure were studied.

In most samples, 3 wt% carbon was also added, but in one sample no carbon was added, whereas in one other sample carbon has been replaced by yttria to investigate their effects on the sintering. The main aim was to see if AlN causes LPS or SSS. All the compositions and sintering schedules are given in tables 3.2 and 3.3.

4.3.1. Effects of additive systems on densification and microstructure of SiC

It has been mentioned earlier in Chapter 2 that the use of AlN as a sintering additive in SiC was as a replacement for alumina in LPS or as a replacement to Al in SSS. However, when adding small amounts of AlN, it is not clear whether a liquid phase forms or if sintering is by solid state diffusion alone.

Carbon reacts with silica present on the surface of the sample at around 1398 °C [14] giving rise to CO gas so there should be a reduction in the vacuum present during heating at this temperature in the samples containing carbon. Vacuum traces recorded during sintering show three distinct regions in figure 4.9, the first region (a) is where the vacuum is lost because of further pyrolysis of the resin through which carbon was added. This increase in pressure was not seen in the sample with no carbon. The second region (b) is where the reaction between silica and carbon is known to occur. An increase in the gas pressure in this region indicates that the reaction between carbon and silica is occuring as expected. This is clear in the sample containing

both C and AlN. The sample with no carbon did not show any change in vacuum in region (b) confirming the lack of reaction in this temperature range. The third region (c) is where the vacuum improves during the hold time whereas the loss of vacuum is due to the expansion of gases as the temperature increases.

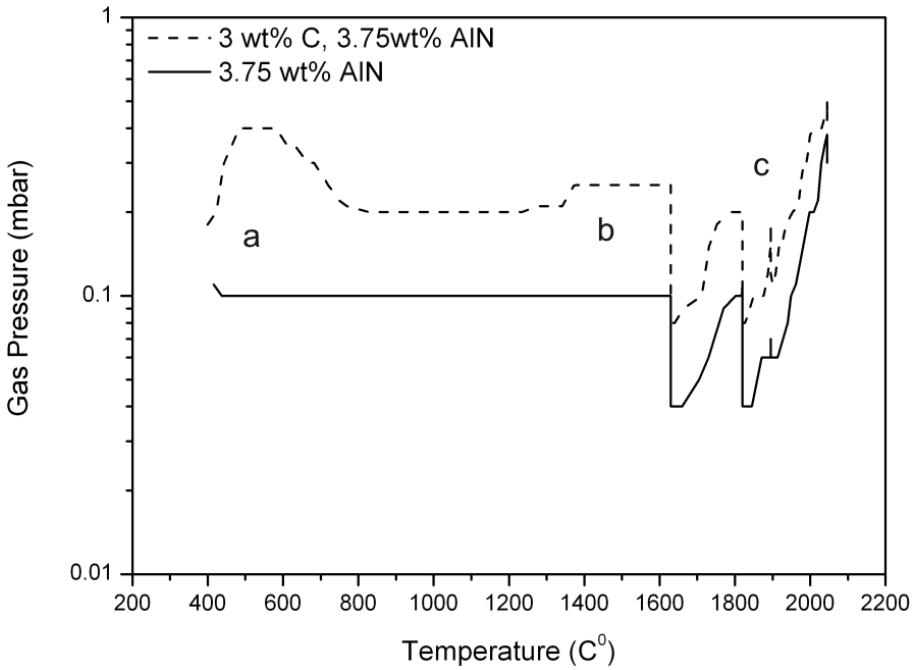


Figure 4.9.: The graph showing the changes in the vacuum during hot pressing with dwells. Losses in the vacuum at various temperatures are evidence of chemical reactions evolving or using gas at those temperatures.

The sample containing carbon and AlN achieved a density of 98% of the theoretical density suggesting that AlN can activate SSS of SiC. The SiC sample that only contained AlN also achieved a density of 97% of the theoretical density. However, the SiC sample that only contained C did not densify. Its final density was 66 % of theoretical density

confirming the results of Maitre et al. [15] and Clegg [14]. Figure 4.10 show the densification curves derived from the ram movements for the three samples, which confirms that carbon is not needed for densification to occur.

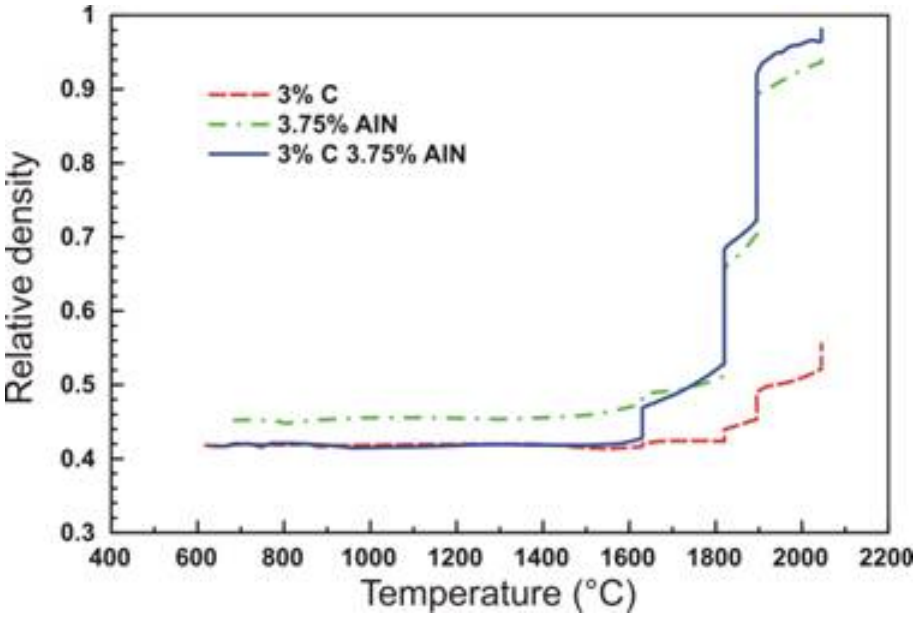


Figure 4.10.: Densificaiton curves of SiC samples containing only C, only AlN and C + AlN HPed with intermediate dwells. (see table 3.3 for details about sintering schedule)

The micrographs of etched samples taken by SEM support the lack of presence of liquid phase from the shapes of grains as can be seen in figure 4.11.

TEM work showed that the grain boundaries are clean as can be seen from figures 4.12 and 4.13.

A SPS sample of the same composition was analysed using TEM (figure 4.14 and high resolution TEM (HRTEM) to check for presence of the liquid phase on the grain boundaries. Figure 4.15 shows that the

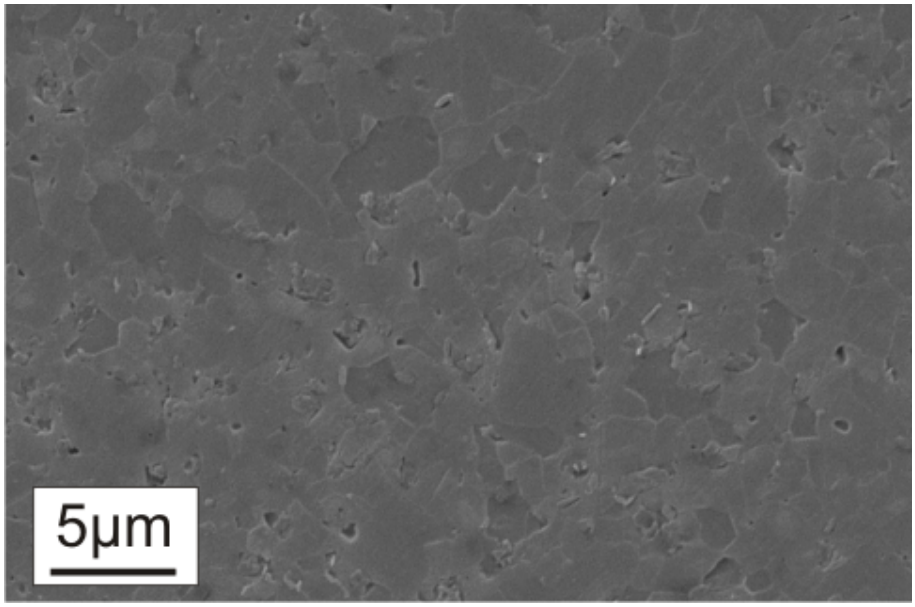


Figure 4.11.: The SEM micrograph of α-SiC sample containing 3 wt% C and 3.75 wt% AlN sintered using HP-dwells schedule.

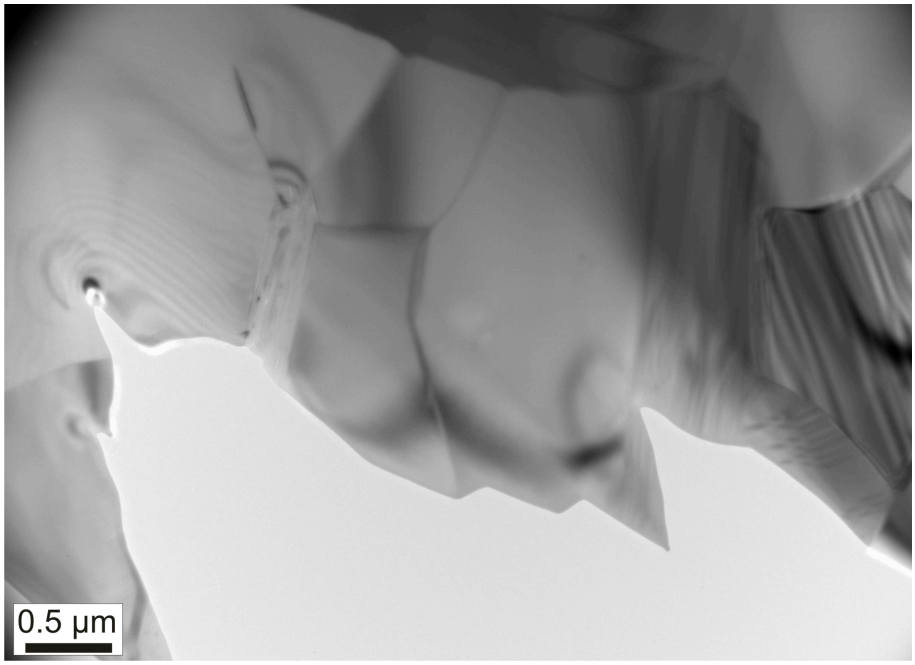


Figure 4.12.: TEM image of α-SiC sample containing 3 wt% C and 3.75 wt% AlN sintered using HP-dwells schedule.

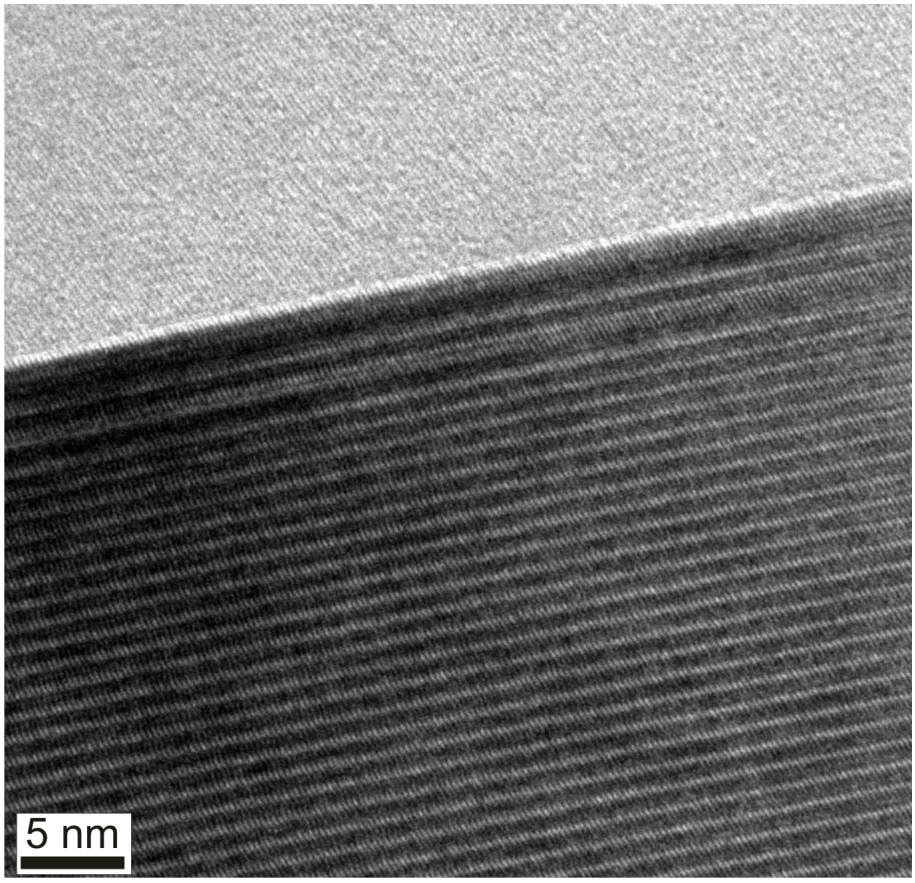
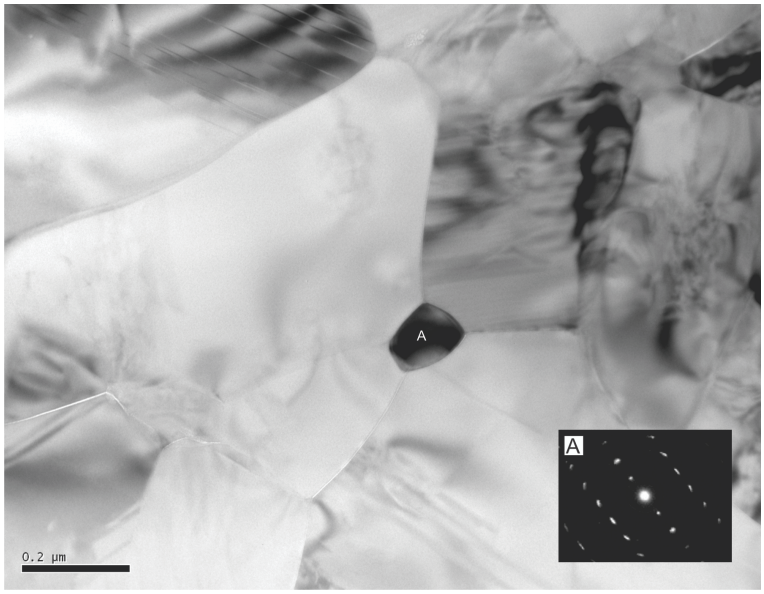


Figure 4.13.: HRTEM of a grain boundary in α-SiC sample containing 3 wt% C and 3.75 wt% AlN sample sintered using HP-dwells schedule. There is no evidence of presence of glassy phase.

grain boundaries are clean and there is no evidence of liquid present.

An interesting feature in figure 4.14 is the particle in the triple junction especially if this image is looked at in conjunction with SIMS results in figures 4.5 and 4.4: the Al rich particles near the triple junction are therefore crystalline and not a glassy phase. The EDX results confirmed the presence of Al and N as well as oxygen. Diffraction pattern taken from this location showed that it is AlN. As has been shown



Location	carbon	oxygen	aluminium	Silicon	Nitrogen
A	31.4	10.4	32.7	15.2	10.6

Figure 4.14.: TEM image of an SiC sample containing 3 wt% C and 3.75 wt% AlN SPSed at 2100 °C for 5 minutes. Selected area electron diffraction pattern and corresponding EDX data from the locations marked in the image. All amounts are in wt.%.

in figure 4.7, the triple junctions were rich in aluminium.

Microstructural observations in the TEM (4.15) suggest there was no liquid phase present in the SPS sample containing carbon and AlN.

The SiC sample containing only AlN also achieved density close to the theoretical. Surprisingly, there was no evidence of the formation of liquid phase from the micrographs of the etched sample as can be seen from shapes of grains in figure 4.16. However, the presence of some liquid on the grain boundaries cannot be ruled out as AlN particles are known to oxidise during sintering and even at room temperature

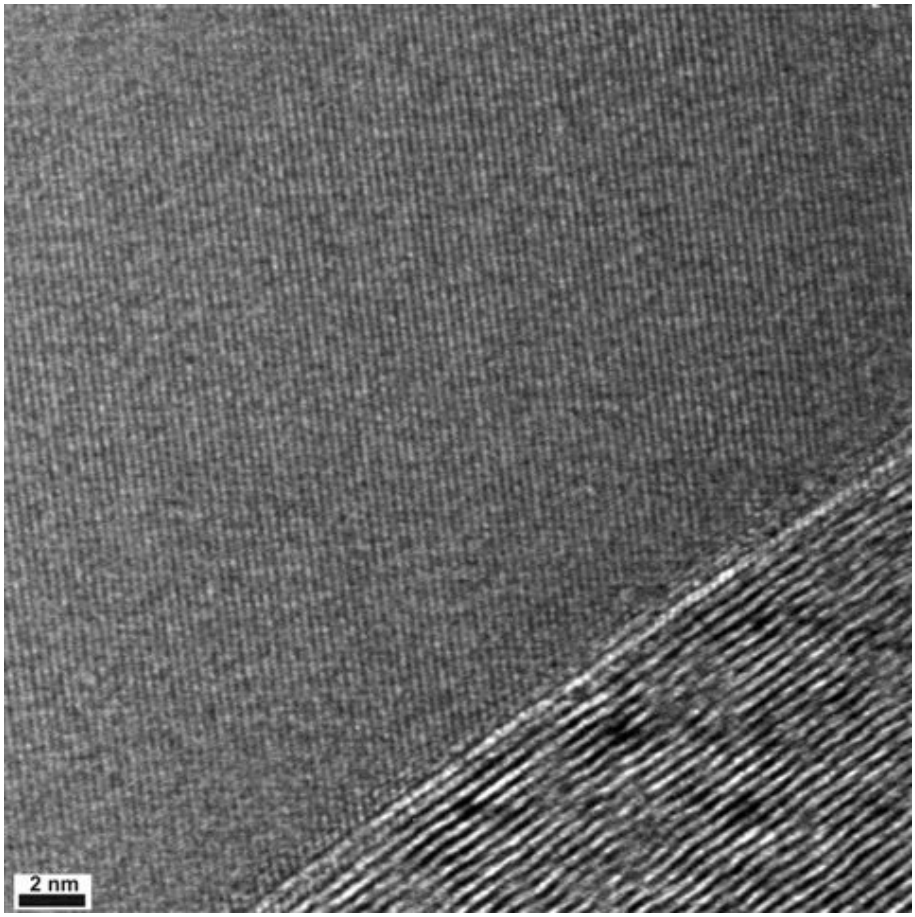


Figure 4.15.: HRTEM image of SPS sintered sample containing carbon and 3.75 wt% AlN. The grain boundaries are clean and there is no evidence of liquid phase.

[124, 125].

Moreover, there are gaps on the grain boundaries so the glassy phase might have been here but removed during etching. TEM images in figures 4.17 and 4.18 do not show the presence of large amounts of liquid phase in the microstructure. However, presence of a thin liquid film on the grain boundaries cannot be ruled out.

The absence of carbon had one marked effect: the grains are much

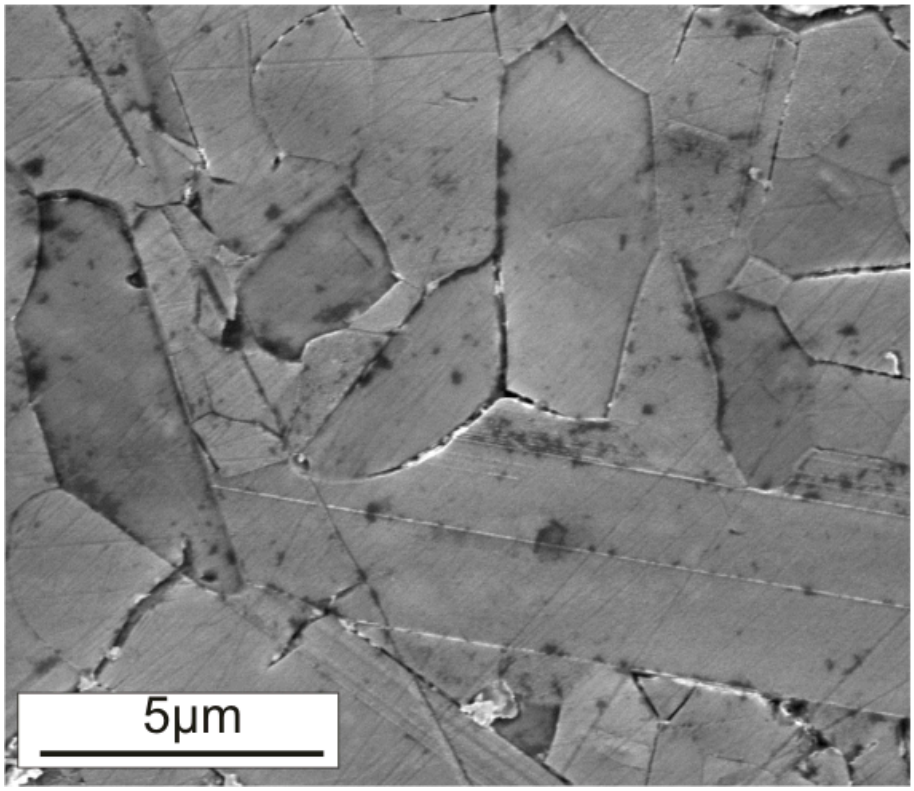


Figure 4.16.: SEM micrograph of sample SiC sample containing only 3.75 wt% AlN sintered using HP-Dwells schedule.

larger (6 μm) and become elongated with an aspect ratio of 2.3. This supports the argument of Maitre et al.[15] and Clegg [14] that carbon restricts the grain growth in SiC sintering hence the absence of carbon should lead to a coarse microstructure.

The yttria-AlN doped sample reveals the presence of the liquid phase in the microstructure as can be seen in figure 4.19.

This study suggests that the confusion in the literature is justified. AlN can act to induce both liquid phase sintering as well as solid state sintering in densifying SiC depending on the other additives used. The evidence suggests that without addition of other oxides, AlN activates

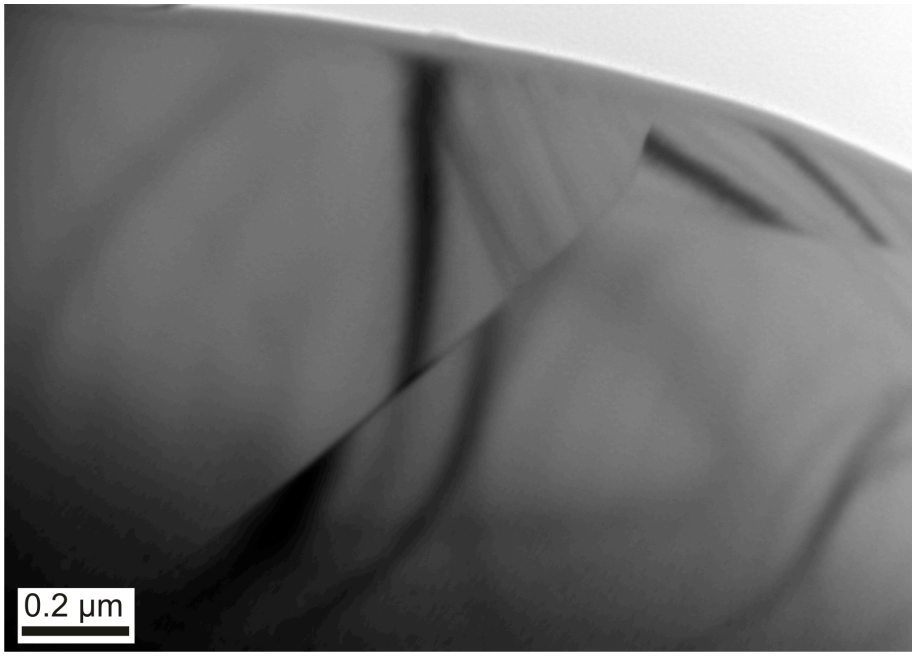


Figure 4.17.: TEM image of SiC + 3.75 wt% AlN sample HPed with dwells. The grain boundary does not show the presence of the liquid phase.

solid state sintering.

4.3.2. Effect of level of AlN additions

The effects of the amount of AlN added on the microstructure of SiC were studied. The amounts of AlN ranged from 0.75 wt% to 3.7 5wt%. All samples were sintered using fast SPS method at 2100 °C. The densities as well as the grain shapes of all samples containing AlN were similar as can be seen from the graph in figure 4.20.

However, grain size measurements, (figures 4.21 and 4.22) show that increasing the amount of AlN leads to a small reduction in the grain size. As discussed above AlN is found mainly on the grain boundaries

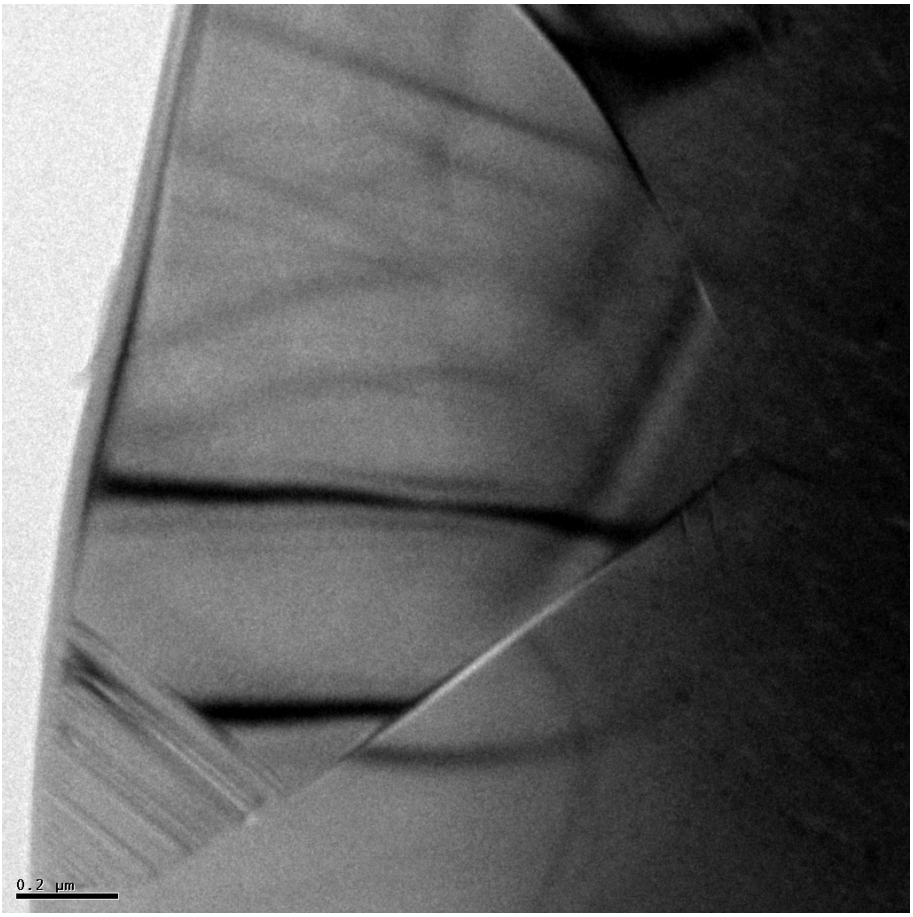


Figure 4.18.: TEM image of SiC + 3.75 wt% AlN sample HPed with dwells. The grain boundary does not show the presence of the liquid phase.

and the data suggest that AlN discourages grain growth. Also the sintering schedule used in this particular instance was short leaving only limited time for grain growth.

The polytype content in samples with different amounts of AlN was also studied. A plot of 6H polytype content against the amount of AlN is presented in figure 4.23. An increase in the amount of AlN leads to a decrease in the polytype transformation from 6H in the



Figure 4.19.: TEM micrograph of 3 wt% yttria doped SiC with 3.75 wt% AlN SPS sintered at 1900 ° C showing the presence of liquid phase.

starting powder to 4H. The stable polytype at this temperature for the AlN content used should be 4H according to the work of Zangvil and Ruh [7]. It is in agreement with the work of Pabit et al.[26] who also found that increasing the amount of AlN lead to a reduction in the polytype transformation from 6H to 4H.

A possible explanation is that the polytype transformation is linked to the formation of SiC-AlN solid solution which is perhaps linked to

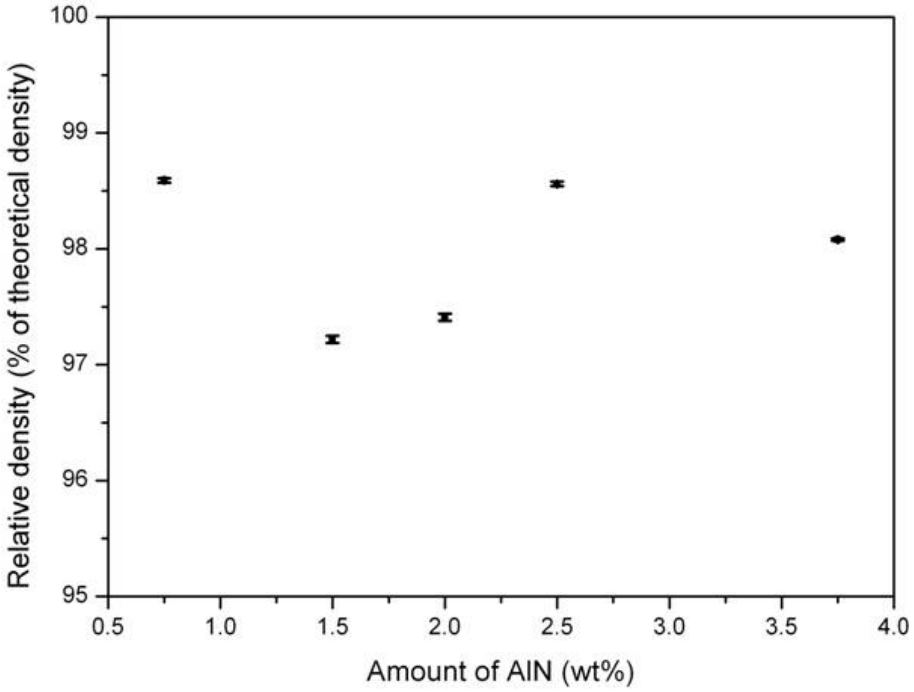
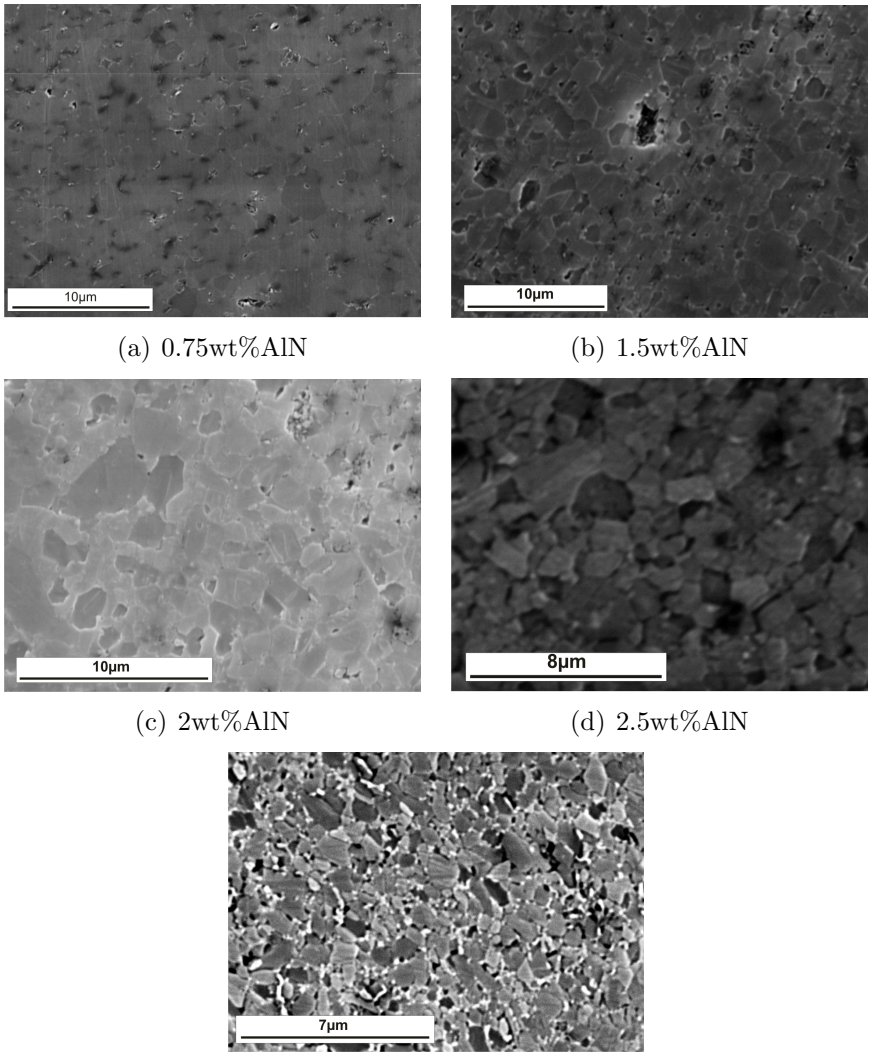


Figure 4.20.: The effects of amount of AlN on the relative densities of SPSed SiC samples. AlN does not have an effect on the relative density.

the grain growth. Although AlN promotes the 6H to 4H polytype transformation, it also suppresses the grain growth. These both are competing processes but perhaps an increase in the grain growth is necessary for the polytype transformation.

Moreover, the formation of an AlN-SiC solid solution is a slow process hence the lack of polytype transformation in fast sintering processes such as SPS. Increasing the time spent at sintering allows bulk diffusion to take place and could perhaps enhance the transformation of 6H SiC into 4H.



(a) 0.75wt%AlN (b) 1.5wt%AlN

(c) 2wt%AlN (d) 2.5wt%AlN

(e) 3.75wt%AlN

Figure 4.21.: Micrographs of α-SiC samples with 3 wt% carbon and various amounts of AlN. All samples were sintered using SPS at 2100 °C for 5 minutes. Image (d) taken from [123]

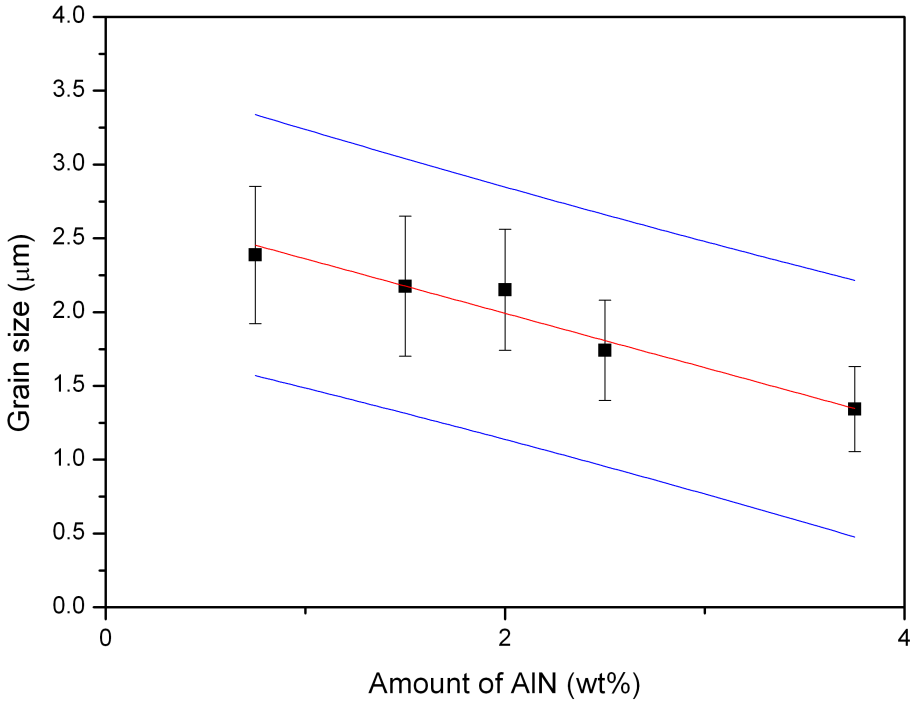


Figure 4.22.: Graph shows effects of the amount of AlN on grain size. The trend lines above and below the values are plotted at 95% predictability.

4.4. Effects of time on sintering

The sintering schedules were set up with a view to see the effects of sintering conditions on the densification and the microstructure of the samples. The two methods used in sintering were SPS and HP. SPS is a fast processing (heating rates of upto 600 °C per minute) and densification method compared to hot pressing (heating rates of 20−30 °C per minute, which is relatively slow. The various sintering schedules tried are given in the table 3.3.

The densification curves given in figure 4.24 suggest that the den-

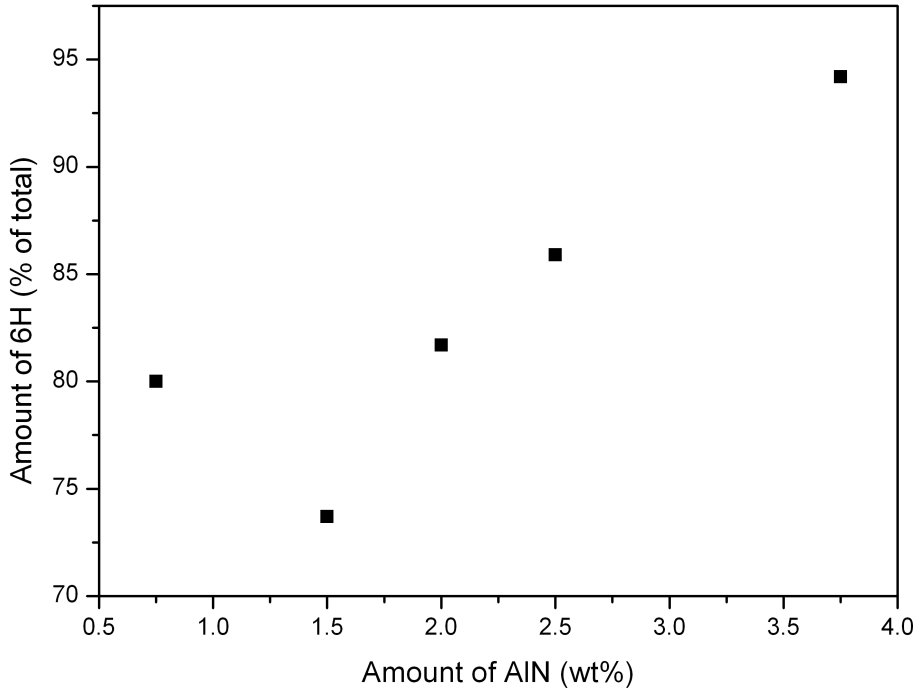


Figure 4.23.: Change in 6H polytype content with the change in the amount of AlN in α-SiC + 3 wt% C SPS samples.

sification process started at a lower temperature in the slow sintering schedule as compared to the fast sintering where the densification started at a slightly higher temperature. This is in agreement with the work of Ray et al. [47] who found that increasing the heating rate from 2.5 °C min^{-1} to 20 °C min^{-1} lead to an increase of 100 °C in the onset of sintering. Also the densification was kick-started by the increase in the pressure during hot pressing.

The time spent at the sintering temperature did not have a huge impact on the final densities. There was no difference in the densities between the samples sintered for 30 minutes or 60 minutes with the densities of 97.0 ± 0.01 and 97.9 ± 0.03% respectively, consistent

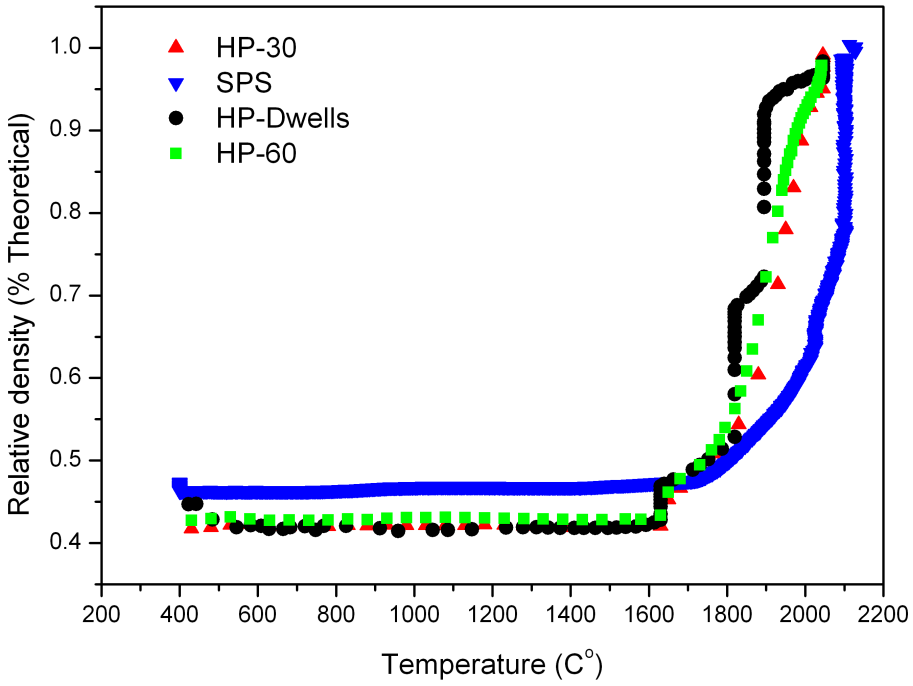
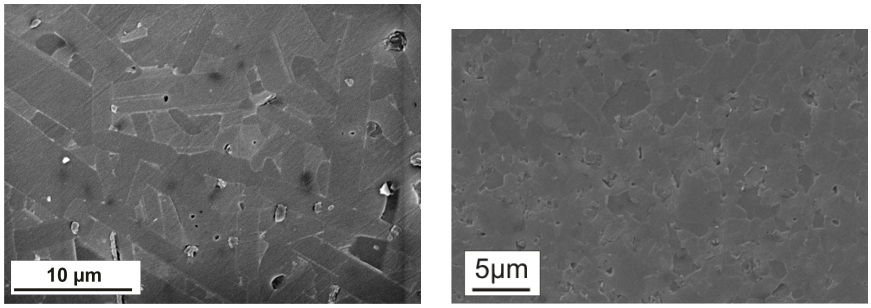


Figure 4.24.: Densification curves for samples sintered using various sintering schedules. All samples had the composition of α-SiC + 3 wt% C + 3.75 wt% AlN.

with the observations that the ram movement stopped after around 30 minutes. This suggests that the densification process is complete in around 30 minutes and waiting for longer for any further densification to take place does not make a difference. However, a sample with the composition of α-SiC with 3 wt%C and 3.75 wt% AlN hot pressed with intermediate dwells showed relatively large (2.4 x 11.4 μm) elongated grains with an aspect ratio of 5 and remarkable polytype transformation from 96% 6H to 100% 4H. Upon repeating the experiment, the results turned out to be different with equiaxed grains and around 25% polytype transformation from 6H to 4H. The author believes that the original sample showing the complete polytype transformation did not



(a) First attempt (b) Repeated experiment

Figure 4.25.: Micrographs of (a) First attempt (image taken from [123] and (b) Repeated experiment of the sample that nominally contained α-SiC, 3 wt% C and 3.75 wt% AlN. They were both sintered using the HP cycle with intermediate dwells.

have the nominal 3 wt% C. In this early sample, the hard 'agglomerates' due to carbon additions were partially removed rather then crushed into the powder. These agglomerates perhaps contained more carbon leading to the less carbon present in the fine powder that was sintered. This carbon deficiency lead to large grains as well as the polytype transformation. The microstructures of the first attempt and the repeated sample are given in figure 4.25.

The results given in figure 4.26 show that increasing the time spent at sintering temperature lead to a reduction in the amount of 6H and an increase in the amount of 4H confirming the hypothesis as to why no effect of the AlN content was seen in the SPS samples. Some Al was detected in the bulk of a grain in the SPS sintered sample containing 3 wt.%C and 3.75 wt.%AlN as can be seen from figures 4.6 and 4.7 which suggests that some bulk diffusion has taken place but perhaps the transformation of 6H into 4H due to this is relatively small enough

to be in the measurement error range. However, even the most transformed sample only contained around 30% 4H which suggests that the transformation from 6H to 4H is a slow process and that for the 6H to 4H polytype transformation to take place, a SiC-AlN solid solution needs to be formed. As explained above the AlN distributes in the SiC-AlN powder mixture through grain boundary diffusion and/or evaporation-recondensation. However, for the formation of SiC-AlN solid solution, it has to diffuse into the SiC grains. This process has to be through bulk diffusion which is a slow process. The polytype transformation from 6H to 4H can be taken as a sign of formation of this solid solution. The increase in the 4H polytype with time suggests an increase in the SiC-AlN solid solution with time confirming the occurrence of bulk diffusion of AlN into SiC grains.

Finally, figure 4.27 shows the effects of sintering time on the grain size of the sintered samples. The graph shows that increasing the time spent at sintering temperature leads to a slight increase in the grain size due to grain coarsening [126].

4.5. Conclusions

The powder processing was found to be capable of achieving a homogeneous distribution of the AlN at a level consistent with the AlN being present as individual particles. The start of densification was found to coincide with an increase in the homogeneity of AlN between 1700 °C and 1850 °C. The proposed mechanism of this re-distribution

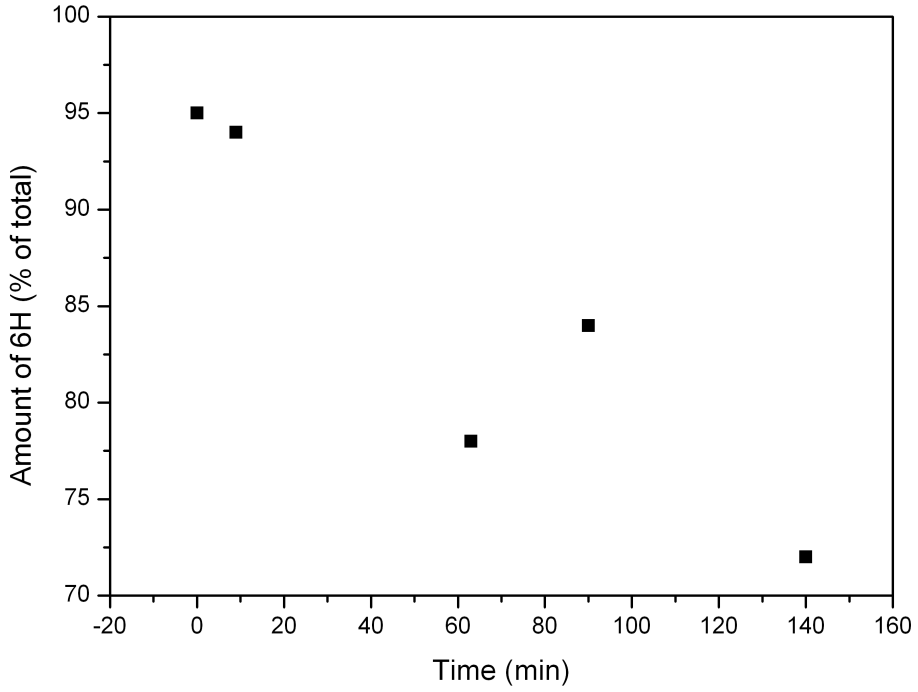


Figure 4.26.: 6H content as a function of the time spent at sintering temperature for three α-SiC samples all containing 3 wt% C and 3.75 wt% AlN. Increasing time at sintering temperature increases 6H to 4H polytype transformation.

is through grain boundary diffusion or evaporation-recondensation. Although a minimum amount of AlN (~ 0.75 wt%) is necessary to densify SiC in hot pressing, the exact amount did not have a huge impact on the grain size or the sintering behaviour of the material. After sintering, AlN was found on the grain boundaries and in triple junctions. However, some traces of Al were also detected inside the SiC grains. Increasing the amount of AlN in the starting powder lead to an increase in the amount present on the grain boundaries. Some evidence of the polytype transformation suggested by Zangvil and Ruh [7] was observed however, the differences were within the error of the measure-

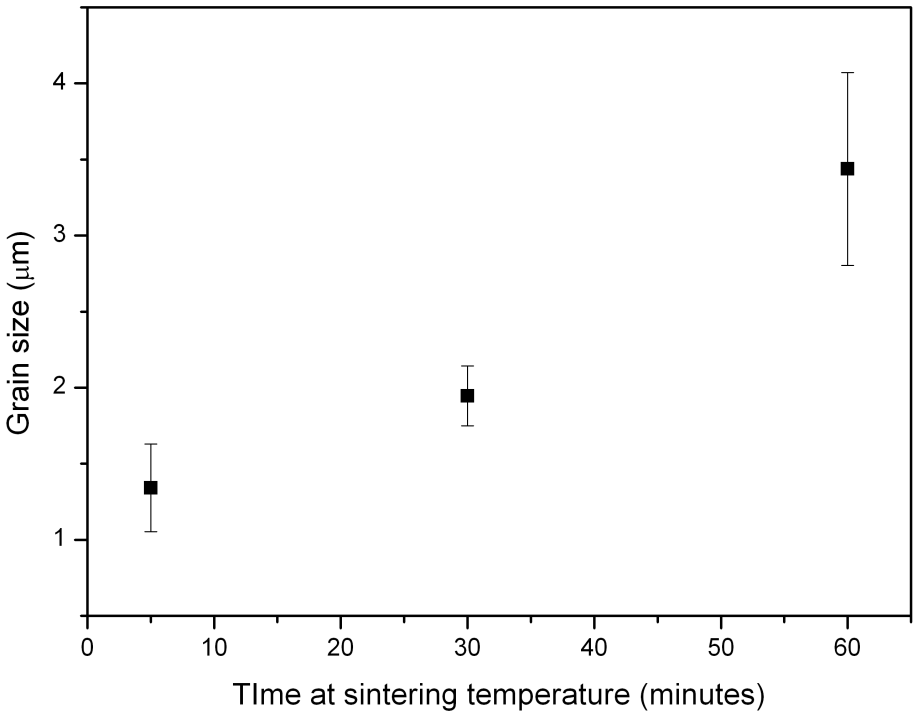


Figure 4.27.: Time spent at sintering temperature for three α-SiC samples all containing 3 wt% C and 3.75 wt% AlN. Increasing time at sintering temprature increases grain size.

ment method.

It is suggested that the polytype transformation from 6H to 4H in SiC can be taken as an indicator of the formation of SiC-AlN solid solution. This can only happen if AlN diffuses into the SiC grains through bulk diffusion. That is why there was some evidence to suggest that increasing the time spent at sintering temperature leads to an increase in the polytype transformation.

AlN + yttria doped SiC samples showed the presence of liquid phase in the microstructure. No evidence of liquid phase was found in the SiC samples containing carbon and AlN. This is consistent with some

findings in the literature[14]. The evidence for a liquid phase when only AlN is added is more limited suggesting that sintering is via solid state diffusion. However, the presence of small amount of liquid phase on the grain boundaries cannot be ruled out.

In line with the work of Clegg [14] and Ermer and Wieslaw [16], carbon can limit grain growth. Since grain size decreases with AlN content, it is proposed that AlN can also restrict grain growth.

5. Small scale indentation

One reason for adding AlN as a sintering additive to SiC was to improve the hardness response of SiC with a minimal impact on the toughness. This is believed to be the case because AlN promotes the formation of equi-axed grains whereas the use of carbon keeps the grains finer [14, 16].

However, such a sweeping statement is dangerous because hardness is a system property: it depends both on a range of material properties as well as on the properties and shape of the indenter.

A wide range of deformation mechanisms can contribute to the size of the imprint. There is always elastic deformation, but additionally plasticity [127], phase transformations [128–131] and cracking [111] can be initiated as well. The latter typically only occurs when higher loads are applied. So when indents are small, only the elastic and plastic properties of the material and the shape and properties of the indenter will determine its hardness.

This chapter is therefore devoted to investigating the effect of the SiC microstructure on the hardness at the small scale where permanent deformation should only be due to plasticity. In such cases, the

measured hardness can be related to the yield strength of the material [63, 79, 83, 132–137]. In ceramics such as SiC, the yield strength can be expected to be dominated by the Peierls stress and therefore in contrast to arguments being made about the effect of grain size, the microstructure should perhaps not matter too much. This is a first question the work reported in this chapter sought to clarify.

Secondly, the Peierls stress is the resistance to dislocation motion due to energy changes in the lattice when the dislocation moves through the lattice at 0 K. Normal compression testing of ceramics is only viable at high temperatures or under confining pressures. Such experiments are cumbersome and determination of the Peierls stress requires extrapolation to 0 K from very high temperatures. Therefore, a second question this chapter tries to answer is whether near room temperature measurements of the hardness using different strain rates can be used to obtain reasonable estimates of the Peierls stress.

Hence this chapter contains two sections: in the first, the hardness of markedly different microstructures will be contrasted with the hardness measured on single crystal substrates of SiC to clarify whether microstructure has a strong effect on hardness of SiC near room temperature. The second section compares the estimates of the Peierls stress and the activation energy to move dislocations by indentation to the results obtained elsewhere by compression tests at high temperature to evaluate the determination of such properties from indentation data.

5.1. Effects of microstructure on hardness and stiffness

Berkovich indents were made using loads of 100 mN, 200 mN and 400 mN into various samples of SiC, polished to 1 μm or better.

As shown in figure 5.1, the difference in hardness of samples sintered using SPS with various amounts of AlN is very small at this scale. Even the effect of a liquid phase on the grain boundaries as in the sample with yttria does not make a significant difference to the hardness.

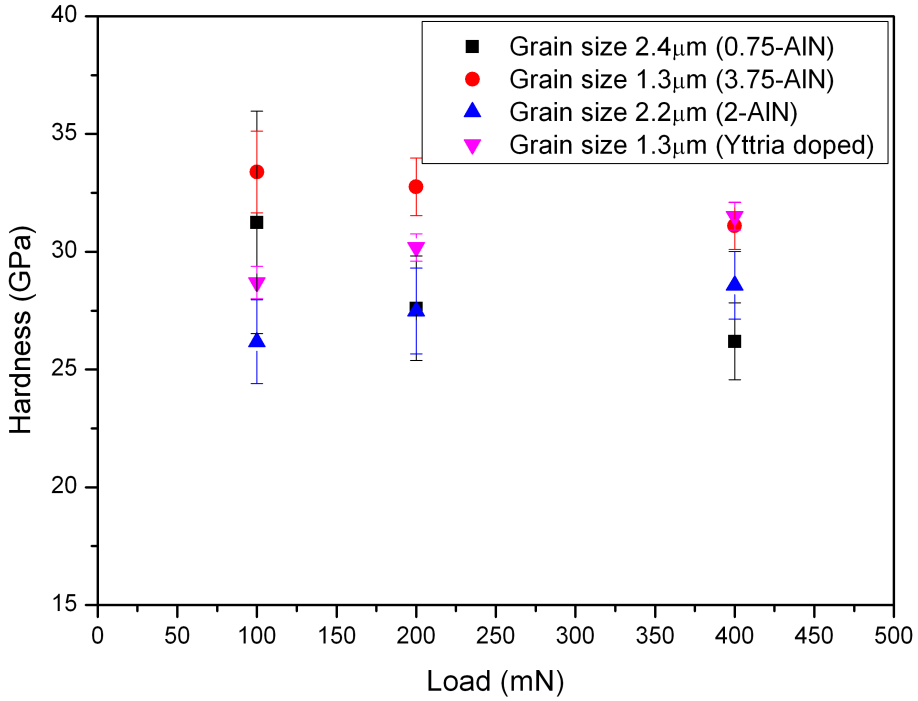


Figure 5.1.: hardness as a function of applied load for samples with different grain size and compositions. All samples were SPSed at 2100 °C for 5 minutes.

The hardness of SiC at the nano-scale (figure 5.1) is higher than

the hardness reported [99] for SiC at macro scale which is consistent with the indentation size effect argument that hardness drops with increasing load. Some evidence of this is observed even in this nano-indentation region too. However, an exception was the hardness results from the 2 wt% AlN sample where hardness actually increased with load. This effect is attributed to the bluntness of the tips this sample was measured at the end of a long series of measurements. Indenting with a blunt Berkovich tip is similar to spherical indentation where the area to depth ratio is not constant. In spherical indentation, the initial contact is elastic and the pressure increases with applied load. Plastic deformation only occurs when a sufficiently high load is reached. Moreover, work hardening takes place and the hardness seems to be increasing with increasing depth [138]. This effect is more prominent in hard ceramics because of the low indentation depth. For example, the indentation depth was only 1 μm at 400 mN load for an SPSed sample with composition fo SiC + 0.75 wt% AlN and 3 wt% C.

If the comparison is made between the hardness and the grain size (figure 5.2) then the hardness is seen to vary with grain size but not systematically. In any case there is no reduction for an increase in hardness for smaller grains. This goes against the idea that the hardness would increase with a reduction in the grain size because grain boundaries act as barriers to dislocation motion making it harder for the material to plastically deform. However, this principle should perhaps not apply in materials where the stress required to move a dislocation through the lattice [127] is the rate determining step as the grain

boundaries will then be of secondary importance.

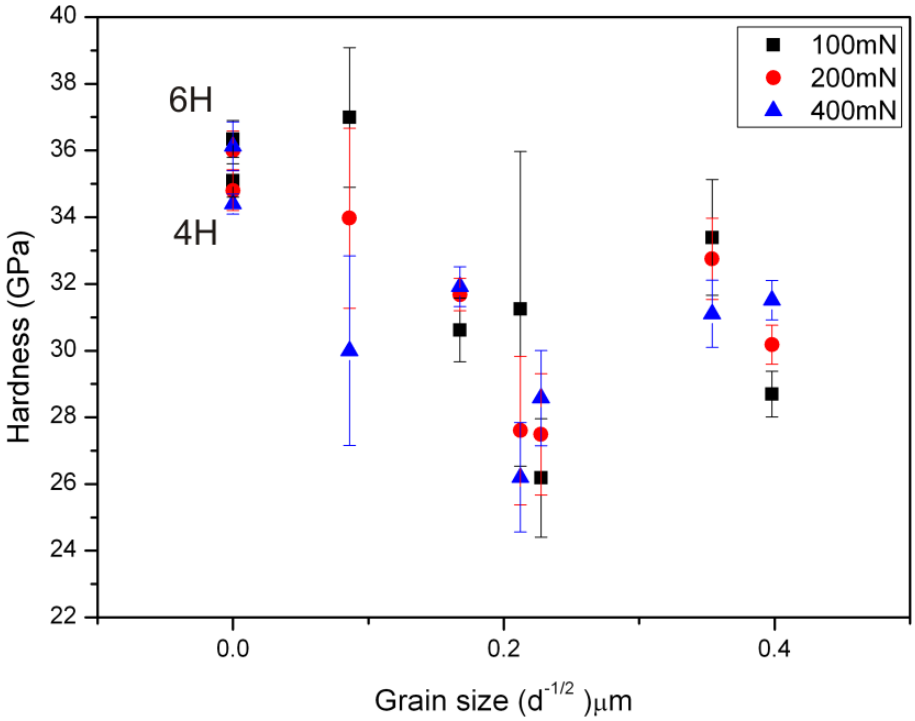


Figure 5.2.: Effect of grain size on nano-hardness. The hardness of SPS as well as HP sintered SiC samples is given. The hardness at zero of x-axis is the hardness of 6H−SiC and 4H−SiC single crystals for comparison.

The small differences in hardness can be explained by points of weakness in the material. For example, if an indent is made closer to a pore then the material has some space to be pushed into which makes it easier for the indenter to penetrate deeper into the sample resulting in lower hardness. Consistent with this, figure 5.2 reveals that the hardness of larger grained sample is higher than that of the finer grain samples. In such large grained materials the pores are still found mostly between the grains (see Chapter 4), and therefore indents are made in essentially single crystals of SiC. In fact the hardness of the large

grained sample is close to the hardness of the single crystal.

If the size of the indent is small compared to the grain size then the indent is not affected by the porosity and the hardness is effectively close to the hardness of that particular single grain. The single crystals of two different polytypes have slightly different hardness (figure 5.2), which is in agreement with the work of Umeno et al. [6] that different polytypes have slightly different mechanical properties. The higher scatter for polycrystalline samples compared to the single crystals indicates that at this scale, the effect of plastic anisotropy on hardness is contributing to the small differences in hardness observed. In contrast, when indenting finer grained materials, even small indents cover a large fraction of single grain and hence avoiding the influence of porosity becomes difficult.

Increasing the time spent at sintering temperature appears to reduce the nano-hardness (figure 5.3). It can be argued that sintering time leads to formation of the SiC-AlN solid solution which has slightly lower hardness [139] which reduced the hardness. The presence of small amounts of AlN on the grain boundaries is not expected to have an impact on nano-hardness.

A key finding from this study is that the nano-indentation hardness in SiC is independent of the grain boundary phase or even to some extent the size of grains. Almost all samples showed similar hardness and indentation response.

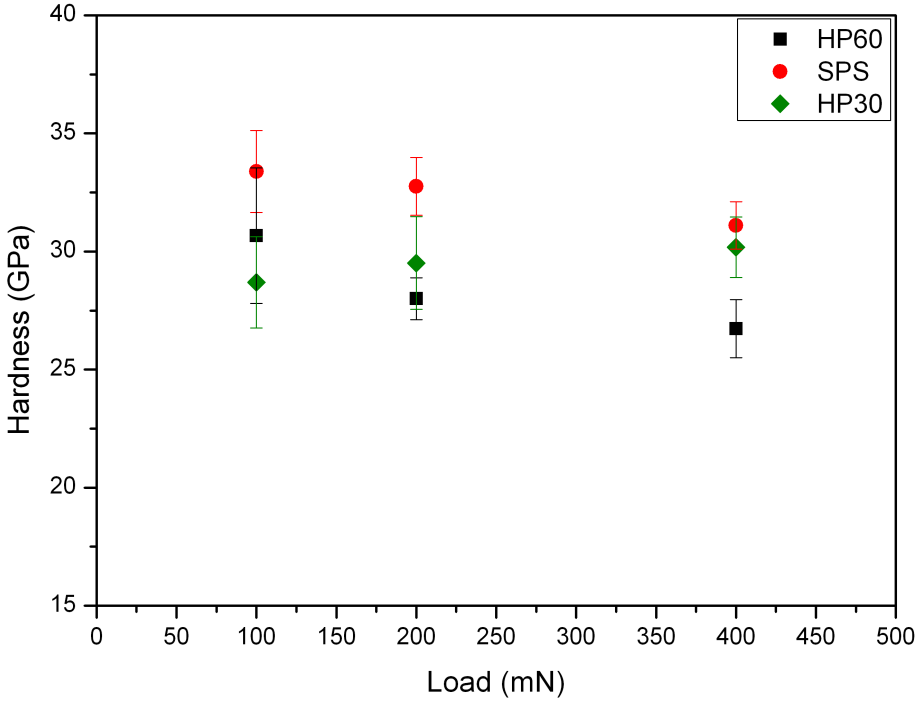


Figure 5.3.: Increasing time spent at sintering temperature reduces the hardness. Both sample types had the same composition of α-SiC + 3 wt% C + 3.75 wt% AlN. HP60 spent 60 minutes at sintering temperature (2045 °C) whereas SPS only spent 5 minutes at sintering temperature (2100 °C).

5.2. Measurement of plasticity parameters

The previous section indicates that hardness does not seem to be affected by the grain boundaries or the phases present on the grain boundaries. This suggests that perhaps grain boundaries do not control the plasticity. Plasticity is controlled by the strongest obstacle to the dislocation motion. Therefore, unlike in metals, in hard ceramics at room temperature, the grain boundaries are not the strongest bar-

riers to dislocation motion in hard ceramics but rather the stress to move the dislocations within the lattice determines the deformation.

Measurements of the plasticity parameters, which describe the lattice resistance, such as activation energy, Peierls stress and activation volume should be able to provide further evidence that the deformation behaviour of SiC at room temperature is controlled by the lattice resistance and establish whether the addition of AlN really has an influence on its deformation or indentation response.

The method employed to calculate the Peierls stress, activation volume and activation energy is nano-indentation at various temperatures and loading rates. The loading rates can be converted into strain rates to establish the effects of strain rates on the hardness response of the material. Known relationships between hardness, yield stress and shear flow stress of hard ceramics have been employed to measure the shear flow stress. The shear flow stresses measured at various temperatures will be used to extrapolate back to 0 K temperature to estimate the value of Peierls stress.

5.2.1. Development of model to measure plasticity parameters of SiC

To measure the Peierls stress, activation volume and activation energy, first, the relation between strain rate and applied stress for the lattice resistance will be derived. As shown in figure 5.4 the shear strain, γ when a single dislocation moves through a sample of length, L can be

expressed as:

$$\gamma = \frac{b}{D} \tag{5.1}$$

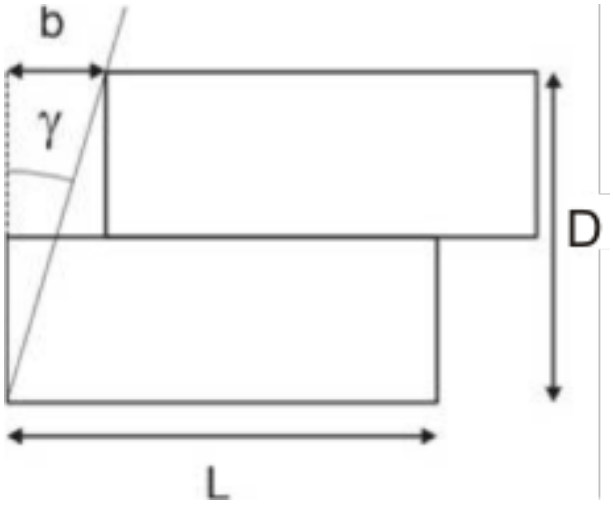


Figure 5.4.: Schematic showing relationship between strain γ, Burgers' vector b and the dimensions of the sample.

Where D is the distance between two atomic layers. and ℓ is the distance travelled by dislocation between two atomic layers in one step.

For an intermediate stage during the dislocation motion where ℓ is a distance smaller than L, the strain is only

$$\gamma = \frac{b}{D} \cdot \frac{\ell}{L} \tag{5.2}$$

Differentiating 5.2 with respect to time , t given:

$$\frac{d\gamma}{dt} = \frac{b}{DL} \cdot \frac{d\ell}{dt} \tag{5.3}$$

where

$$\frac{d\ell}{dt} = \omega \tag{5.4}$$

ω is the dislocation velocity. For N parallel dislocations

$$\frac{d\gamma}{dt} = \frac{N}{DL} \cdot b\omega \tag{5.5}$$

and

$$\frac{N}{DL} = \rho_m \tag{5.6}$$

where ρ_m is the mobile dislocation density hence;

$$\frac{d\gamma}{dt} = \rho_m \cdot b \cdot \omega \tag{5.7}$$

where $\frac{d\gamma}{dt}$ is the strain rate and b is the Burgers vector.

ω depends on the Burgers vector, which is the the distance travelled by dislocation with one jump, and the number of successful jumps per unit time. This in turn depends on the attempts made multiplied by the likelihood of their success.

In the absence of any stress, the dislocations jump in both forward and backward directions which can be expressed as:

$$\omega = v \cdot b \cdot exp\left(-\frac{Q}{kT}\right) - v \cdot b \cdot exp\left(-\frac{Q}{kT}\right) \tag{5.8}$$

where v is the attempt frequency, Q is the activation energy, k is the Boltzman constant and T is temperature. In the presence of the

stress, equation 5.8 can be converted into equation 5.9

$$\omega = v \cdot b \cdot exp\left(-\frac{Q - \tau V_a}{kT}\right) - v \cdot b \cdot exp\left(-\frac{Q + \tau V_a}{kT}\right) \tag{5.9}$$

or

$$\omega = v \cdot b \cdot exp\left(-\frac{Q}{kT}\right)\left[exp\left(\frac{\tau V_a}{kT}\right) - exp\left(-\frac{\tau V_a}{kT}\right)\right] \tag{5.10}$$

where τ is the applied shear stress, V_a is the activation volume which is defined as the volume the single dislocation sweeps through when it moves by one Burgers vector as shown in figure 5.5 [140]

If stress is applied then the number of dislocations jumping in the direction of the stress will increase. For high applied stress

$$exp\left(\frac{\tau V_a}{kT}\right) >> exp\left(-\frac{\tau V_a}{kT}\right) \tag{5.11}$$

So if the backward jump of the dislocations is ignored then equation 5.10 can be simplified to equation 5.12.

$$\omega = v \cdot b \cdot exp\left(-\frac{Q}{kT}\right) exp\left(\frac{\tau V_a}{kT}\right) \tag{5.12}$$

Now if equation 5.7 is combined with equation 5.12 then

$$\frac{d\gamma}{dt} = \rho_m \cdot b^2 \cdot v \cdot exp\left(-\frac{Q}{kT}\right) exp\left(\frac{\tau V_a}{kT}\right) \tag{5.13}$$

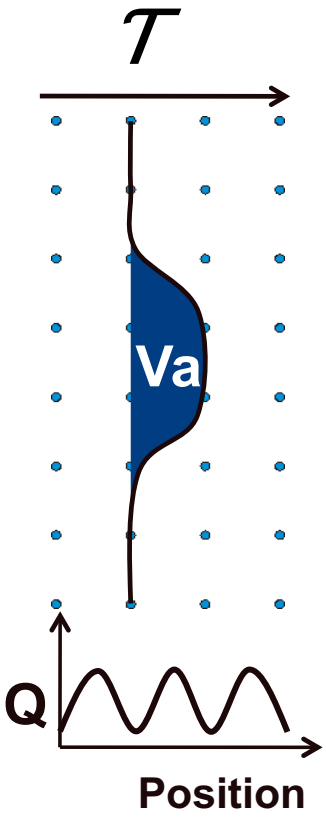


Figure 5.5.: A schematic to show in physical terms the projected activation volume, V_a and dislocation movement. Activation energy Q is the energy required for the dislocation to move from one plane to the next. The arrow shows the direction of shear flow stress τ.

Solving equation 5.13 for applied stress yields:

$$\tau = \frac{kT}{V_a} \cdot ln \left[\left(\frac{1}{\rho_m \cdot b^2 \cdot v} \frac{d\gamma}{dt} \right) exp \left(\frac{Q}{kT} \right) \right] \tag{5.14}$$

or

$$\tau = \frac{Q}{V_a} + \frac{kT}{V_a} ln \left[\frac{d\gamma}{dt}\right] - \frac{kT}{V_a} ln \left[\rho_m \cdot b^2 \cdot v\right] \tag{5.15}$$

If it is assumed that the activation volume V_a remains constant with temperature then

$$Q = \tau_p V_a \tag{5.16}$$

where τ_p is the stress required to move a dislocation by one step at 0 K otherwise known as the Peierls' stress. Then equation 5.15 can be simplified further to.

$$\tau = \tau_p + \frac{kT}{V_a} ln \left[\frac{d\gamma}{dt}\right] - \frac{kT}{V_a} ln \left[\rho_m \cdot b^2 \cdot v\right] \tag{5.17}$$

By using equation 5.17, plasticity parameters for silicon carbide can be calculated. The data for this model can be obtained from nano-indentation experiments.

5.2.2. Obtaining the data for the model using nano-indentation

The nano-indentation experiments were designed with the aim of measuring the strain rates and shear flow stresses at various temperatures to use in the model and calculate the plasticity parameters. Since the model assumes pure plastic deformation with no cracks, crushing or phase changes, they have to be avoided by selecting an appropriate experimental setup. For this purpose the Berkovich diamond tip at

loads where there was no cracking was used.

The samples 6H and 4H single crystals of SiC, a fine grained (1.7 μm) sample of SiC containg 2.5 wt%AlN and 3 wt% C produced by SPS, and a coarser grained (8.6 μm with aspect ratio of 3.6) SiC sample containing 3.75 wt% AlN and some carbon produced by HP-Dwells sintering schedule (see table 3.3), using loads of 100 mN and 200 mN. The loads were taken so that the cracking could be avoided during indentation. An SEM image of an indent made using 200 mN load is given in figure 5.6.

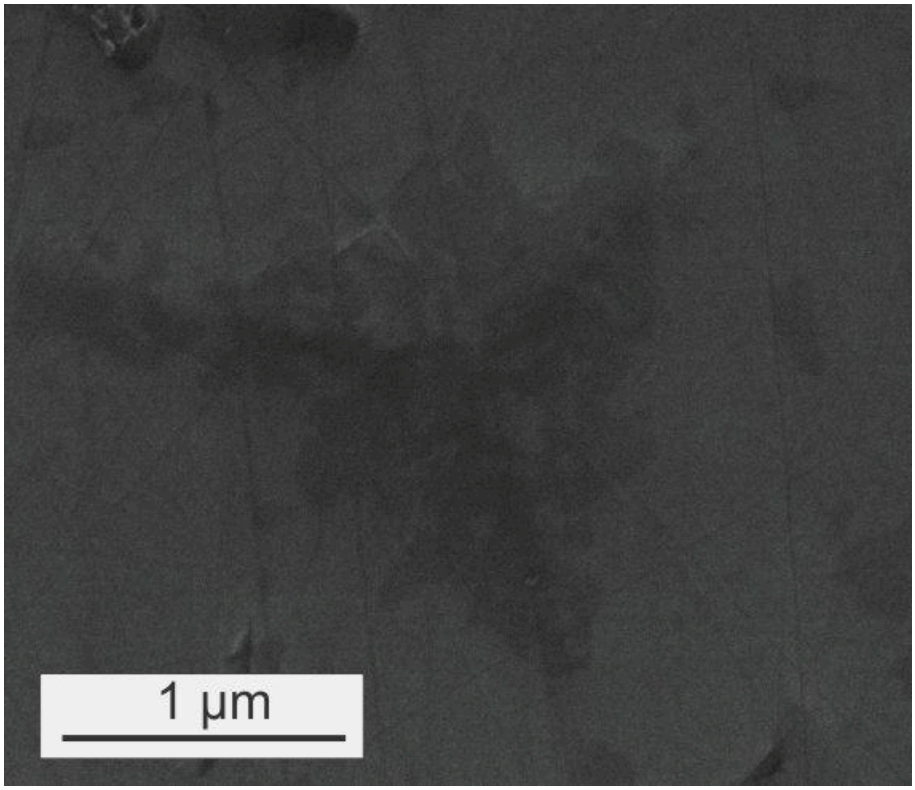


Figure 5.6.: SEM image of a nano-indent made using 200 mN load in the sample containing 2.5 wt%AlN and 3 wt% C produced by SPS. No cracks can be seen at the corners of the indent.

The loading rates chosen were such that the maximum loads were achieved in 4, 20 and 100 seconds. The indentations in the coarse grained sample were carried out at 295 K, 373 K and 473 K. Other samples were indented at room temperature only. 10 indents were made at each load, loading rate and temperature.

Methods to measure the strain rate for loading rates in nano-indentation

The loading rates can be changed in order to change the rate at which the material has been strained. These loading rates can be changed into strain rates, $\dot{\gamma}$ to see the effects of strain rates on hardness using equation 5.18.

$$\dot{\gamma} = \frac{d\gamma}{dt} = \frac{1}{h_t} \cdot \frac{dh_t}{dt} \tag{5.18}$$

where h_t is the total displacement of the indenter. A graph of hardness versus strain rate from simple average strain rates calculated from loading rates and loads using the equation 5.18 is shown in figure 5.7.

Figure 5.7 reveals that temperature clearly affects hardness but the strain rate during loading apparently has no effect. However, an important consideration is that the hardness is measured at the end of the loading curve and after a dwell which is needed to equilibrate the displacement. However, plastic flow occurs [141, 142] during the dwell resulting in eradication of any loading effects on hardness (see schematic figure 5.8). Another problem is only one hardness value is extracted

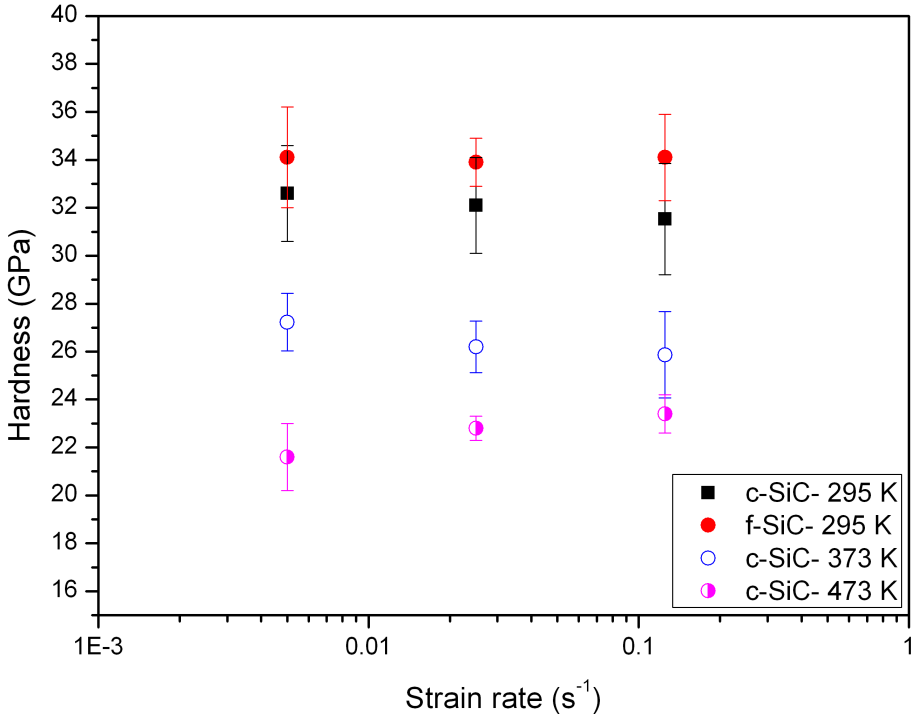


Figure 5.7.: Graph showing the effect of strain rate and temperature on hardness for both coarse (8.6 $\pm$ 3.3 μm) (SiC with + 3.75 wt% AlN and some carbon sintered using HP-D sintering schedule (see table 3.3) and fine grained (1.7 $\pm$ 0.3 μm) (SiC + 2.5 wt% AlN + 3 wt% C SPSed for 5 minutes at 2100 °C) SiC. Hardness values are for 200 mN load and calculated from unloading slope.

from each indent because of the need of an unloading slope to measure the hardness.

As a result of this, there was a need to measure the hardness before the dwell time and in fact at all the points on the loading curve. The loading rates can be converted into strain rate all along the loading curve using the expression given in 5.18

Now the next step is to calculate hardness at all the points on the loading curve. As can be seen from figure 3.6, the hardness calculations

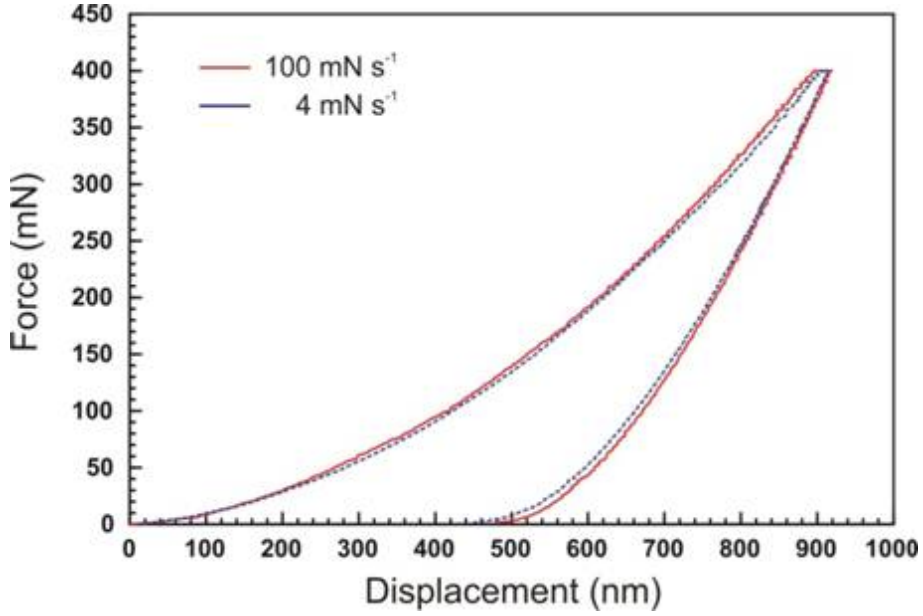


Figure 5.8.: A schematic of load vs displacement curves produced at two different strain rates. Strain rate effects disappear as the hardness is calculated from unloading.

require knowledge of the slope of the initial unloading curve which is used to separate the elastic and plastic response of the material during indentation. This can then be used to estimate the area of the indent after unloading.

However, for a bulk material the Young's modulus should not vary with indentation depth. This is confirmed with experimental data in figure 5.9.

Therefore, for a bulk material the unloading slope can be predicted from Young's modulus by re-arranging equation 3.20.

$$S = 2E_r\sqrt{\frac{A_c}{\pi}} \tag{5.19}$$

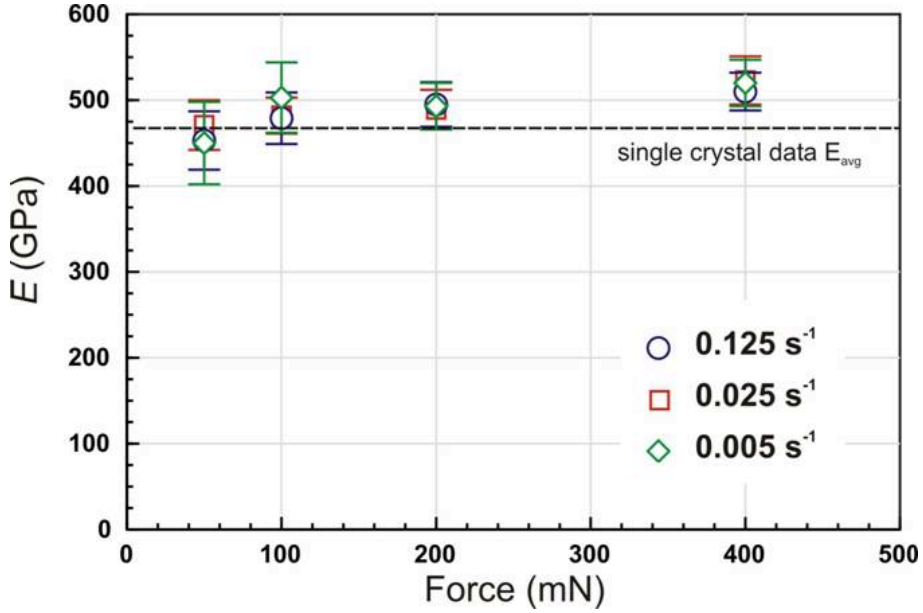


Figure 5.9.: Elastic modulus versus applied load. The sample tested was the fine grained (1.3 ± 0.3 μm) SiC sample with the composition of SiC + 3 wt% C and 3.75 wt% AlN SPSed for 5 minutes at 2100 °C.

Now if the S is replaced in equation 3.18 then

$$h_c = h_t - \epsilon \frac{F}{2E_r}\sqrt{\frac{\pi}{A_c}} \tag{5.20}$$

Equation 5.20 can be iteratively solved. Iterations are necessary as projected area, A_c is a function of contact height, h_c. Hence the hardness at all points on the loading curve as well as from the data collected during dwell at maximum load can be calculated.

Figure 5.10 shows that when instanteneous hardness data is used, the hardness does depend on strain rate. However, the strain rate calculated for the loading curve is based on total strain rate whereas the plasticity model only considers the plastic strain rate.

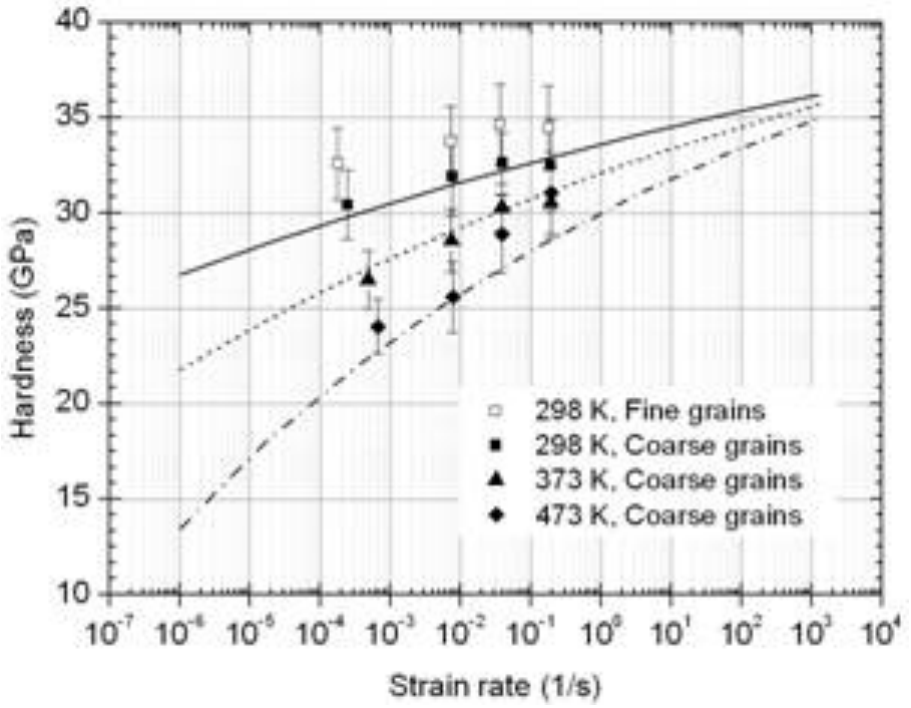


Figure 5.10.: Hardness against strain rate showing that hardness for instantaneous hardness values increases with increasing strain rate for a change in load based strain rate calculation. Fine grains are 1.7 μm and coarse grains are 8.6 μm. Lines on the plot are the predicted change in hardness with strain rate using the model developed.

Therefore, Bhakhri et al. [143] proposed that the total strain rate must be divided into a plastic and elastic contribution. Total strain rate $\dot{\gamma}_t$ is the sum of both elastic strain rate $\dot{\gamma}_e$ and plastic strain rate $\dot{\gamma}_p$.

$$\dot{\gamma}_t = \frac{1}{h_t} \cdot \frac{dh_t}{dt} = \dot{\gamma}_p + \dot{\gamma}_e \tag{5.21}$$

which can be written as

$$\frac{1}{h_t} \cdot \frac{dh_t}{dt} = \frac{1}{h_t} \cdot \frac{dh_p}{dt} + \frac{1}{h_t} \cdot \frac{dh_e}{dt} \tag{5.22}$$

They provided a method for calculating the plastic strain rate from the data. Using this method the variation of hardness with strain rate is given in figure 5.11.

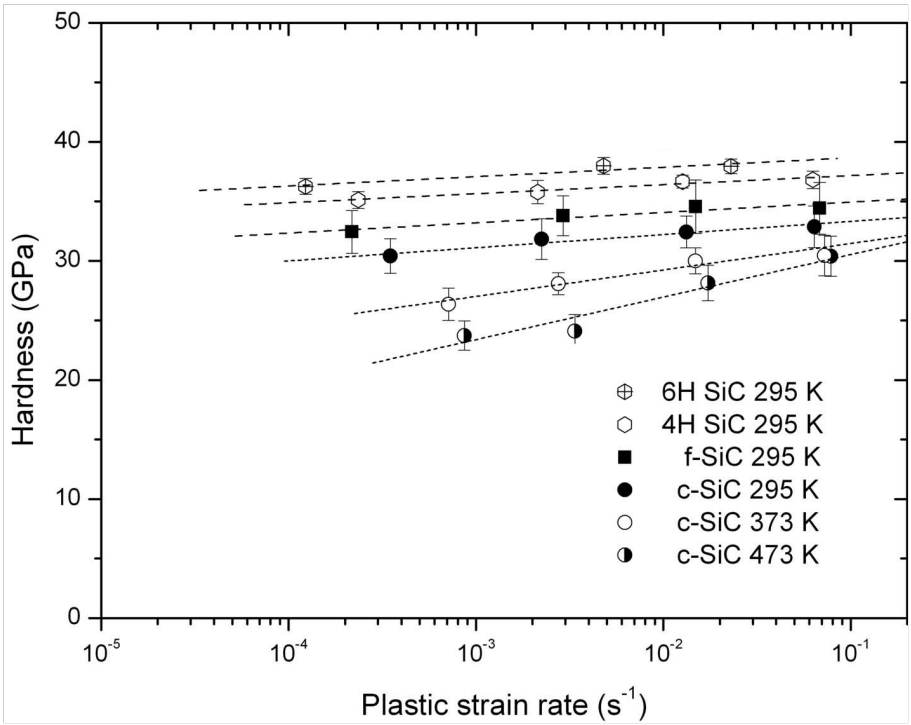


Figure 5.11.: Hardness against strain rate showing that hardness increases with increasing strain rate. f is fine grained SiC, c is coarse grained SiC. 4H and 6H are single crystals of the 4H and 6H SiC polytypes respectively.

It is worth noticing from figure 5.11 that the strain rate sensitivity of both single crystals and polycrystalline materials is the same at room temperature however the hardnesses are different. Hence the strain rate sensitivity of SiC does not depend on its grain size. This

confirms further that the dislocation velocity is not controlled by the grain boundaries. Hence it is not unreasonable to assume that the plastic deformation mechanisms in these ceramics is controlled by the lattice resistance, i.e. the rate of deformation is controlled by the single step through the lattice. The higher hardness of single crystals is due to the orientation of indents relative to the primary slip plane which in SiC is expected to be basal plane [144] and the effect of plastic anisotropy is stronger than the effect of grain boundaries. Again, the higher scatter in the data of the poly crystalline material reflects the fact that the indents were made at various orientations which lead to the scatter.

The coarse grained sample had a large amount (more than 90%) of 4H phase present whereas the fine grained sample was predominantly (more than 90%) 6H. The results indicate that they both behaved in a similar fashion to their respective single crystals. The strain rate effect on room temperature hardness is the same for both single crystals as well as the polycrystals. However, the hardness of 6H single crystals was higher then 4H at all strain rates. Polycrystals also followed the same trend as their respective single crystals. The hardness of 6H single crystal was also higher than 4H at all strain rates.

The temperature had an influence on the strain rate sensitivity which doubled from 0.8 GPa per decade of strain rate at room temperature to 1.6 GPa per decade of strain rate at 100 °C and to 2.7 GPa per decade of strain-rate at 200 °C.

Hence, at these moderate temperatures, the hardness is indeed dom-

inated by the magnitude of the lattice resistance. The size of the grains might become important at higher temperatures but at these relatively low temperatures, they do not appear to have a significant impact on nano-hardness.

Conversion of hardness into shear flow stress

Various models exist to convert hardness into a uni-axial yield stress which can then be converted into shear flow stress, τ. (see figure 5.12

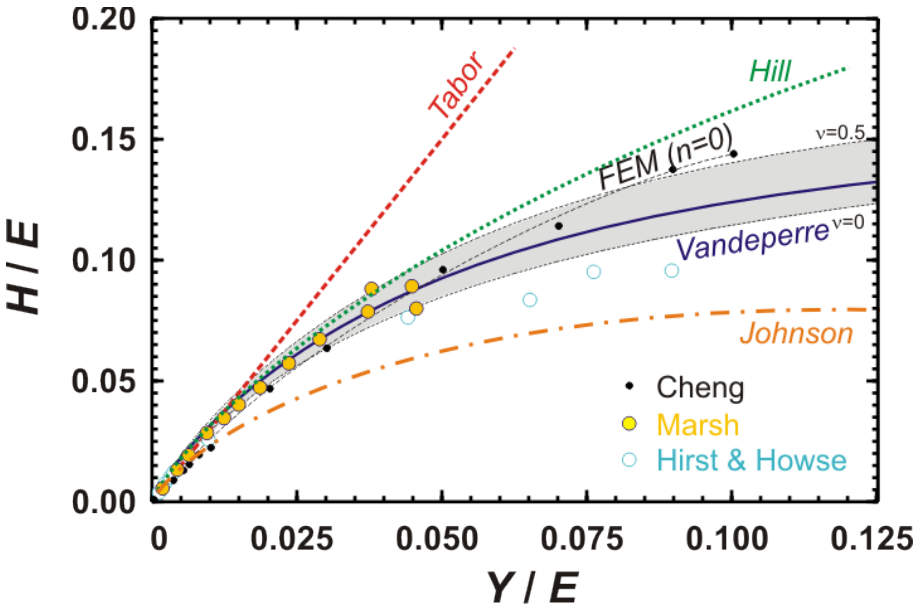


Figure 5.12.: Various models [63, 79, 81, 82, 145–148] and equations used to convert hardness into Yield stress.

Of the analytical models the work by Vandeperre et al.[145] agrees most closely with finite element calculations of Cheng and Cheng [81]. Their [145] analytical model is based on the expanding cavity model [82] and relates hardness and yield stress through:

$$\frac{H}{Y} = \frac{2}{3}\left\{1 + \frac{3}{3-6\lambda} ln\left(\frac{(3+2\mu)\cdot(2\lambda\cdot(1-\zeta)-1)}{(2\lambda\mu-3\mu-6\lambda)\cdot\zeta}\right)\right\} \tag{5.23}$$

where

$$\zeta = \frac{E_r}{E_r - 2H\cdot tan\alpha} \tag{5.24}$$

and

$$\lambda = \frac{(1-2\nu)Y}{E} \tag{5.25}$$

$$\mu = \frac{(1+\nu)Y}{E} \tag{5.26}$$

where E is the Young's modulus, E_r is the reduced modulus, ν is the Poisson ratio, and α is equivalent semi-angle of the indenter. This yield stress was then converted into shear flow stress by dividing it by 2 according to the Tresca yield criterion. The results for the strain rate dependence of the shear flow stress are shown in figure 5.13

5.2.3. Incorporation of data into the model to measure the plasticity parameters

The shear flow stress and strain rate data obtained from nano-indentation experiments can be incorporated into equation 5.17. From this equation, if shear flow stress is plotted against the natural logarithm (Ln)

of strain rate, then the activation volume, V_a can be calculated from the slope of the lines as can be seen from the figure 5.13. The activation volumes were found to be 1.68 $\times$ 10^{-29} m^3, 1.45 $\times$ 10^{-29} m^3 and 1.20 $\times$ 10^{-29} m^3 for the temperatures of 295 K, 373 K and 473 K respectively. Although the activation volume seem to be increasing with increasing temperature, the differences are small. For simplicity, the average value of these three activation volumes was taken which was found to be 1.44 $\times$ 10^{-29} $\pm$ 0.25 $\times$ 10^{-29} m^3 which is around 4 times the Burgers vector cubed, b^3 assuming the deformation is by dislocations present in the basal plane with the Burgers vector b=a/3 [1 1 $\bar{2}$ 0] dissociates into two partial dislocations with Burgers vector of b_1 = a/3 [1 0 $\bar{1}$ 0] and b_2 = a/3 [0 1 $\bar{1}$ 0]. [144]. The Burgers vector was taken to 0.154 nm.

Equation 5.17 can be modified into the form of equation 5.27.

$$\tau = \tau_p - \frac{kT}{V_a} ln \left[\frac{\rho_m \cdot b^2 \cdot v}{\dot{\gamma}} \right] \tag{5.27}$$

From equation 5.27, if shear flow stress is plotted against temperature then the Peierls stress, τ_p, can be read off the y-axis, whereas the product of mobile dislocation density, ρ_m and attempt frequency, v can be calculated from the slopes of the curves as can be seen in figure 5.14.

Once the activation volume and the Peierls stress are known, then equation 5.28 can be used to calculate the activation energy to move dislocation by one step.

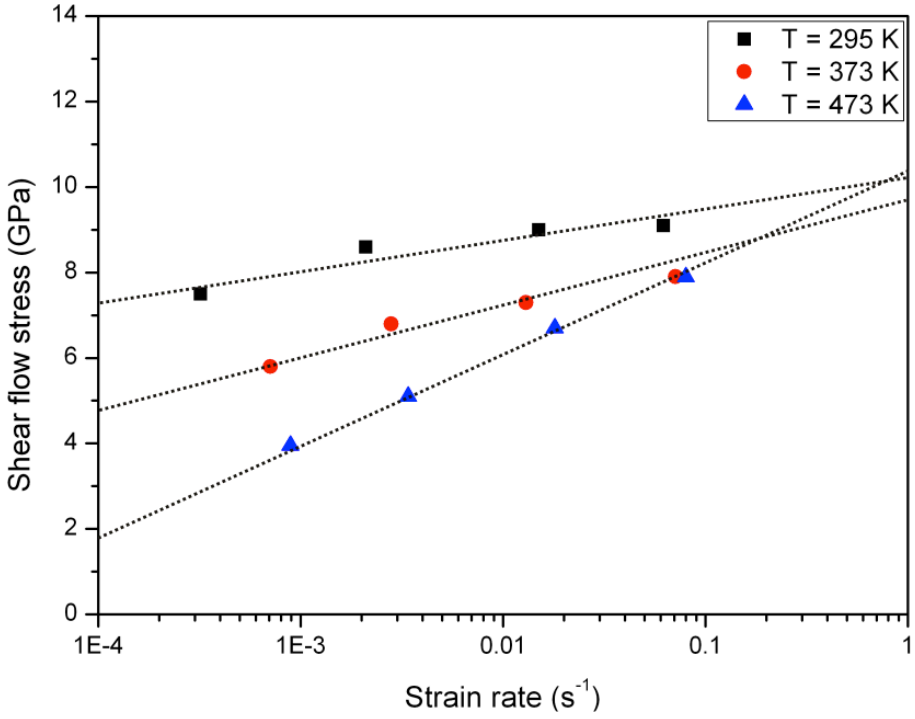


Figure 5.13.: Plot of shear flow stress against the strain rate can be used to calculate the activation volume from the gradients of the curves. the sample tested is SiC + 3.75 wt% AlN and some carbon sintered using HP-Dwells sintering schedule (see table 3.3 for details) with the grain size of 8.6 μm.

$$Q = \tau_p V_a \tag{5.28}$$

The results of these calculations as well as the constants used are given in table 5.1.

Comparing these with published values [127, 149] shows that these estimates are reasonable. The drop in hardness with increase in temperature correlates well with published data as can be seen from figure 5.16. The Peierls stress calculated from indentation is 12 $\pm$ 1 GPa.

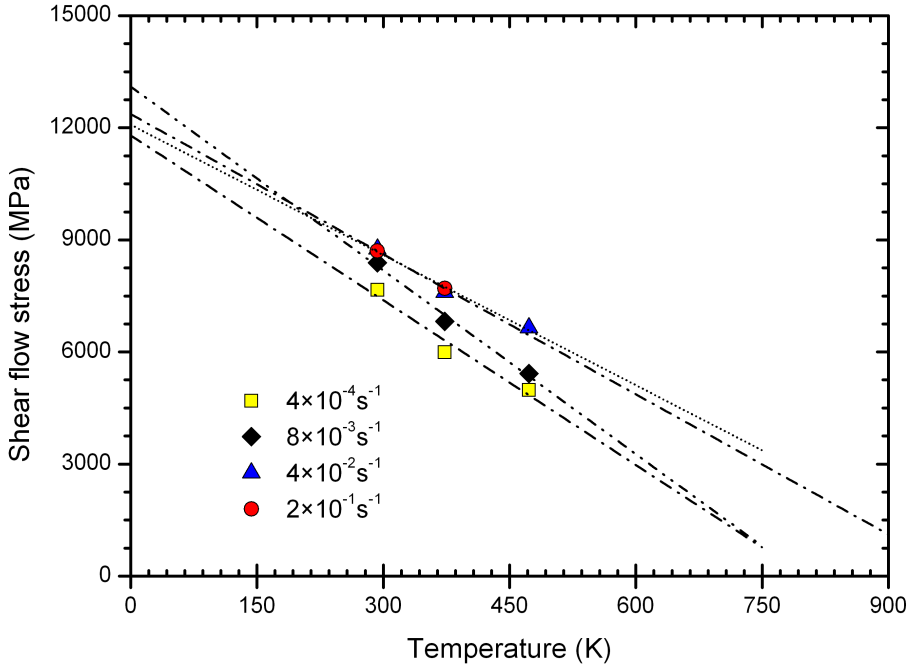


Figure 5.14.: Plot of shear flow stress against temperature. The shear flow stress at 0 K is the Peierls stress whereas the activation volume can be calculated from the slopes of the curves.

The activation energy for dislocations was estimated to be 1.75 ± 0.4 × 10^{-19} J (1.1 ± 0.3 eV). This is in fair agreement with the activation energy from high temperature compression by Fujita et al.[149] and Pirouz et al.[127] which are 3.4 eV and 1.67 ± 0.16 eV respectively. The model quite accurately predicts a drop in hardness with the increase in temperature. This is because of extra energy that is supplied which makes it easier to move dislocations in the material and hence hardness reduces. This suggests that the deformation in hard ceramics is controlled by the Peierls stress of the material. The effect of grain boundaries on the deformation is secondary which explains the hard-

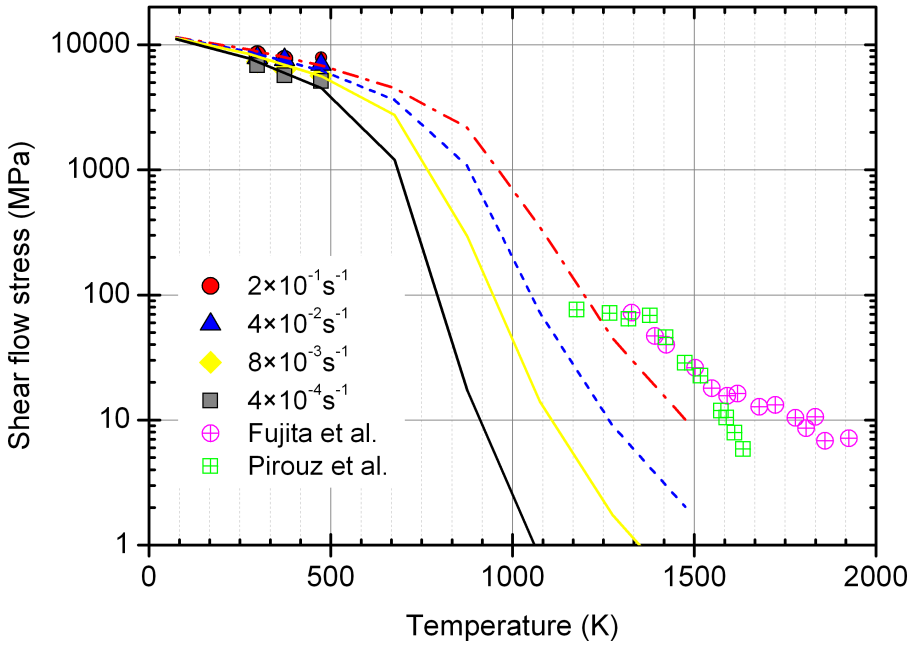


Figure 5.15.: Plot of shear flow stress against temperature. The drop in shear flow stress with increasing temperature is predicted by model and data correlates well with the literature [127, 149].

ness results discussed in the previous section where the amount of AlN on the grain boundaries had no effect on hardness. Plastic anisotropy's influence is stronger than the effect of grain boundaries. This explains why the single crystals were harder then the polycrystalline samples.

5.3. Conclusions

Sintered silicon carbide was indented using very small loads (100 mN, 200 mN and 400 mN) to measure its hardness. As far as any trends with grain size could be established, the hardness increased with increasing grain size and single crystals exhibited the highest hardness.

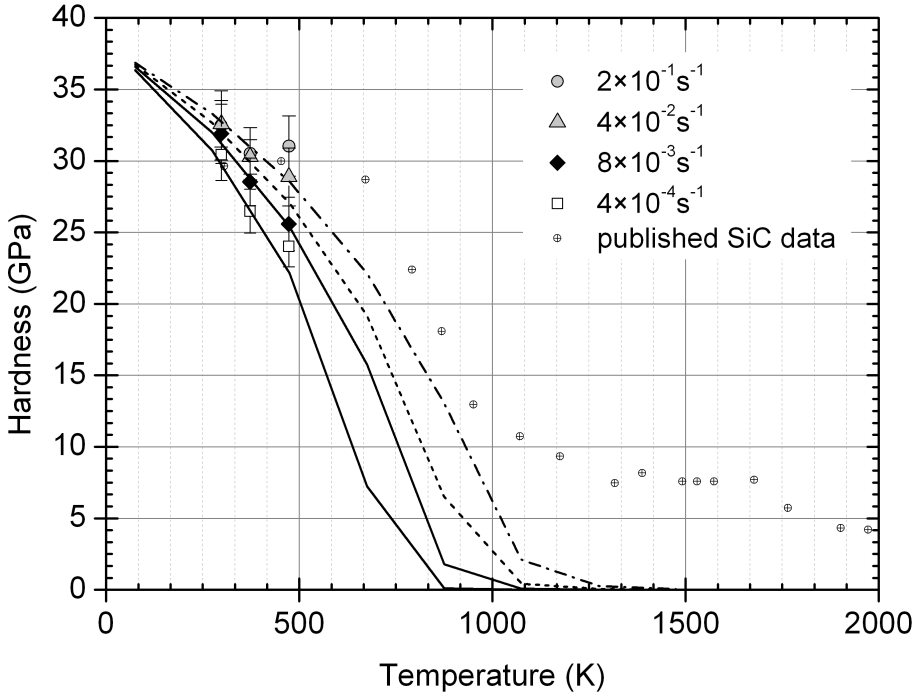


Figure 5.16.: Plot of hardness against temperature. The drop in hardness with increasing temperature predicted by the model correlates well with the literature [127, 149] for SiC single crystals

It is proposed that this is due to limited residual porosity which in large grained material remains far from the indents and hence has only limited influence while pores are closer to the indent in fine equiaxed materials.

The hardness increased with strain rate. The strain rate sensitivity increased with increasing temperature. It doubled from 0.8 GPa per decade increase in strain rate at room temperature to 1.6 GPa per decade strain rate at 100 °C and quadrupled to 2.9 GPa per decade strain rate at 200 °C.

Plasticity parameters were calculated through the development of

Table 5.1.: $\star$ parameters are calculated from the equation. Attempt frequency, v was taken from Frost and Ashby [150], Burgers vector was calculated from assumption of partial dislocations [127, 151, 152].

Property	Value
Boltzmann constant, k	1.38×10^{-23} J K^{-1}
Burgers vector, b	1.54×10^{-10} m
Attempt frequency, v	10^{11} s^{-1}
$\star$Activation volume, V_a	1.44×10^{-29} m^3
$\star$Mobile Dislocation Density, ρ	4×10^{10} - 2×10^{14} m^{-2}
$\star$Peierls stress, τ_p	12 ± 1 GPa
$\star$Activation energy, Q	1.1 ± 0.3 eV

a model. These parameters include, Peierls stress (12 ± 1 GPa), Dislocation activation energy (1.1 ± 0.3 eV) and activation volume (1.44×10^{-29} m^3). The calculated results were in good agreeement with published data for the activation energy from compression tests at high temperatures and can be used to predict the decrease in hardness for higher temperatures.

Hence the determining factor in the plastic flow in SiC near room temperature is the Peierls stress rather than the grain size. It suggests that the grain boundaries and grain size are perhaps of secondary importance in determining plastic deformation in SiC near room temperature.

6. Large scale indentation

After the analysis of small scale indents in the previous chapter, the effects of increasing the size of the indents were investigated to establish how size alters the response of SiC and to determine whether larger indents would reveal differences in behaviour between the different compositions or sintering cycles.

Studying larger scales was also motivated by the idea that depending on the application, contact damage might form at different length scales. To make comparisons with the small scale experiments easier a Vickers indenter was used although other indenter types may be more appropriate. For example, spherical indentation is often used to investigate wear resistance [153–155].

The expected differences in behaviour when the indent size is increased are that cracks will form and that the hardness values are typically lower. Therefore in the first part of this chapter, the variation of hardness with applied load will be discussed. In the second part, the appearance of cracks is used to investigate the interaction of the cracks with the microstructure and therefore potentially establish which toughening mechanisms are active. Indentation cracks are

sometimes also used to measure the actual toughness but various conversions are available and the method has been criticised. The results obtained here are used to evaluate the different approaches in the literature. Finally, the final section of this chapter reports new observations made after unloading.

6.1. Effects of microstructure on hardness

The hardness measurements were carried out at a range of loads to see the effect of scale on the response of the SiC. The hardnesses from Vickers indents have been measured using the projected area rather then the contact area which is usually used for Vickers indentation to enable comparison with results from nano-indentation discussed in the previous chapter.

Figure 6.1 reveals the hardness of SiC samples in this study drops with increasing porosity. This is because the pores provide space for material to move into when it is pushed by the indenter allowing the indenter tip to penetrate deeper into the sample and resulting in a reduced value of hardness. This observation is consistent with the literature [156].

The indentation results given in figure 6.2 of samples containing various amounts of AlN all sintered using fast SPS show that there again is not much difference in hardness response even when larger loads are applied. This confirms that changing the amount of AlN from 0.75 wt% to 3.75 wt% does not affect the hardness behaviour.

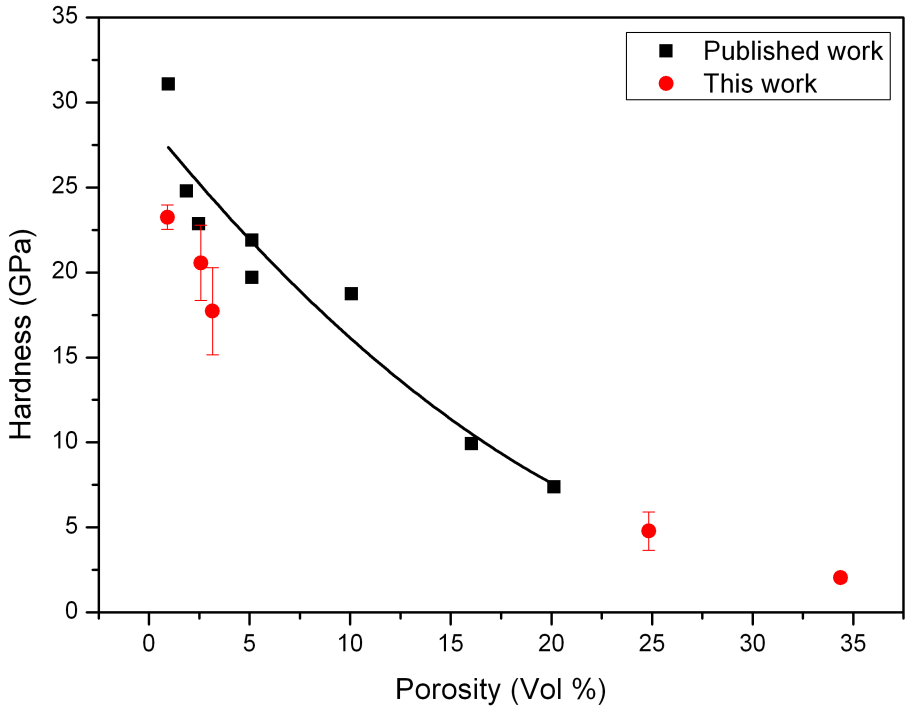


Figure 6.1.: Graph showing a reduction in hardness measured using 5 Kg load with increasing porosity. All samples had the composition of α-SiC + 3 wt% C + 3.75 wt% AlN sintered using various HP and SPS schedules. The published data is taken from Slustker et al.[156].

As explained the hardness drops when the load is increased. This load dependence is stronger in large grained (6 μm) sample as can be seen in figure 6.3. The hardness drops from 36 GPa at 100 mN load to 17 GPa at 49,050 mN. However, a sample with finer grains (2.3 μm), although lower in hardness at small loads, retained its hardness better at higher loads.

This high hardness of the coarse grained sample for low loads can be understood from the fact that in this sample, small indents are made in the fully dense grains and not affected by the intergranular porosity,

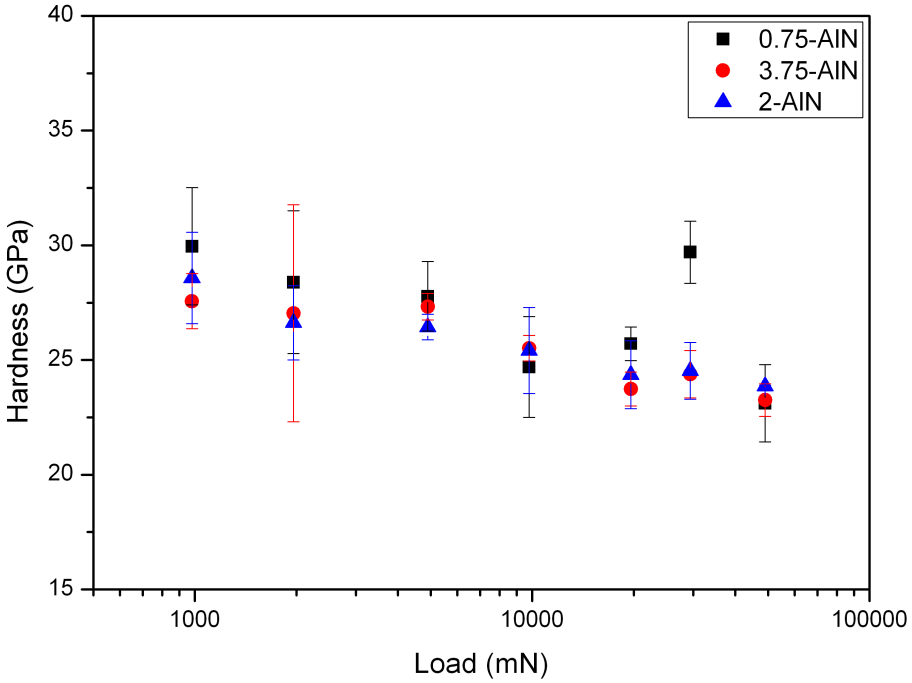


Figure 6.2.: Graph showing how the hardness varies with load for different amounts of AlN. The samples were made by using SPS at 2100 °C for 5 minute.s and all contained α-SiC starting powder and 3 wt% C.

whereas for fine-grained materials, pores do affect the hardness even when making small indents.

Another explanation for lower hardness of coarse grained sample is perhaps linked to its indentation damage mechanisms which are different from all the rest of the sample. As can be seen from figure 6.4 that the large grained sample gets crushed. An example typical of all other samples is given in figure 6.4 as well.

A comparison between the hardness of samples that spent different times at the sintering temperature is given in figure 6.5. It shows that although these samples had slightly different hardness responses

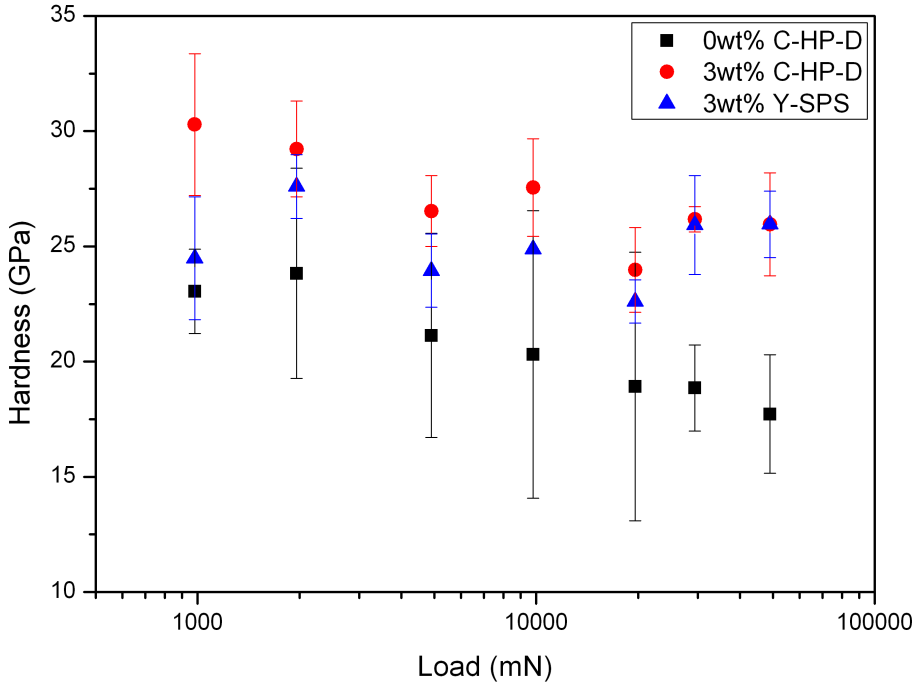
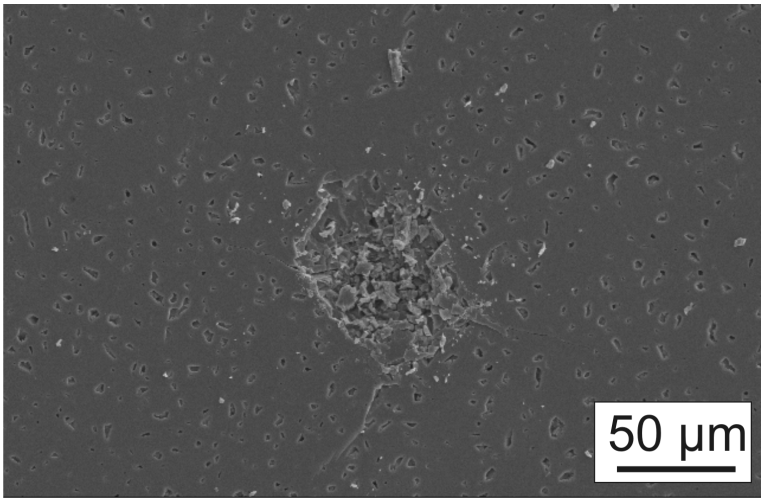


Figure 6.3.: Graph showing a comparison between the sample with large grain size (with 0wt% carbon) and the sample with fine grains (with 3 wt% carbon). The large grained sample drops in hardness much more rapidly then the sample with fine grains. Both samples were sintered using HP-D sintering schedule. SPSed sample had 3 wt% yttria and 3.75 wt% AlN in SiC.

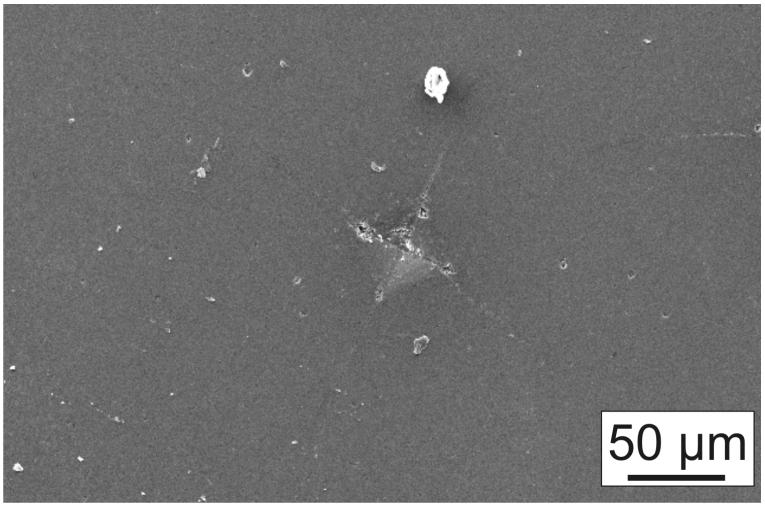
at the nano-indentation scale, their hardness responses at the macro indentation scale are similar.

6.2. Effect of microstructure on cracking in SiC

Once cracks form around indents, their size can be used to obtain an estimate of the toughness. Several relationships between applied load,



(a) No carbon



(b) 3wt% carbon

Figure 6.4.: Cracking in and around the indent made using 5 kg load. (a) Sample with no carbon, (b) Sample with carbon. Both samples were sintered using HP-D schedule and contained α-SiC and 3.75 wt% AlN

stiffness, hardness, crack length and toughness have been proposed, the best known are those of Niihara [96]

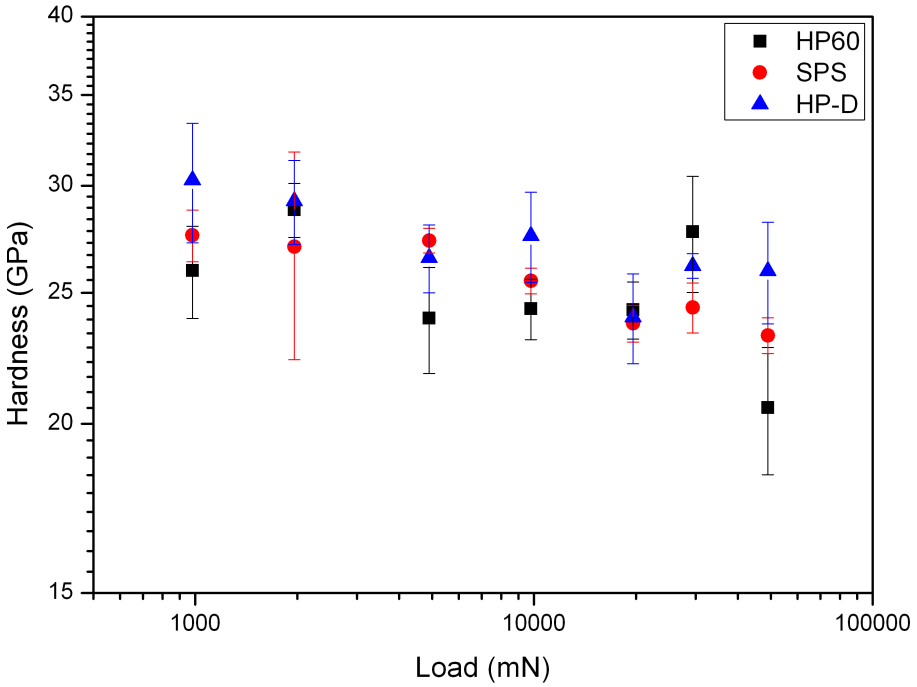


Figure 6.5.: Graph showing a comparison between the sample that spent one hour on the sintering temperature (HP60) and a sample that only spent 5 minutes (SPS). HP-D sample spent half an hour however, it spent longer time at the temperature above 1800 °C then the HP60 sample.The hardness at small scale is higher for SPSed sample.

$$K_{1C} = 0.018 \cdot H\sqrt{a} \cdot \left(\frac{E}{H}\right)^{\frac{2}{5}} \cdot \frac{1}{\sqrt{\frac{c}{a} - 1}} \tag{6.1}$$

$$K_{1C} = 0.067 \cdot H\sqrt{a} \cdot \left(\frac{E}{H}\right)^{\frac{2}{5}} \cdot \frac{1}{\frac{c}{a}^{\frac{3}{2}}} \tag{6.2}$$

and Anstis et al. [77]:

$$K_{1C} = 0.016 \cdot \sqrt{\frac{E}{H}} \cdot \frac{F}{c^{\frac{3}{2}}} \tag{6.3}$$

where K_{1C} is the fracture toughness, H is hardness, a is half of the

diagonal length of the indent, c is the crack length, F is load and E is the Young's modulus.

These crack lengths were measured from SEM images using "Corel Draw" software. The principle is the same as used in measuring the grain size or size of indents where the scale bar is used as a reference length.

Another practical problem is the choice of load at which indentation toughness is to be measured. The hardness drops with load until it reaches a steady state [99]. The indentation toughness can be more accurately measured at the indentation load where the cracks have just reached this steady state.

All the equations given above (6.1, 6.2 and 6.3) were used to measure the toughness of a SiC sample at three different loads. It can be seen from figure 6.6 that they all yield different results that the toughness increases for increasing indentation loads for both methods. However, the increase in the method of Niihara [96] is considerably more than Anstis et al. [77]. This is because of the differences in the assumptions used as well as the different parameters used in the calculations as discussed in the Chapter 2. The Niihara [96] equation for Palmqvist type cracking is closer to results obtained following Anstis et al. [77] whereas Niihara's [96] equation assuming half-penny cracking showed unrealistically high toughness results. It can be concluded that perhaps the crack shape in this load region is closer to Palmqvist then half-penny. However, this cracking pattern changes with load. It was found by Jones et al. [97] that increasing the load leads to extension of

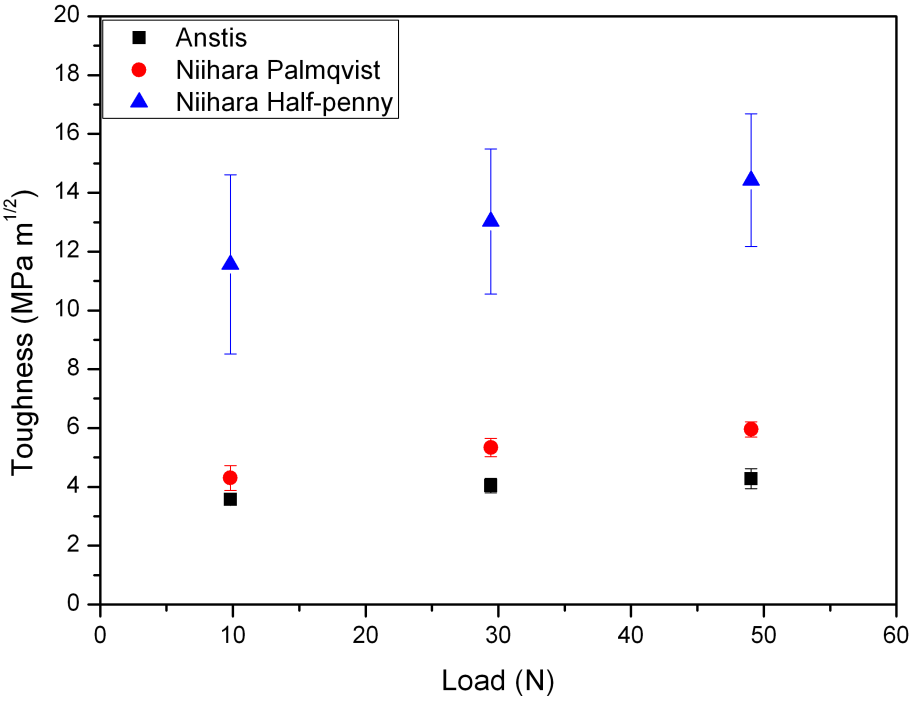


Figure 6.6.: Graph showing indentation toughness of an α-SiC sample containing 3 wt%C and 2 wt% AlN SPSed for 5 minutes as calculated using Niihara [96], and Anstis et al.[77] approaches.

Palmqvist cracks which eventually end up becoming half-penny cracks.

For the purpose of the current study, the absolute toughness value calculation is not the aim but rather a study of how the cracks proceed with load.

The c/a ratios of the samples sintered using SPS containing amounts of AlN in the range from 0.75 wt% to 3.75 wt% are given in figure 6.7

Figure 6.7 suggests that the c/a ratio decreases with increasing amount of AlN however the differences between the samples are within the error range. This result suggests that the changes in the amounts of AlN from 0.75 wt% to 3.75 wt% does not influence the crack prop-

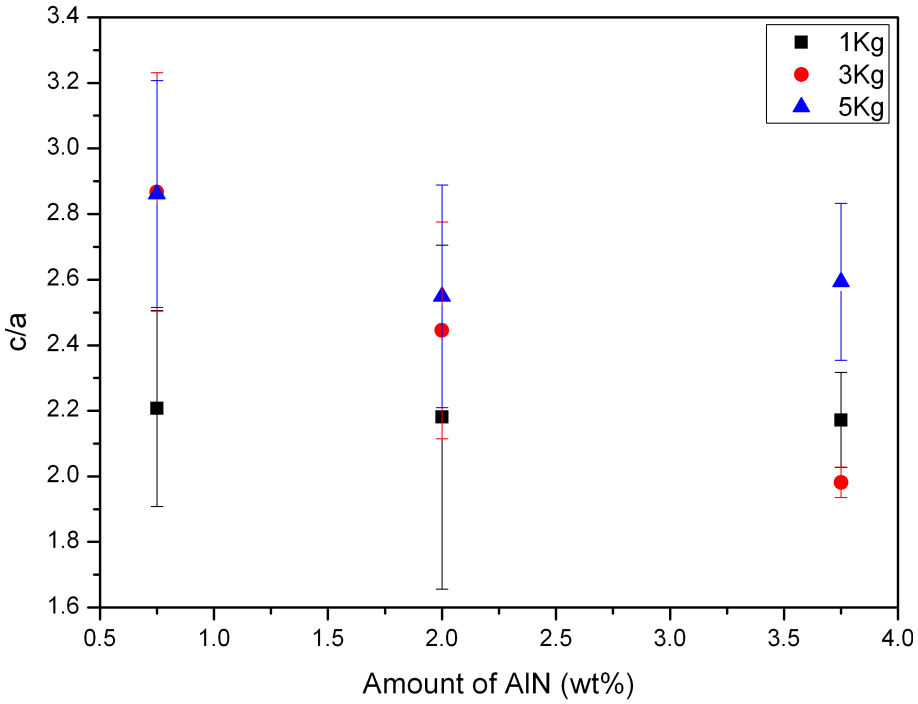


Figure 6.7.: Graph shows that there is little difference between the c/a ratios of these samples differing in the amount of AlN from 0.75 wt% to 3.75 wt%. All samples were sintered using SPS for 5 minutes.

agation significantly.

The effect of time spent at temperatures above 1850 °C on the c/a ratio was also found using the samples with the compositions of α-SiC with 3 wt% C and 3.75 wt% AlN. The fastest sintering schedule was the SPS followed by HP for 60 minutes and then the slowest was the sample that was dwelled at intermediate temperatures as described in table 3.3.

Figure 6.8 reveals that there is a slight increase in the c/a ratio which is a sign of reduction in toughness however the increase is within the measurement error range. This result suggests that the sintering

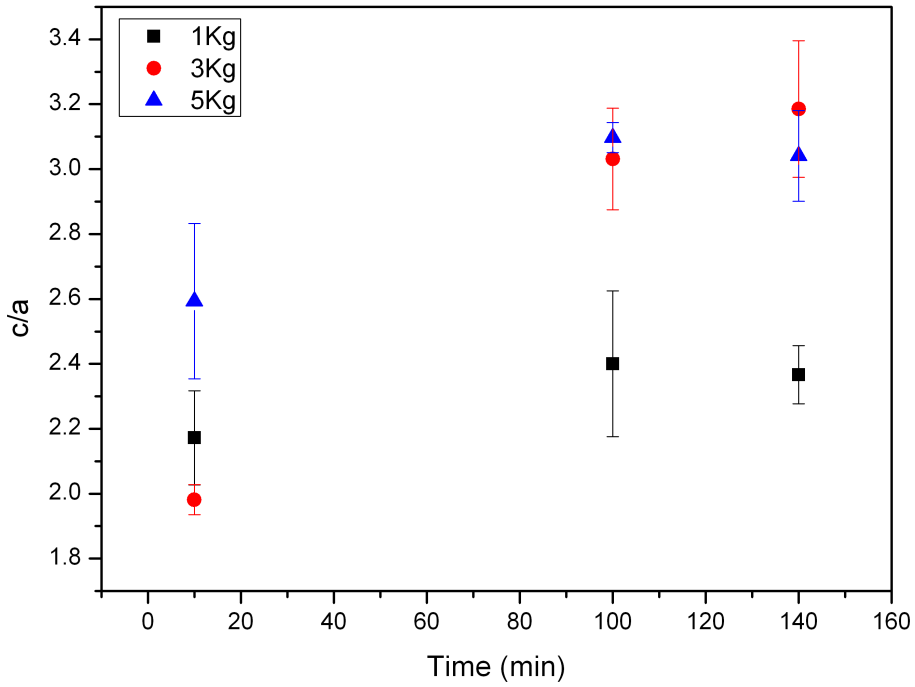


Figure 6.8.: Graph of c/a ratio as a function of time spent above 1800 °C during sintering showing a reduction in c/a ratio which translates into increased toughness with increase in time spent above 1800 °C. All samples had the composition of α-SiC + 3 wt% C and 3.75 wt% AlN.

schedules tried does not have significant influence on the cracking of SiC.

As can be seen in figure 6.9, the c/a ratio of the LPS sample is higher then the sample with no liquid phase, but again the differences are limited. Although LPS SiC has higher toughness, this is due to a careful balance between elongated grains, residual stress and grain boundary toughness and this particular LPS SiC sample does not have an elongated grain structure.

Analysing the cracking from indentation gives some idea about the fracture mode and possible toughening mechanisms. The fracture

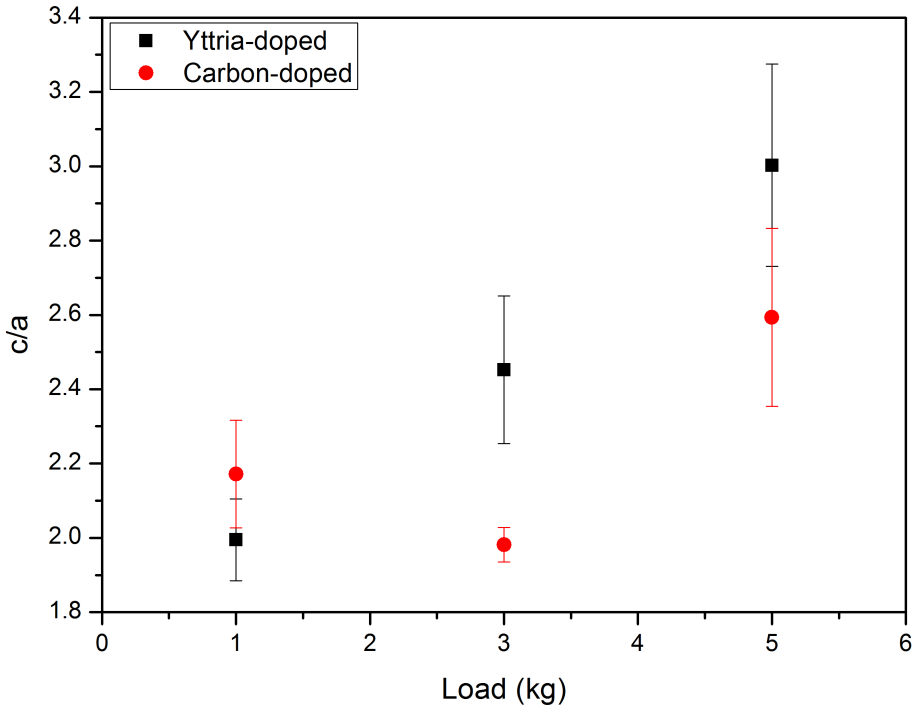
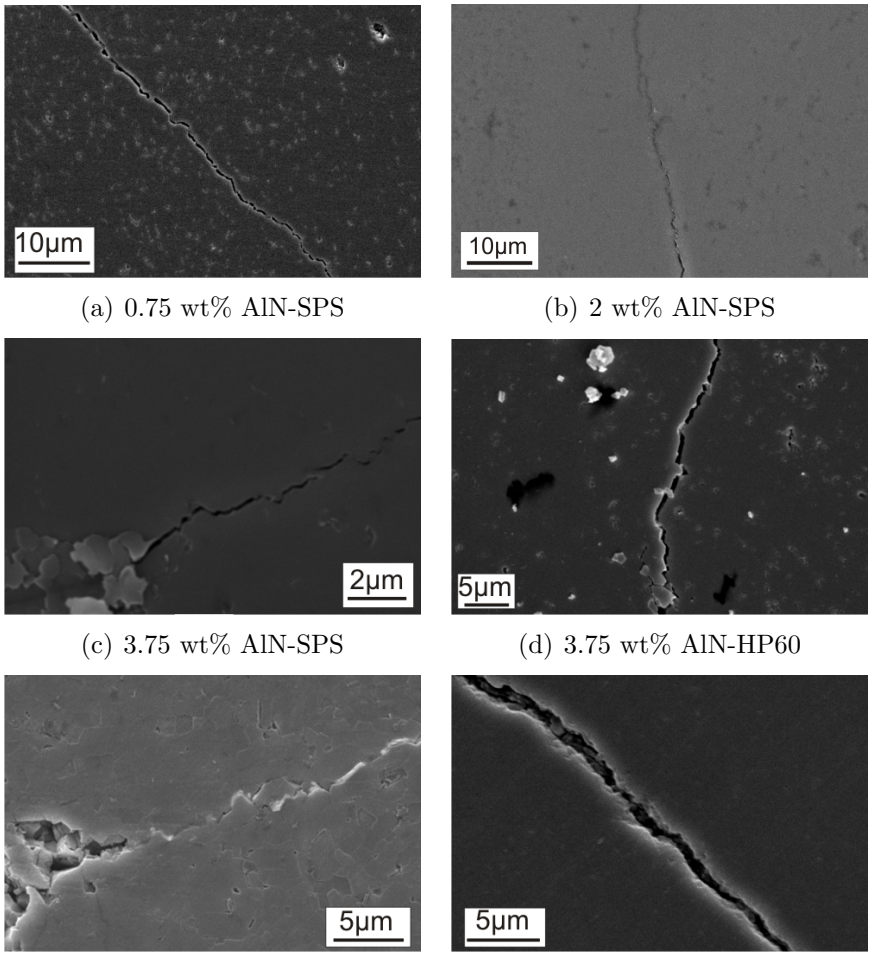


Figure 6.9.: Graph comparing c/a ratios of samples containing liquid phase or not.

mode in all the samples tested was intergranular. Crack bridging and deflection are possible toughening mechanisms as can be seen in figure 6.10. These mechanisms were present in almost all the samples tested.

However, the sample that did not contain any carbon showed very different cracking patterns. The crack lengths measured were short. However, this is not an indication of high toughness. The indent shown in figure 6.4 shows that in this sample, the material inside the indent gets crushed and densified and therefore there is no build-up of stress and no cracking. The reason for this behaviour is the coarse porosity. The pore size is bigger which leads to crumbling of the sample rather than cracking. The image of the sample in figure 6.4(b) shows what



(a) 0.75 wt% AlN-SPS (b) 2 wt% AlN-SPS

(c) 3.75 wt% AlN-SPS (d) 3.75 wt% AlN-HP60

(e) 3.75 wt% AlN-HP-Dwells (f) Yttria doped-1900 °C

Figure 6.10.: Cracks in various samples starting from the corners of indents. All cracks go around the grains.

an indent should look like for the cracking to be used as a measure of toughness. Hence the c/a ratio from the sample with no carbon was not regarded as meaningful.

It can be observed from the c/a ratios that none of these samples have very high toughness even though they all exhibit various toughening mechanisms including the intergranular cracking, crack deflection

and grain bridging. However, due to the fine grain size, the contributions of crack bridging and deflection is limited.

6.3. Effect of indentation cracking on hardness of SiC

It was noticed (figure 6.11) that increasing the load lead to a reduction in hardness and that higher loads increase the length of the cracks relative to the indent size. The shape of the graphs shows an almost constant hardness at very low loads in the nano-indentation region followed by a drop in hardness and perhaps more constant hardness at the higher loads.

It is argued that the hardness is a system property that depends on various other properties of the material and the indenter as mentioned earlier. The size of the indent depends on various factors. As mentioned earlier in the previous chapter, at small loads, the area of the indent depends on the plastic deformation of the sample. As the load is increased, the cracks start to appear near the corners of the indents. It is argued that these cracks lead to an increase in the size of the indents at large loads. The fact that the sharp drop in hardness in ceramics coincides with the start of the cracking supports this idea further.

Hardness is the ratio of applied load over the area of the indent.

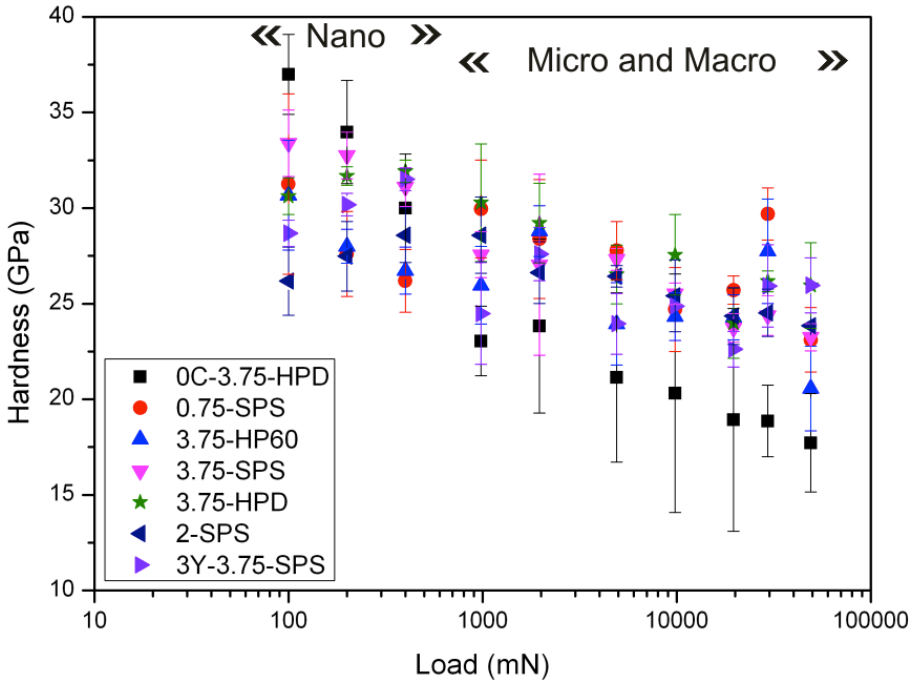


Figure 6.11.: Measured hardness of various samples plotted against load. For sintering schedule, please see table 3.3. All samples contained SiC. All samples except 0C-3.75-HPD contained 3 wt%C whereas C was replaced by yttria in 3Y-3.75-SPS sample.

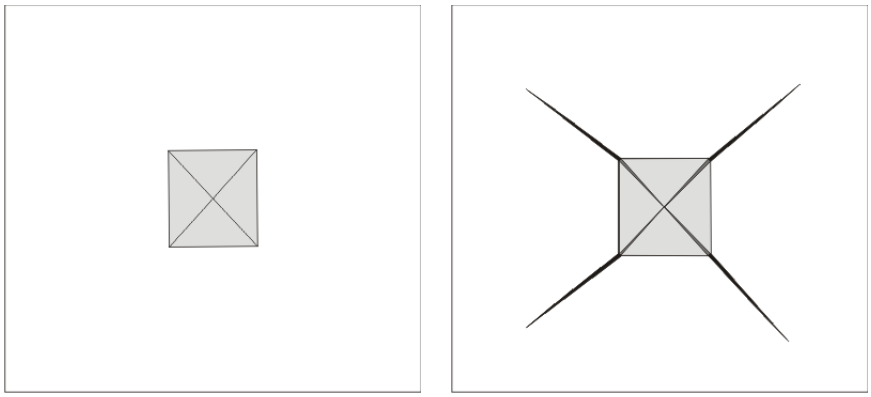
$$H = \frac{F}{A} \tag{6.4}$$

where H is hardness, F is the load applied and A is the area of the indent.

If it is assumed that the cracking leads to an increase in the area of the indent then, A from equation 6.4 can be split into two parts. A_o which is the area of the indent when there is no cracking and ΔA which is the increase in this area due cracking of the indent. Then the equation 6.4 can be written as follows:

$$H = \frac{F}{A_o + \Delta A} \tag{6.5}$$

The increase in area due to the cracking is illustrated in the schematic in figure 6.12



(a) No cracking (b) Cracking

Figure 6.12.: Schematic showing effect of cracking on the size of indent(a) No cracking on the indent corners (b) Cracking on the corners of indents.

It can be expected that ΔA is directly proportional to the applied load, F, and inversely proportional to the modulus of the material. It will also be a function of the crack lengths and the size of the indent, i.e. c/a ratio, which can be written as equation 6.6.

$$\Delta A = \psi \cdot f\left(\frac{c}{a}\right) \cdot \frac{F}{E} \tag{6.6}$$

where ψ is a constant.

Any crack which is smaller then the size of the indent will not lead to an increase in the size of an indent hence it will not have an effect on hardness. In other words, ΔA will be zero when the crack length

c, is smaller or equal to the size of the indent a, i.e. when c/a is equal to 1. A function that satisfies this criteria is the natural logarithmic function so therefore equation 6.6 can be rewritten as follows:

$$\Delta A = \psi \cdot ln\left(\frac{c}{a}\right) \cdot \frac{F}{E} \tag{6.7}$$

The hardness with no cracking, H_o can then be defined as given in equation 6.8.

$$H_o = \frac{F}{A_o} \tag{6.8}$$

From equation 6.8, the Area, A_o can be deduced as given in equation 6.9.

$$A_o = \frac{F}{H_o} \tag{6.9}$$

If, A_o is replaced by the expression in 6.9 and ΔA is replaced by the expression in equation 6.7 in equation 6.5 then the hardness is given as

$$H = \frac{F}{\frac{F}{H_o} + \psi \cdot ln\left(\frac{c}{a}\right) \cdot \frac{F}{E}} \tag{6.10}$$

Equation 6.10 can also be written as follows:

$$H = \frac{H_o}{1 + \psi \cdot ln\left(\frac{c}{a}\right) \cdot \frac{H_o}{E}} \tag{6.11}$$

Equation 6.11 suggests that the change in the hardness depends on

the c/a ratio alone and therefore does not appear to predict a load dependence for the hardness. However, the c/a ratio can be expressed in terms of the applied load. Dimensional analysis by Anstis et al.[77] shows that the applied load, fracture toughness, K_{1C}, and crack length must be related through:

$$K_{1C} = \chi \sqrt{\frac{E}{H}} \frac{F}{c^{3/2}} \tag{6.12}$$

Whereas the size of a Vickers indent is related to the applied load by

$$H = \frac{F}{2a^2} \tag{6.13}$$

If equation 6.12 is solved for c and equation 6.13 is solved for a then the following expression is obtained for c/a

$$\frac{c}{a} = \left[\chi^4 \frac{8 \cdot H \cdot E^2}{K_{1C}^4} \right]^{\frac{1}{6}} \cdot F^{\frac{1}{6}} \tag{6.14}$$

which shows that c/a will increase with load. If the c/a ratio in equation 6.14 is set to be 1, then the load applied will be the critical load above which the indent size will be affected by cracking. This critical load F_c, can be expressed as follows:

$$F_c = \left[\chi^4 \frac{8 \cdot H_o \cdot E^2}{K_{1C}^4} \right]^{-1} \tag{6.15}$$

So that

$$\frac{c}{a} = \left(\frac{F}{F_c}\right)^{\frac{1}{6}} \tag{6.16}$$

Substituting the c/a expression from equation 6.16 into equation 6.11, the hardness expression becomes as given in equation 6.17. However, for short cracks, i.e. at the lowest loads where cracking occurs, the constant of proportionality χ may be different consistent with the observation that indentation toughness values are only reliable in limited load regions. Therefore in practice, F_c might need to remain a fitting variable.

When

$F \leq F_c$ then $H = H_o$ $F \geq F_c$ then H is given in equation 6.17

$$H = \frac{H_o}{1 + \frac{\psi}{6} \cdot ln\left(\frac{F}{F_c}\right) \cdot \frac{H_o}{E}} \tag{6.17}$$

From this expression, the hardness without the effect of cracking at any load can be found if the critical load F_c and H_o are known. The critical load can be found from the c/a ratios using equation 6.16. Since all the samples had very similar hardness, fracture toughness and modulus, the data from all these samples was combined and analysed together. These samples included α-SiC with 0.75 wt.%AlN + 3 wt.%C, 2 wt.%AlN + 3 wt.%C, and 3.75 wt.%AlN + 3 wt.%C and yttria doped sample all SPS sintered as well as α-SiC + 3.75 wt.%AlN + 3 wt.%C Hot Pressed for 1 hour and Hot Pressed with intermediate dwells. The plot is given in figure 6.13.

The critical load is where both the lines on the graph intersect each

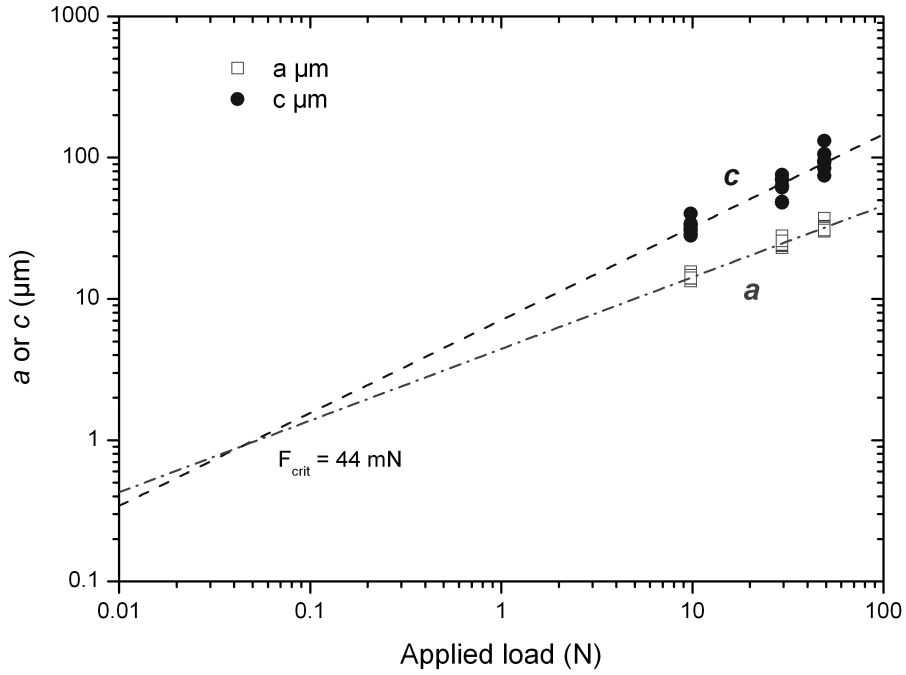


Figure 6.13.: Graph of Log of crack length and diagonal length of indent against the log of applied load for three different loads to measure the critical load F_{crit}.

other. This was found to be 44 mN.

The critical load can also be found from the Young's modulus, fracture toughness and hardness, H_0 using equation 6.15. The average of the Young's modulii for all the SiC samples when measured using nano-indentation method was used which was found to be 422 ± 62 GPa. H_0 was taken as 34.7 and fracture toughenss was calculated from indentation using Anstis's equation and the average fracture toughness was found to be 3.84 ± 0.9 MPa $m^{1/2}$. ψ was calculated by fitting the data using equation 6.12 and was found to be 5.3. The resulting critical load was found to be 67 mN.

The average of both critical loads was then used to fit the model

onto the hardness data for SiC which is given in figure 6.14. A power law fit is also given for comparison.

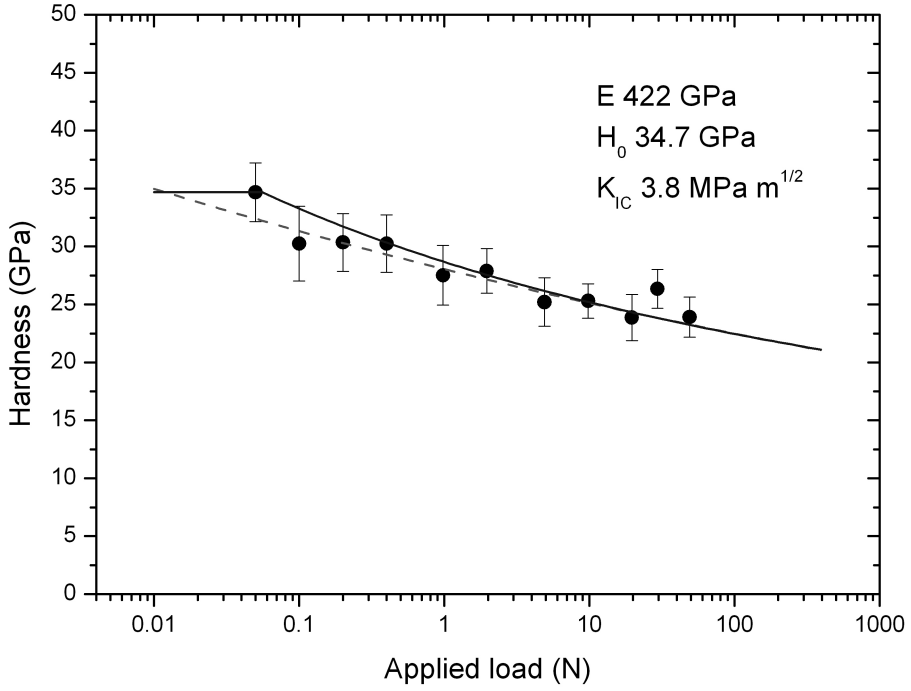


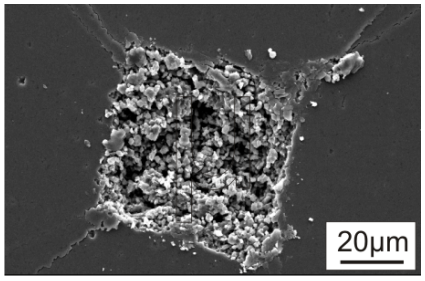
Figure 6.14.: Diagram showing the hardness data from SiC samples. The curve represents the model propsed in this study. The dotted line is the power law fit which is given for comparison.

Figure 6.14 reveals that the hardness drops with the load according to the expected power of the force, i.e. hardness does scale with c/a hence cracking is a viable explanation. It suggest that it is this cracking that is the cause of the drop in hardness rather then any other part of the microstructure. Although the microstructure does play a role in the indentation cracking. However, all these samples showed similar behaviour. This suggests that the amount of AlN in the samples did not have any impact on the hardness of SiC. The critical load found

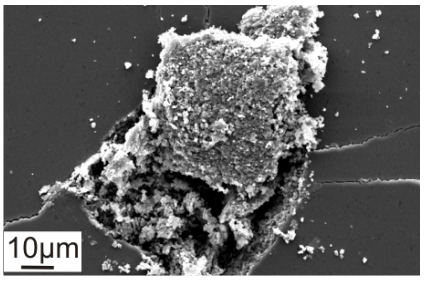
in this model is low. Cracks were not observed at such low loads. This is because perhaps due to the assumption that the crack lengths can be extrapolated back to small loads. Starting a crack is more energy consuming then propagating a crack. This is why no cracks were observed in the indents made using 200 mN load.

6.4. Comminuta ejection

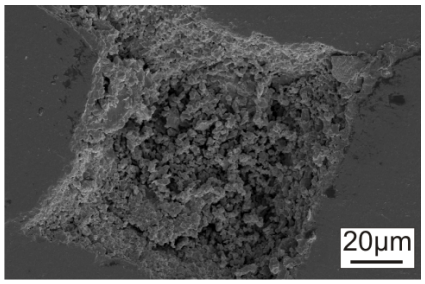
The indents made in the cracking regime showed a very interesting phenomenon. Upon unloading, the indents ejected the material from within the indent upwards in a dramatic manner. The inside of the indents made using 5 kg load showed the presence of individual grains separated from each other as can be seen in figure 6.15 whereas the area around the indent showed a lot of debris containing single grains from the material as can be seen in figure 6.16. These grains have been ejected from the inside of the indent after unloading and have landed back on the surface of the sample. It is to be noted that this effect is different from 'chipping; which is the ejection of lobes of material from the sides of the indent, which is more commonly observed. The ejection from the centre of the indent reported here was found in indents with and without chipping.



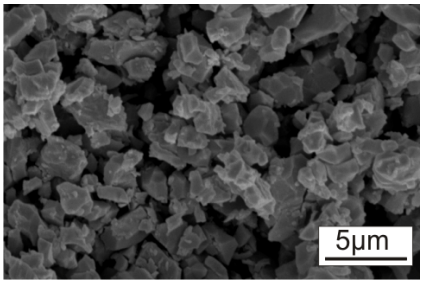
(a) SEM image of an indent that ejected comminuta



(b) SEM image of an indent that has a large piece debris fallen into it



(c) SEM image of another indent that ejected comminuta

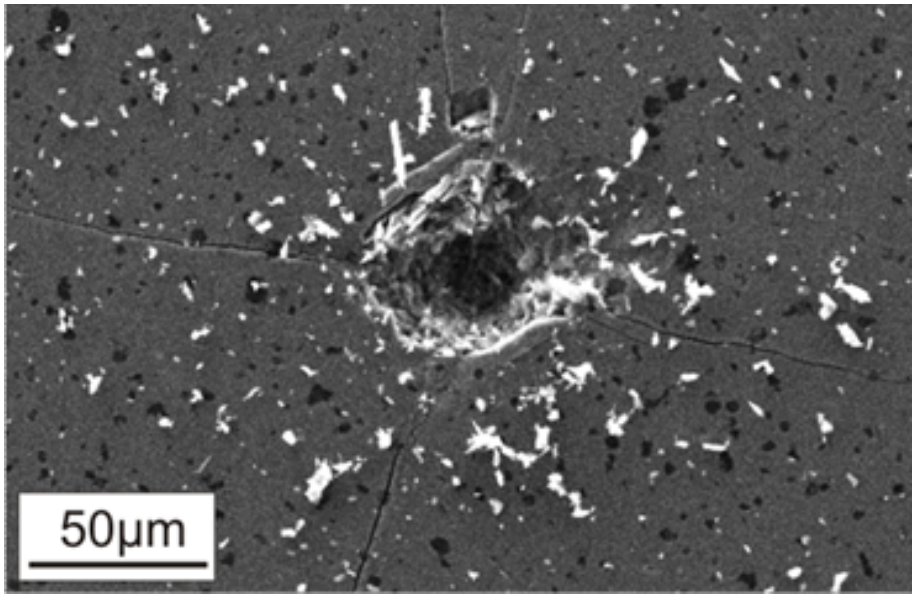


(d) A close up of inside of indent (c)

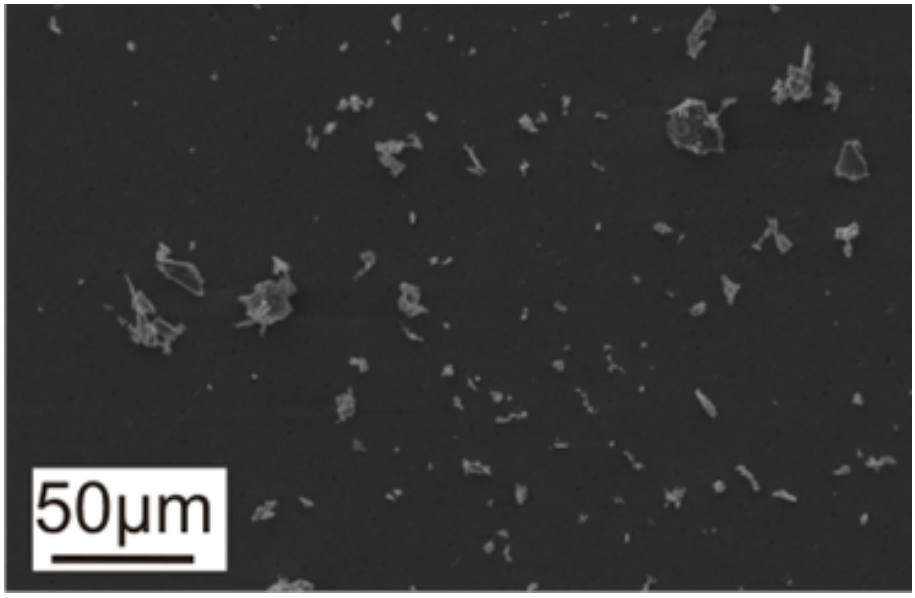
Figure 6.15.: (a), (b) and (c) shows SEI of inside indents that have ejected the comminuta after unloading whereas (d) is a close up of inside of indent shown in (c) The sample was SiC + 3 wt% C + 3.75 wt% AlN sintered using HP-D schedule (see table 3.3)

6.4.1. Effects of indentation load on comminuta ejection

A study of comminuta ejection with increasing indentation loads was carried out. 10 indents were made at each load using loads of 1 Kg (9.8 N), 3 Kg (29.4 N), 5 Kg (49 N), 10 Kg (98 N), 20 Kg (196 N) and 30 Kg (294 N). The indents were analysed in the SEM to see how many of the indents showed ejection. The results for SPS sintered samples of α-SiC with 3 wt% C and 2 wt% AlN are shown in figure 6.17. It



(a) SEM image of an indent with debris around it



(b) SEM image of the area near the indent showing debris suspected to result from comminuta ejection. Sample courtesy of Defence Science and Technologies Ltd. (DSTL)

Figure 6.16.: SEI of the indented surface of a sample with composition of SiC + 3 wt%C + 2 wt% AlN SPSed.

is clear that a larger fraction of indents show ejection as the load is increased. A critical load was arbitrarily defined as is the load at which 50% of indents have ejected. The critical load for this material is 23 N.

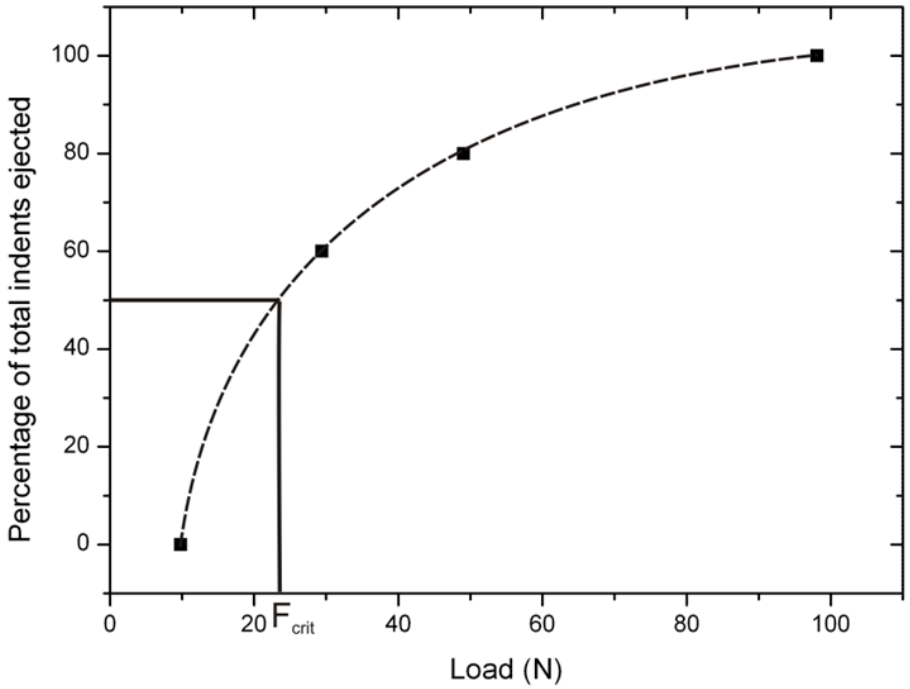


Figure 6.17.: Plot of indentation load vs % of indents with comminuta ejection behaviour for α-SiC with 2 wt% AlN and 3 wt%C SPSed sample. The critical load F_{crit} is defined as load at which 50% of total indents eject comminuta.

6.4.2. Effects of amount of AlN in α-SiC samples on critical load for comminuta ejection

SPSed samples of α-SiC with 3 wt% C and three different amounts of AlN (0.75, 2 and 3.75 wt%) were studied to determine the critical load of comminuta ejection. Increasing the amount of AlN leads to an increase in the critical load of comminuta ejection as can be seen in

figure 6.18.

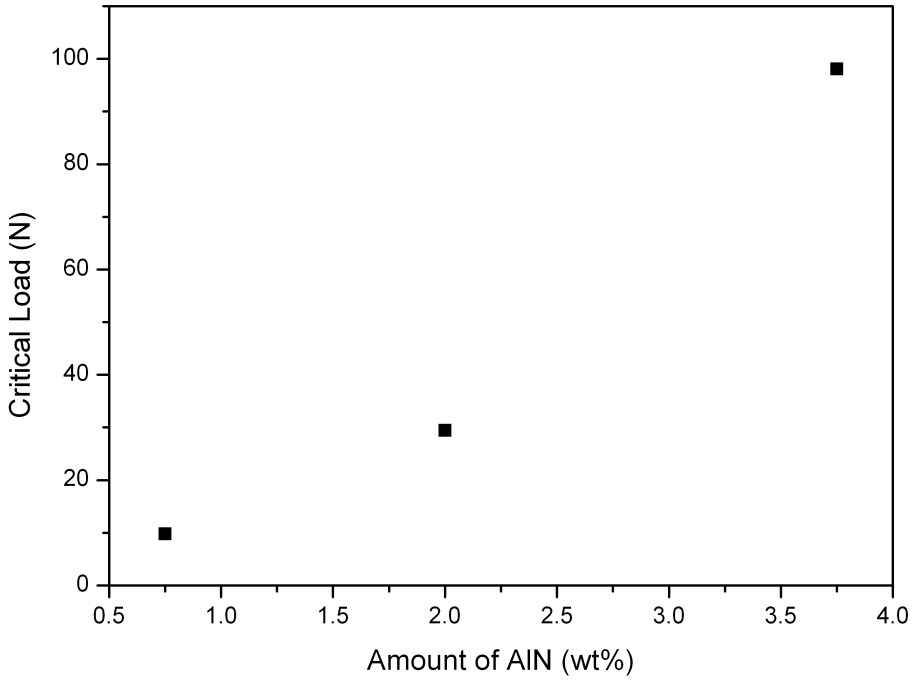


Figure 6.18.: Graph showing effects of amount of AlN on the sample's critical load of ejection in the samples SPSed at 2100 °C for 5 minutes. Increasing amount of AlN increases critical load of ejection.

The grain sizes and hardnesses of all these compositions are similar. As discussed in chapter 4, AlN in these materials is mostly found near the grain boundaries. Hence AlN affects the grain boundary chemistry and perhaps the strength of the grain boundary.

6.4.3. Mechanisms of comminuta ejection

SEI and observations during indentation suggest that the comminuta ejection can be separated into two parts. Firstly, the grains have to debond from each other and then secondly, they will have to eject out

of the indent.

Two processes can contribute to break-up into small grains. The first is the surface break up during the loading of the indenter whereas the second is the "de-bonding" of the grains from each other due to grain boundary cracking deep inside the bulk of the sample under the indenter tip.

The grains that come into contact with the indenter tip need to either 'flow/deform' with the indenter tip or 'roll' and move in order to accommodate the indenter tip's travel. This means they will have to break free from the adjoining grains as can be seen from the schematic given in figure 6.19. This leads to the fracturing of the grains at the grain boundaries. This leads to the break up of the surface of the sample and cracking. This is shown in figure 6.20.

In the next stage, the broken up surface grains get 'repacked' as the indenter travels further into the surface. This can be observed in figure 6.21 where the centre of the indent remains firm however, the edges of the indent show some break up. A few chips can also be seen.

During the loading period, the cracking of the grain boundaries slightly deeper into the surface of the sample also takes place in order to accommodate the indenter tip. This involves grain sliding and other cracking phenomena an illustrated in figure 6.22. The low magnification image shows the indent location. This indent was made using a Berkovich diamond indenter tip with 200mN load in the SPS sintered sample of α-SiC with 3 wt% C and 0.75 wt% AlN.

The high magnification image of the same site shows the cracking on

the grain boundaries as well as the grain sliding. Upon unloading, the elastically deformed material tries to recover and large stresses build up in the indent. After unloading, the residual stress field of material where the residual stress is broadly parallel to the surface. This is well known and drives the cracks parallel to the surface which gives rise to chipping (see also the work of Lawn and Wilshaw [68]). However, this stress field can also drive ejection from the centre. If the surface layer can withstand these stresses then the ejection does not happen however, if the compressive stresses are too large for this surface layer, which also consists of broken and repacked grains, to withstand it then the ejection takes place and the individual grains are 'thrown out' by these residual compressive stresses.

The same communita ejection effect has been observed by Ezra Feilden-Irving[157] in alumina when it was indented with Vickers indenter using 20 kg load. The images given in figure 6.23 which shows that the communita ejection phenomenon is not specific to SiC.

6.5. Conclusions

Macro indentation of SiC samples suggests that the amount of AlN does not have an effect on the hardness. The hardness of a sample with no carbon that had coarse grains (4 μm) was lower then the hardness of a fine grained sample. The time spent at the sintering temperature also had minimal effect on the hardness of SiC.

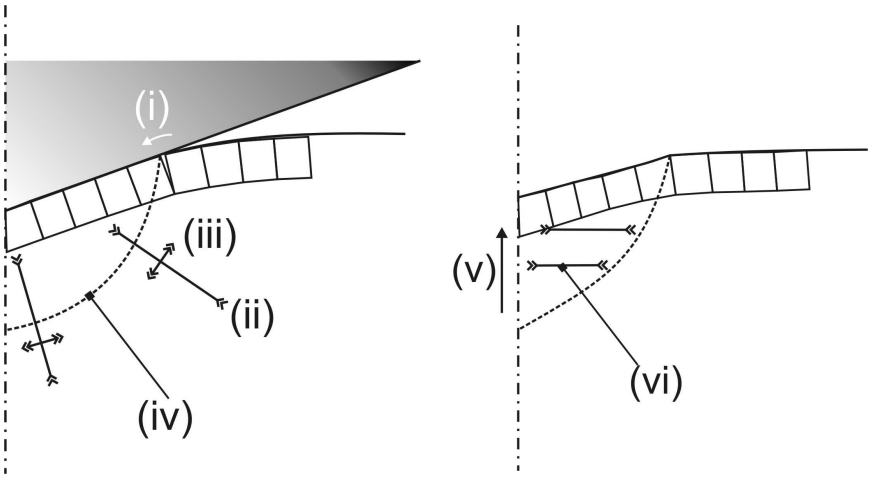
There were insignificant differences between all the samples apart

from the sample with no carbon. This sample showed extensive cracking inside the indent but only small cracks were detected coming out of the corners because of a change in deformation mechanism to densification. The sample containg liquid phase also showed similar behaviour suggesting that the liquid phase does not lead to an increase in the toughness. All samples showed intergranular cracking. Grain bridging and crack deflection are possible toughening mechanisms.

The drop in hardness with increasing load can be explained by the cracking of the indents. A model to calculate the effects of cracking on hardness has been developed. The variation of hardness with load was consistent with it but further work is needed to verify some of the underlying assumptions.

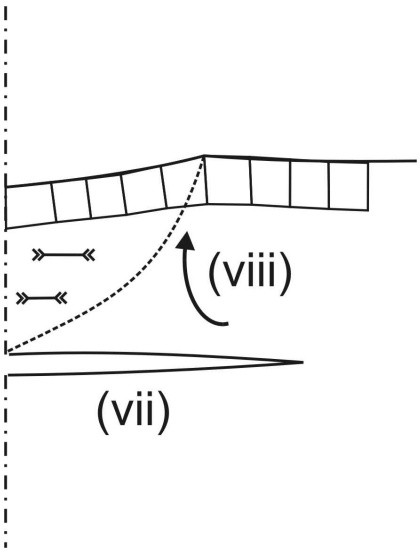
A new observation made was the ejection of comminuta after the unloading of the indenter tip in Vickers indentation. It was found that the critical load which is defined to be the load of indentation at which 50% or more of the total indents eject comminuta, increases with increasing amount of AlN in the SiC.

A possible mechanism proposed for this phenomenon is the breaking up of grains through grain boundary micro cracking during the loading of the indenter before re-packaging under the load. The residual stresses push these broken grains out of the indent upon unloading of the indenter tip. The critical load might therefore depend on the grain boundary toughening.



(a) The indenter moving into the sample with tensile stresses on the grain boundaries near the plastic zone and on the surface

(b) Indenter travels further with compressive stresses inside the plastic zone



(c) Cracking and the residual stress build-up inside the indent pushing the material outwards.

Figure 6.19.: (a) The indenter moving into the sample with tensile stresses on the grain boundaries near the plastic zone and on the surface (b) Indenter travels further with compressive stresses inside the plastic zone. (a) whereas (c) Cracking and the residual stress build-up inside the indent pushing the material outwards.

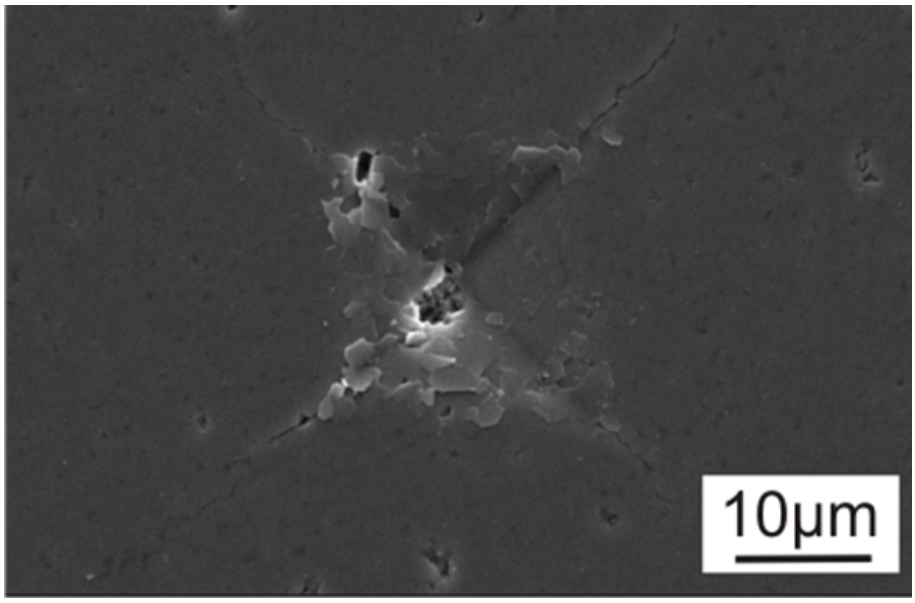


Figure 6.20.: Image showing the indent made in α-SiC with 3 wt%C and 2 wt%AlN SPSed sample using 49 N load. Surface cracking can be seen.

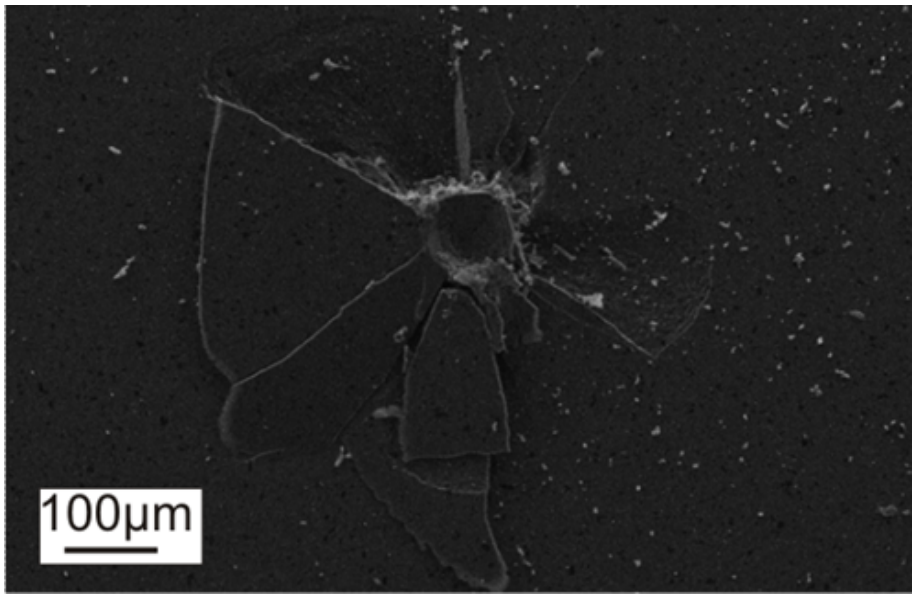
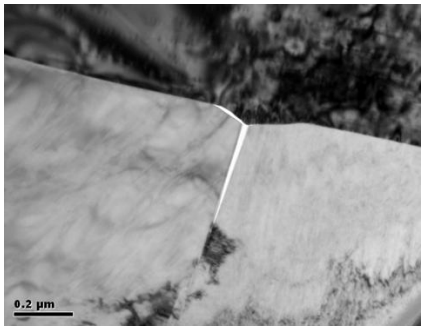


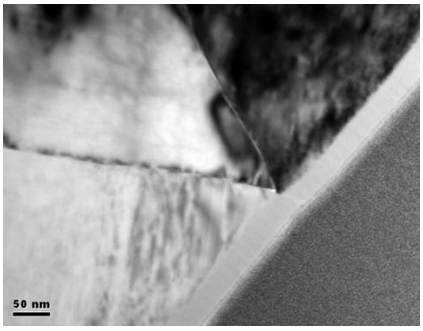
Figure 6.21.: Image showing the indent made in α-SiC with 3 wt% C and 2 wt% AlN SPSed sample using 294 N load. Although it has chipped but the centre of the indent is firm with no ejection.



(a) BF-TEM image of area under the indent



(b) Cracking under the indent



(c) Grain sliding

Figure 6.22.: (a)Low magnification TEM image under the indent made using Berkovich indenter and 200 mN load in an SPSed sample with composition of SiC + 3 wt% C + 0.75 wt% AlN, (b) shows a close up of the crack in (a) whereas (c) shows the grain sliding

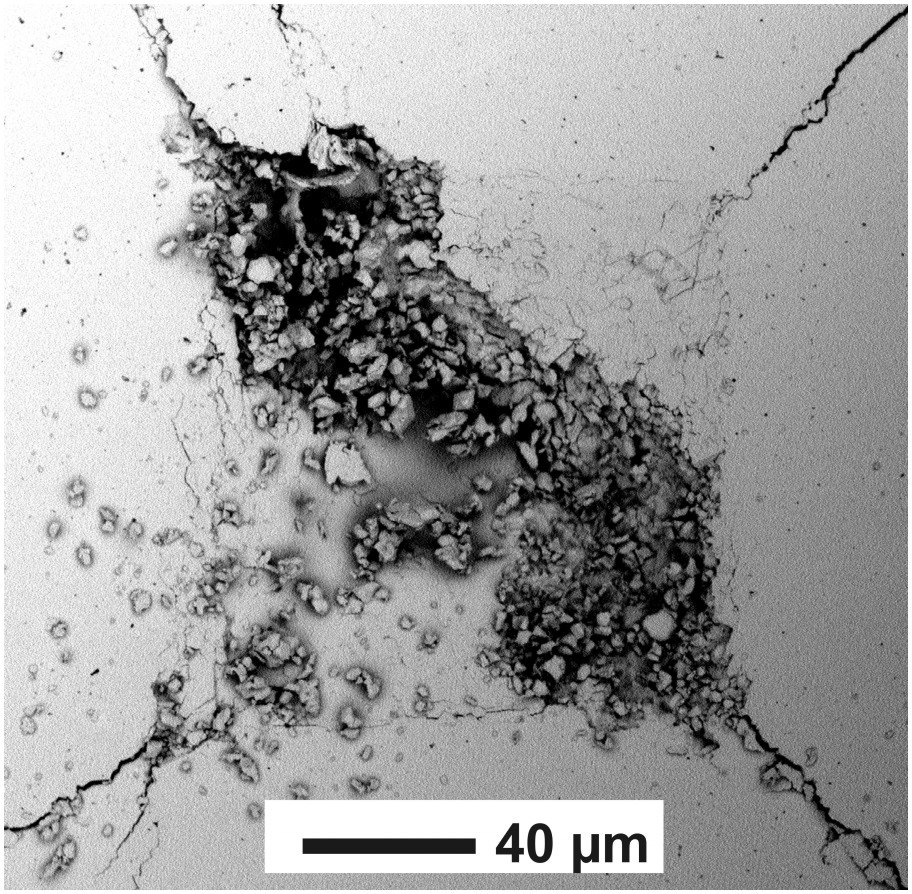


Figure 6.23.: SEM image of an indent made in alumina showing evidence of communita ejection. Image taken from Ezra Feilden-Irving [157]

7. Conclusions and further work

7.1. Conclusions

Silicon carbide was sintered using carbon, yttria and AlN as sintering additives in various amounts. Fast SPS and HP were used to densify the SiC. It was found that carbon alone is insufficient to sinter SiC using HP. However, AlN as a single additive was able to densify SiC. It was confirmed that carbon restricts the grain growth whereas increasing the AlN amount from 0.75 wt% to 3.75 wt% decreased the grain size by 1 μm from 2.5 μm to 1.5 μm. The sample with only AlN as sintering additive had very coarse microstructure (grain diameter of around 6 μm) suggesting that carbon is more effective in limiting the grain size. It was also observed that the time spent at high temperature (above 1800 °C) was the main factor that determined the polytype transformation from 6H to 4H. However, a sample accidentally sintered with an unknown amount of carbon (less then 3 wt.%) showed a remarkable polytype transformation along with the elongated

grain structure suggesting that perhaps carbon can dramatically effect the polytype and microstructure.

No liquid phase was present in the SiC sample containing AlN and carbon whereas the sample containing AlN and yttria showed the presence of liquid phase. No bulk liquid phase was observed in the sample that only contained AlN however, the presence of a very thin liquid film on the grain boundaries cannot be ruled out. Hence the formation of liquid during sintering of AlN doped SiC depends on the whole system of additives rather then just AlN.

Indentation of SiC samples revealed that the hardness response of SiC changes with load. At nano-indentation scale (load up to 400 mN) where there is no cracking, deformation is simply controlled by the plasticity parameters of the SiC lattice, at least near room temperature. The Peierls stress was found to be 12 ± 1 GPa and the activation energy for dislocation flow was found to be 1.1 ± 0.3 eV. These parameters were measured using simple nano-indentation experiments and were in reasonably good agreement with literature values obtained by high temperature compression testing. Hardness is not a function of load in this region nor did the grain size have an impact on the nano-hardness of SiC. As the applied load increased, cracks started to appear from the corners of the indents. With the onset of cracking, the hardness of the material dropped with load.

c/a ratios were measured to get an estimate of toughness. It was found that the grain size did not have an effect on toughness. The cracking pattern was similar for all the samples showing intergranular

cracking, crack bridging as well as grain pull out. However, the sample with no carbon that had coarse grains (grain diameter of around 6 μm) showed a very different cracking mechanism. There were very small cracks near the corners of the indents however crushing was observed inside the indent suggesting that perhaps this crushing was responsible for the lack of cracking from the corners. Samples sintered using LPS could perhaps have been expected to show some toughening behaviour arising from the presence of liquid phase on grain boundaries as reported in literature. However, the samples in this study were found to be very brittle. However the grains were still very small and hence crack deflection and grain pull-out can only raise the fracture energy by a limited amount.

A new observation made is the ejection of communita from the Vickers indents after unloading in AlN doped SiC. The same effect was also observed in a pressureless sintered alumina sample. The fraction of total indents ejecting communita increased with a reduction in the amount of AlN in SiC. It is proposed that this effect depends on the grain size and grain boundary toughness of the material.

7.2. Further work

It was shown in this thesis that AlN does not affect the microstructure greatly however, the role of carbon is yet to be determined. Some evidence points towards an impact of carbon content on the grain size. However, the contribution of sintering schedule to the polytype trans-

formation is yet to be determined. There is a need to study the effect of carbon and the sintering schedules on the microstructure and the subsequent effect on the mechanical properties.

The AlN distribution in the SiC has been studied. However; further HRTEM work is needed to clarify further whether liquid might play a role in densifying this type of SiC.

It has been demonstrated that the nano-indentation can be used to determine the parameters of plasticity near room temperature. Identification of slip planes in the TEM could further help in understanding of these parameters. It has been concluded that the grain boundaries are not the controlling factor in plastic deformation when the size of indent is smaller then the grain size. However, the size at which they become important could be found by experiments using very small grains.

The macro-hardness testing showed that hardness depends on the applied load. The model proposed to separate the effect of cracking on hardness needs to be developed further with some underlying assumptions to be verified. A 3D finite element analysis could be used to determine the effect of crack opening on indenter penetration further.

Finally, the communita ejection behaviour observed needs to be linked to other mechanical properties. It is expected to be a function of grain boundary toughness, grain size, morphology and plasticity. Effect of shape of indenter tip and sample surface condition could also be important parameters.

Elongated grains are believed to improve the toughness whereas, it

was believed that fine grained microstructure of SiC produces harder ceramic. This study suggests that the nano-hardness at room temperature is independent of the grain size. An elongated grained SiC sample responded in the same manner as a finer equiaxed microstructured sample of SiC. This paves the way to produce hard and tough SiC.

References

[1] Swab, J. Recommendations for determining the hardness of armor ceramics. *International Journal of Applied Ceramic Technology*, 1(3):219–225, 2004.

[2] Rainforth, W. M. The wear behaviour of oxide ceramics- A review. *Journal of Materials Science*, 39(22):6705–6721, 2004.

[3] Shapiro, I. P. Todd, R. I. Titchmarsh, J. M. and Roberts, S. G. An indentation model for erosive wear in Al_2O_3/SiC nanocomposites. *Journal of the European Ceramic Society*, 31:85–95, 2011.

[4] Page, T. F. *The Physics and Chemistry of Carbide, Nitrides and Borides.* Kluwer Academic Publishers, Norwell, MA, U.S.A., 1990.

[5] Ramsdell, L. S. The crystal structure of α-SiC, type 4. pages 431–442, 1944.

[6] Umeno, Y. Kinoshita, Y. and Kitamura, T. Ab initio DFT study of ideal shear strength of polytypes of silicon carbide. *Strength of Materials*, 40(1):8–13, January-February 2008.

[7] Zangvil, A. and Ruh, R. *Journal of the American Ceramic Society*, 71(10):884–890, 1988.

[8] Prochazka, S. and Charles, R. J. Strength of Boron-Doped, Hot-Pressed Silicon Carbide. *Ceramic Bulletin*, 52(12):885–891, 1973.

[9] Prochazka, S. The Role of Boron and Carbon in Sintering of Silicon Carbide. *Special Ceramics 6*, pages 171–181, 1975.

[10] Gu, H. Shinoda, Y. and Wakai, F. *Journal of the American Ceramic Society*, 82(2):469–472, February 1999.

[11] van Rijswijk, W. and Shanefield, D. J. Effects of Carbon as a Sintering Aid in Silicon Carbide. *Journal of the American Ceramic Society*, 73(1):148–149, 1990.

[12] Friederich, K. M. and Coble, K. L. Influence of Boron on Chemical Interdiffusion in SiC During Conversion of Silicon Fibers to SiC. *Journal of the American Ceramic Society*, 66(8):C–141–C–142, 1983.

[13] Stobierski, L. and Gubernat, A. Sintering of silicon carbide II. Effect of boron. *Ceramics international*, 29(4):355–361, 2003.

[14] Clegg, W. J. Role of Carbon in the Sintering of Boron doped Silicon Carbide. *Journal of the American Ceramic Society*, 83(5):1039–1043, May 2000.

[15] Maitre, A. Put, A. Laval, J. Valette, S. and Trolliard, G. Role of boron on the Spark Plasma Sintering of an α-SiC powder. *Journal of the European Ceramic Society*, 28(9):1881–1890, 2008.

[16] Ermer, E. Wieslsaw, P. and Ludoslaw, S. Influence of sintering activators on structure of silicon carbide. *Solid state ionics*, 141-142:523–528, 2001.

[17] Quanli, J. Haijun, Z. Suping, L. and Xiaolin, J. Effect of particle size on oxidation of silicon carbide powders. *Ceramics international*, 33(2):309–313, March 2007.

[18] Rczka, M. Górny, G. Stobierski, L. and Rozniatowski, K. Effect of carbon content on the microstructure and properties of silicon carbide-based sinters. *Materials Characterization*, 46:245–249, 2001.

[19] Ziccardi, C. and Haber, R. Addition of Excess Carbon to SiC to Study its Effect on Silicon Carbide (SiC) Armor. In Prokurat, L and Wereszczak, A and Lara-Curzio, E, editor, *Advances in Ceramic Armor II: Ceramic Engineering and Science Proceedings*, volume 27, pages 97–103. John Wiley & Sons, Inc., 2008.

[20] Hecht, N. L. McCullum, D. E. and Graves, G. A. Investigation of Selected Silicon Nitride and Silicon Carbide Ceramics. *Ceramic Engineering Science Proceedings*, 9:1313–1332, 1988.

[21] Chantikul, P. Anstis, G. R. and Lawn, B. R. A critical evaluation of indentation techniques for measuring fracture toughness: II, strength method. *Journal of the American Ceramic Society*, 64(9):539–543, September 1981.

[22] Cao, J. J. MoberlyChan, W. J. De Jonghe, L. C. Gilbert, C. J. and Ritchie, R. O. In Situ Toughened Silicon Carbide with Al-B-C Additions. *Journal of the American Ceramic Society*, 79(2):461–469, May 1996.

[23] Zhang, X. F. Yang, Q. and De Jonghe, L. C. Microstructure development in hot-pressed silicon carbide: effects of aluminum, boron, and carbon additives. *Acta Materialia*, 51(13):3849–3860, 2003.

[24] Pabit, E. L. *Grain boundary and triple junction chemistry of silicon carbide sintered with minimum additives for armor applications*. PhD thesis, University of Florida, 2005.

[25] Ray, D. Flinders, M. Anderson, A. and Cutler R. A. Hardness/Toughness Relationship for SiC Armor. In Kriven, W. M. and Lin, H. T., editor, *27th Annual Cocoa Beach Conference on Advanced Ceramics and Composites: A: Ceramic Engineering*

and Science Proceedings, volume 24. John Wiley & Sons, Inc., 2008.

[26] Pabit, E. Siebein, K. Butt, D. P. Heinrich, H. Ray, D. Kaur, S. Flinders, R. M. and Cutler, R. A. *Grain Boundary Chemistry of SiC-Based Armor*, pages 69–84. John Wiley & Sons, Inc., 2008.

[27] Zenotchkine, M. Shuba, R. and Chen, I-W. Effect of Seeding on the Microstructure and Mechanical Properties of α-SiAlON: III, Comparison of Modifying Cations. *Journal of the American Ceramic Society*, 86(7):1168–1175, 2003.

[28] L.L. Qian, J. Daemen and Y. Zhao. Hardness and fracture toughness of moissanite. *Diamond and Related Materials*, 14:1669–1672, 2005.

[29] Kim, D-H and Kim, C. H. Toughening behavior of silicon carbide with additions of yttria and alumina. *Journal of the American Ceramic Society*, 73(5):1431–1434, May 1990.

[30] Chen, Z. Effects of Gadolinia and Alumina Addition on the Densification and Toughening of Silicon Carbide. *Journal of the American Ceramic Society*, 79(2):530–532, 1996.

[31] Omori, M. and Takei, H. Pressureless sintering of SiC. *Communications of the American Ceramic Society*, 65(6):C–92, June 1982.

[32] Liu, D-M and Fu, C-T. Effect of residual porosity and pore structure on the mechanical strength of SiC Al_2O_3 Y_2O_3. *Ceramics International*, 22(3):229 – 232, 1996.

[33] Falk, L. K. L. Microstructural development during liquid phase sintering of silicon carbide ceramics. *Journal of the European Ceramic Society*, 17(8):983–994, 1997.

[34] Ihle, J. Herrmann, M. and Adler, J. Phase formation in porous liquid phase sintered silicon carbide: Part I: Interaction between Al_2O_3 and SiC. *Journal of the European Ceramic Society*, 25(7):987 – 995, 2005.

[35] Lee, S. K. and Kim, C. H. Effects of α-SiC versus β-SiC Starting Powders on Microstructure and Fracture Toughness of Sic Sintered with Al_2O_3-Y_2O_3 Additives. *Journal of the American Ceramic Society*, 77(6):1655–1658, 1994.

[36] Gomez, E. Echeberria, J. Iturriza, I. and Castro, F. Liquid phase sintering of SiC with additions of Y_2O_3, Al_2O_3 and SiO_2. *Journal of the European Ceramic Society*, 24(9):2895 – 2903, 2004.

[37] Ihle, J. Herrmann, M. and Adler, J. Phase formation in porous liquid phase sintered silicon carbide: Part 2: Interaction between Y_2O_3 and SiC. *Journal of the European Ceramic Society*, 25(7):997–1003, may 2005.

[38] Strecker, K. Ribeiro, S. Camargo, D. Silva, R. Vieira, J. and Oliveira, F. Liquid phase sintering of silicon carbide with

AlN/Y_2O_3, Al_2O_3/Y_2O_3 and SiO_2/Y_2O_3 additions. *Materials Research*, 2(4):249–254, 1999.

[39] Ruh, R. and Zangvil, A. *Journal of the American Ceramic Society*, 65(5):260–265, May 1982.

[40] Chia, K. Y. and Storm, R. S. Silicon carbide bodies having high toughness and fracture resistance and method of making same. US Patent No. 5298470, March 1994.

[41] Rixecker, G. Wiedmann, I. Rosinus, A. and Aldinger, F. High-temperature effects in the fracture mechanical behaviour of silicon carbide liquid-phase sintered with AlN-Y_2O_3 additives. *Journal of the European Ceramic Society*, 21(8):1013 – 1019, 2001.

[42] Pan, Y. Tan, S. Jiang, D. Qiu, J. Kawagoe, M. and Morita, M. In-Situ Characterization of SiC-AlN multiphase ceramics. *Journal of Materials Science*, 34:5357–5360, 1999.

[43] Tian, Q. and Virkar, A. V. Interdiffusion in SiC-AlN and AlN-Al_2OC systems. *Journal of the American Ceramic Society*, 79(8):2168–2174, August 1996.

[44] Lee, J. K. Tanaka, H. and Kim, H. Formation of solid solutions between SiC and AlN during liquid-phase sintering. *Materials Letters*, 29:1–6, 1996.

[45] Rafaniello, W. Cho, K. and Virkar, A. V. Fabrication and char-

acterization of SiC-AIN alloys. *Journal of Materials Science*, 16:3479–3488, 1981.

[46] Li, J-F and Watanabe, R. Preparation and mechanical properties of SiC-AlN ceramic alloy. *Journal of Materials Science*, 26:4813–4817, 1991.

[47] Ray, D. A. Kaur, S. Cutler, R. A. and Shetty, D. K. Effect of Additives on the Activation Energy for Sintering of Silicon Carbide. *Journal of the American Ceramic Society*, 91(4):1135–1140, April 2008.

[48] Hilmas, G. E. and Tien, T-Y. Effect of AlN and Al_2O_3 additions on the phase relations and morphology of SiC Part 2: Microstructural observations. *Journal of Materials Science*, 34:5613–5621, 1999.

[49] Balog, M. Sajgalik, P. Hnatko, M. Lences, Z. Monteverde, F. Keckes, J. and Huang, J. L. Nano- versus macro-hardness of liquid phase sintered SiC. *Journal of the European Ceramic Society*, 25(4):529 – 534, 2005.

[50] Sigl, L. S. and Kleebe, H-J. Core/Rim Structure of Liquid-Phase-Sintered Silicon Carbide. *Journal of the American Ceramic Society*, 76(3):773–776, 1993.

[51] Hilmas, G. E. and Tien, T-Y. Effect of AlN and Al_2O_3 additions on the phase relations and morphology of SiC. Part 1: Composi-

tion and properties. *Journal of materials research*, 34:5605–5612, 1999.

[52] Huang, Z. H. Jia, D. C. and Zhou, Y. Effect of a new additive on mechanical properties of hot-pressed silicon carbide ceramics. *Materials Research Bulletin*, 37(5):933–940, April 2002.

[53] Wereszczak, A. A. Lin, H-T and Gilde, G. A. The effect of grain growth on hardness in hot-pressed silicon carbides. *Journal of Materials Science*, 41(15):4996–5000, May 2006.

[54] Takeshi A Yamamoto, Takayuki Kondou, Yasuhiro Kodera, Takashi Ishii, Manshi Ohyanagi, and Zuhair A Munir. Mechanical Properties of -SiC Fabricated by Spark Plasma Sintering. *Journal of Materials Engineering and Performance*, 14(4):460–466, aug 2005.

[55] K. Toriyama M. Zhou, Y. Hirao and H. Tanaka. Very rapid, densification of nanometer silicon carbide powder by pulse electric current sintering. *Journal of the American Ceramic Society*, 83(3):654–656, March 2000.

[56] Munir, Z. Anselmi-Tamburini, U. and Ohyanagi, M. The effect of electric field and pressure on the synthesis and consolidation of materials: A review of the spark plasma sintering method. *Journal of Materials Science*, 41:763–777, 2006.

[57] Snyder, A. Quach, D. Groza, J. R. Fisher, T. Hodson, S. and Stanciu, L. A. Spark Plasma Sintering of ZrB_2-SiC-ZrC ultra-

high temperature ceramics at 1800 °C. *Materials Science and Engineering A*, 528(18):6079–6082, July 2011.

[58] Lee, S-H. Tanaka, H. and Kagawa, Y. Spark plasma sintering and pressureless sintering of SiC using aluminum borocarbide additives. *Journal of the European Ceramic Society*, 29(10):2087 – 2095, July 2009.

[59] G. Molenat, L. Durand, J. Galy, and A. Couret. Temperature control in spark plasma sintering: An FEM approach. *Journal of Metallurgy*, 2010, January 2010.

[60] W. Yucheng, F. Zhengyi. Study of temperature field in spark plasma sintering. *Materials Science and Engineering B*, 90(1-7):34–37, March 2002.

[61] D. Tiwari, B. Basu and K. Biswas. Simulation of thermal and electric field evolution during spark plasma sintering. *Ceramics international*, 35(2):699–708, March 2009.

[62] S. Grasso, Y. Sakka, and G. Maizza. Pressure effects on temperature distribution during spark plasma sintering with graphite sample. *Materials Transactions*, 50(8):2111–2114, 2009.

[63] Tabor, D. The physical meaning of indentation and scratch hardness. *British Journal of Applied Physics*, 7(5):159–166, May 1956.

[64] Zhang, J and Sakai, M. Geometrical effect of pyramidal indenters

on the elastoplastic contact behaviors of ceramics and metals. *Materials Science and Engineering A*, 381(1-2):62–70, sep 2004.

[65] Sakharova, NA and Fernandes, JV and Antunes, JM and Oliveira, MC. Comparison between Berkovich, Vickers and conical indentation tests: A three-dimensional numerical simulation study. *International Journal of Solids and Structures*, 46(5):1095–1104, March 2009.

[66] Fischer-Cripps, A. C. *Introduction to Contact Mechanics*. Springer-Verlag, New York, Inc., 2000.

[67] Knoop, F. Peters, C. G. and Emerson, W. B. A surface pyramidal-diamond tool for indentation measurements. *National Bureau of standards, U.S. Dept. of Commerce*, pages 211–240, 1939.

[68] Lawn, B and Wilshaw R. Review Indentation fracture: principles and applications. *Journal of Materials Science*, 10:1049–1081, 1975.

[69] Oliver, W. C. and Pharr G. M. An improved technique for determining hardness and elastic modulus using load and displacement sensing indentation experiments. *Journal of Materials Research*, 7(6):1564–1582, 1992.

[70] Hagan, J. T. and Swain, M. V. The origin of median and lateral cracks around plastic indentes in brittle materials. *Journal of Physics D-Applied Physics*, 11(15):2091–2102, October 1978.

[71] Vandeperre, L. J. Giuliani, F. Lloyd, S. J. and Clegg, W. J. The hardness of silicon and germanium. *Acta Materialia*, 55(18):6307 – 6315, 2007.

[72] Domnich, V. Gogotsi, Y. and Trenary, M. Identification of Pressure-Induced Phase Transformations Using Nanoindentation. In *MRS Fall Meeting*, volume 649 Symposium Q-Fundamentals of Nanoindentation and Nanotribology 2. Cambridge University Press, 2000.

[73] Mann, A. B. van Heerden, D. Pethica, J. B. Bowes, P. and Weihs, T. P. Contact resistance and phase transformations during nanoindentation of silicon. In *Philosophical Magazine A*, volume Physics of Condensed Matter Structure Defects and Mechanical Properties, pages 1921–1929, 2002.

[74] Mann, A. B. and van Heerden, D. Size-dependent phase transformations during point loading of silicon. *Journal of Materials Research*, 15(8):1754–1758, 2000.

[75] Suzuki, K. Benino, Y. Fujiwara, T. and Komatsu, T. Densification energy during nanoindentation of silica glass. *Journal of the American Ceramic Society*, 85(12):3102–3104, 2002.

[76] Tancret, F. and Osterstock, F. Indentation behaviour of porous materials: application to the Vickers indentation cracking of ceramics. *Philosophical Magazine*, 83(1):125–136, 2003.

[77] Anstis, G. R. Chantikul, P. and Lawn, B. R. A critical evaluation of indentation techniques for measuring fracture toughness: I, direct crack measurements. *Journal of the American Ceramic Society*, 64(9):533–538, 1981.

[78] Warren, P. D. Fracture of brittle materials: effects of test method and threshold stress on the Weibull modulus. *Journal of the European Ceramic Society*, 21(3):335–342, 2001.

[79] Marsh, D. M. Plastic flow in glass. In *Proc. R. Soc. A*, volume 279, pages 420–435, 1963.

[80] Johnson, K. L. The correlation of indentation experiments. *Journal of the Mechanics and Physics of Solids*, 18:115–126, 1970.

[81] Cheng, Y-T and Cheng C-M. Can stress–strain relationships be obtained from indentation curves using conical and pyramidal indenters? *Journal of Materials Research*, 14:3493–3496, 1999.

[82] Hill, R. Lee, E. H. and Tupper, S. J. The theory of wedge indentation of ductile materials. *Proceedings of the Royal Society A*, 188A:273–289, 1947.

[83] Vandeperre, L. J. Giuliani, F. and Clegg, W. J. Effect of elastic surface deformation on the relation between hardness and yield strength. *Journal of Materials Research*, 19(12):3704–3714, 2004.

[84] Lawn, B and Wilshaw, R. Indentation fracture: principles and

applications. *Journal of Materials Science*, 10(6):1049–1081, 1975.

[85] Cook, R. F. and Pharr, G. M. Direct Observation and Analysis of Indentation Cracking in Glasses and Ceramics. *Journal of the American Ceramic Society*, 73(4):787–817, 1990.

[86] Li, X. D. and Bhushan, B. Micro/nanomechanical characterization of ceramic films for microdevices. *Thin Solid Films*, 340:210–217, 1999.

[87] Dub, S. N. and Maistrenko, A. L. *Fracture Mechanics of Ceramics 10: Fracture fundamentals, High-Temperature Deformation, Damage, and Design*, volume 10, chapter Reliability of Ceramics Fracture Toughness Measurements By Indentation. Kluwer Academic Publishers, Norwell, MA, U.S.A., 1992 edition, 1992.

[88] Lawn, B. R. and Marshall D. B. Hardness, Toughness and Brittleness: An Indentation Analysis. *Journal of American Ceramic Society*, 62(347-350), 1979.

[89] Lawn, B. R. Evans, A. G. and Marshall, D. B. Elastic/Plastic Indentation Damage in Ceramics: The Median/Radial Crack System. *Journal of the American Ceramic Society*, 63(9-10):574–581, September 1980.

[90] Bhat, G. Comment on "Elastic/Plastic indentation damage in ceramics: the median radial crack system". *Journal of American Ceramic Society*, 64(11):C165–C166, November 1981.

[91] Marshall, D. B. and Evans, A. G. Reply to "Comment on 'Elastic/Plastic indentation damage in ceramicsL the Median/Radial crack systems'". *Journal of American Ceramic Society*, 64(12):C–182–C–183, December 1981.

[92] Evans, A. G. and Charles, E. A. Fracture toughness determination by indentation. *Journal of American Ceramic Society*, 59(7-8):371–372, July 1976.

[93] Niihara, K. Nakahira, A. and Hirai, T. The effect of stoichiometry on mechanical properties of boron carbide. *Journal of American Ceramic Society*, 67(1):C–13–C–14, January 1984.

[94] Li, Z. Ghosh, A. Kobayashi, A. S. and Bradt, R. C. Indentation Fracture Toughness of Sintered Silicon Carbide in the Palmqvist Crack Regime. *Journal of the American Ceramic Society*, 72(6):904–911, 1989.

[95] Lewis, M. H. Fung, R and Taplin, D. M. R. Indentation plasticity and fracture of Si_3N_4 ceramic alloys. *Journal of Materials Science*, 16:3437–3446, 1981.

[96] Niihara, K. A fracture mechanics analysis of indentation-induced Palmqvist crack in ceramics. *Journal of Materials Science Letters*, 2:221–223, 1983.

[97] Jones, S. L. Norman, C. J. and Shahani, R. Crack-profile shapes formed under a Vickers indent pyramid. *Journal of Materials Science Letters*, 6:721–723, 1987.

[98] Bull, S. J. Page, T. F. and Yoffe E. H. An explanation of the indentation size effect in ceramics. *Philosophical Magazine Letters*, 59(6):281–288, 1989.

[99] Gong, J. Wu, J. and Guan, Z. Examination of the indentation size effect in low-load vickers hardness testing of ceramics. *Journal of the European Ceramic Society*, 19(15):2625–2631, November 1999.

[100] Tarakanian, M. L.Neumann, J. P. and Raymond, L. Determination of the temperature dependence of {100} and {112} slip in tungsten from Knoop hardness measurements. *American Society for Metals*, The Science of Hardness Testing and Its Research Applications:187–198, 1973.

[101] Hays, C. and Kendall, E. G. An analysis of Knoop microhardness. *Metallography*, 6(4):275–282, August 1973.

[102] Li, H. and Bradt, R. C. The effect of indentation-induced cracking on the apparent microhardness. *Journal of Materials Science*, 31(4):1065–1070, 1996.

[103] Machaka, R. Derry, T. E. Sigalas, I. and Herrmann, M. Analysis of the Indentation Size Efect in the Microhardness Measurements in B_6O. *Advances in Materials Science and Engineering*, 2011(Article ID: 539252), 2011.

[104] Gao, H. and Huang, Y. Geometrically necessary dislocation and

size-dependent plasticity. *Scripta Materialia*, 48(2):113 – 118, 2003.

[105] Fleck, N. A. Muller, G. M. Ashby, M. F. and Hutchinson, J. W. Strain gradient plasticity: Theory and experiment. *Acta Metallurgica et Materialia*, 42(2):475 – 487, 1994.

[106] Fleck, NA and Hutchinson, JW. A phenomenological theory for strain gradient effects in plasticity. *Journal of the Mechanics and Physics of Solids*, 41(12):1825 – 1857, 1993.

[107] Fleck, N. A. and Hutchinson, J. W. *Advances in Applied Mechanics*, volume 33 of *Advances in Applied Mechanics*, chapter Strain Gradient Plasticity, pages 295 – 361. Elsevier, 1997.

[108] Rashid, K. Al-Rub, A. and Voyiadjis G. Z. Analytical and experimental determination of the material intrinsic length scale of strain gradient plasticity theory from micro- and nano-indentation experiments. *International Journal of Plasticity*, 20(6):1139 – 1182, 2004.

[109] Ren, X. J. Hooper, R. M. and Griffiths, C. Indentation size effect inceramics: Correlation with H/E. *Journal of Materials Science Letters*, 22:1105–1106, 2003.

[110] Peng, Z. Gong, J. and Miao, H. On the description of indentation size effect in hardness testing for ceramics: Analysis of the nanoindentation data. *Journal of the European Ceramic Society*, 24(8):2193–2201, July 2004.

[111] Quinn, G. D. Green, P. and Xu, K. Cracking and the Indentation Size Effect for Knoop Hardness of Glasses. *Journal of the American Ceramic Society*, 86(3):441–448, 2003.

[112] Sangwal, K. Review: Indentation size effect, indentation cracks and microhardness measurement of brittle crystalline solids - some basic concepts and trends. *Crystal Research and Technology*, 44:1019–1037, October 2009.

[113] Ezis, A. Monolithic, fully dense silicon carbide material, method of manufacturing and end uses. US Patent No. 5372978, December 1994.

[114] Goldstein, J. I. *Scanning electron microscopy and X-ray microanalysis*. New York; KLondon: Plenum Press, 2003.

[115] Vickerman, J. C. Brown, A. and Reed, N. M. *Secondary Ion Mass Spectroscopy: Principal and Applications*. Oxford Science Publication, 1989.

[116] Vickerman, J. C. *Surface analysis: the principal techniques*. Wiley, 2nd edition, 2009.

[117] William, D. B. and Carter, C. B. *Transmission Electron Microscopy*. Springer, second edition, 2009.

[118] Zaspalis, V. and Kolenbrander, M. Mixing homogeneity and its influence on the manufacturing process and properties of soft

magnetic ceramics. *Journal of Materials Processing Technology*, 205(1-3):297–302, August 2008.

[119] Cullity, B. D. and Stock, S. R. *Elements of X-ray Diffraction*. Prentice Hall, 3 edition, 2001.

[120] Ruska, J. Gauckler, L. J. Lorenz, J. and Rexer, H. U. The quantitative calculation of SiC polytypes from measurements of X-ray diffraction peak intensities. *Journal of Materials Science*, 14(8):2013–2017, 1979.

[121] Mendelson, M. I. Average grain size in polycrystalline ceramics. *Journal of the American Ceramic Society*, 52(8):443–446, 1969.

[122] Sneddon, I. Boussinesq's problem for a rigid cone. *Cambridge University Press*, 44:492–507, 1948.

[123] N. Ur-rehman, P. Brown, and L.J. Vandeperre. *Evolution of the AlN Distribution during Sintering of Aluminium Nitride Doped Silicon Carbide*, volume 31, chapter Ceramic Engineering and Science Proceedings, pages 231–238. John Wiley & Sons, Inc., 2010.

[124] Slack, G. A. Tanzilli, R. A. Pohl, R. O. and Vandersande, J. W. The intrinsic thermal conductivity of AIN. *Journal of Physics and Chemistry of Solids*, 48(7):641 – 647, 1987.

[125] Yue, R. Wang, Y. Wang, Y. and Chen, C. SIMS study on the

initial oxidation process of AlN ceramic substrate in the air. *Applied Surface Science*, 148(1-2):73 – 78, 1999.

[126] Guillard, F. Allemand, A. Lulewicz, J-D and Galy, J. Densification of SiC by SPS-effects of time, temperature and pressure. *Journal of the European Ceramic Society*, 27(7):2725 – 2728, 2007.

[127] Pirouz, P. Demenet, J. L. and Hong, M. H. On transition temperatures in the plasticity and fracture of semiconductors. *Philosophical Magazine A*, 81(5):1207–1227, May 2001.

[128] Pharr, G. M. Oliver, W. C. and Harding, D. S. New evidence for a pressure-induced phase transformation during the indentation of silicon. *Journal of Materials Research*, 6(6):1129–1130, 1991.

[129] Clarke, D. R. Kroll, M. C. Kirchner, P. D. Cook, R. F. and Hockey, B. J. Amorphization and Conductivity of Silicon and Germanium Induced by Indentation. *Physical Review Letters*, 60:2156–2159, May 1988.

[130] Juliano, T. Gogotsi, Y. and Domnich, V. Effect of indentation unloading conditions on phase transformation induced events in silicon. *Journal of Materials Research*, 18:1192–1201, 2003.

[131] Williams, J. S. Chen, Y. Wong-Leung, J. Kerr, A. and Swain, M. V. Ultra-micro-indentation of silicon and compound semiconductors with spherical indenters. *Journal of Materials Research*, 14(2338-2343), 1999.

[132] Tabor, D. *The Hardness of Metals*. Oxford, London, 1951.

[133] Cheng, Y-T and Cheng, C-M. What is indentation hardness? *Surface and Coatings Technology*, 133:417–424, 2000.

[134] Samuels, L. E. An experimental investigation of the deformed zone associated with indentation hardness impressions. *Journal of the Mechanics and Physics of Solids*, 5(2):125–134, March 1957.

[135] Gupte, S. S. and Desai, C. F. Vickers hardness anisotropy and slip system in zinc (tris) thiourea sulphate crystals. *Crystal Research and Technology*, 34(10):1329–1332, December 1999.

[136] Bucaille, J. L. Stauss, S. and Felder, E. Determination of plastic properties of metals by instrumented indentation using different sharp indenters. *Acta Materialia*, 51(6):1663–1678, 2003.

[137] Capehart, T. W. and Cheng Y. T. Determining constitutive models from conical indentation: sensitivity analysis. *Journal of Materials Research*, 18(4):827–832, 2003.

[138] Swadener, J. G. George, E. P. and Pharr, G. M. The correlation of the indentation size effect measured with indenters of various shapes. *Journal of the Mechanics and Physics of Solids*, 50(4):681–694, 2002.

[139] Raffenielo, W. Plichta, M. R. and Virkar, A. V. Investigation

of phase stability in the system SiC-AlN. *Journal of American Ceramic Society*, 66(4):272–276, 1983.

[140] McClintock, F. A. and Argon, A. S. *Mechanical Behavior of Materials*. Addison-Wesley, New York, USA, 1966.

[141] Quinn, G. D. Patel, P. J. and Lloyd, I. Effect of loading rate upon conventional ceramic microindentation hardness. *Journal of Research of the National Institute of Standards and Technology*, 107(3):299–306, 2002.

[142] Vandeperre, L. J. Ur-Rehman, N. and Brown, P. Strain rate dependence of hardness of AlN doped SiC. *Advances in Applied Ceramics*, 109(8):493–497, November 2010.

[143] Bhakhri V. Wang, J. Ur-rehman, N. Ciurea, C. Giuliani, F. and Vandeperre L. J. Instrumented Nanoindentation Investigation into the Mechanical Behaviour of Ceramics at Moderately Elevated Temperatures. *Journal of Materials Research*, 27(1), January 2012.

[144] Amelinckx, S. Strumane, G. and Webb, W. W. Dislocations in Silicon Carbide. *Journal of Applied Physics*, 31(8):1359 –1370, August 1960.

[145] Vandeperre, L. J. Giuliani, F. and Clegg W. J. An analytical approach for relating hardness and yield strength for materials with high ratio of yield strength to Young modulus. In *Sympo-*

sium on Fundamentals of Nanoindentation and Nanotriboloy III, volume 841, pages 323–328, 2005.

[146] Hirst, W. The indentation of materials by wedges. *Proceedings of the Royal Society A*, 311:429–444, 1969.

[147] Dugdale, D. S. Wedge indentation experiments with cold-worked metals. *Journal of the Mechanics and Physics of Solids*, 2(1):14–26, 1953.

[148] Atkins, A. G. and Tabor, D. Plastic indentation in metals with cones. *Journal of the Mechanics and Physics of Solids*, 13:149–164, 1965.

[149] Fujita, S. Maeda, K. and Hyodo, S. Dislocation glide motion in 6H SiC single crystals subjected to high-temperature deformation. *Philosophical Magazine A*, 55(2):203–215, 1987.

[150] Frost, H. J. and Ashby, M. F. *Deformation mechanism maps: the plasticity and creep of metals and ceramics*. Oxford: Pergamon Press, 1982.

[151] Ohsawa, K. Koizumi, H. and Kirchner, H. O. K. The critical stress in a discrete Peierls-Nabarro model. *Philosophical Magazine A*, 69(1):171–181, 1994.

[152] Clegg, W. J. Vandeperre, L. J. and Pitchford, J. E. Energy changes and the lattice resistance. *Key Engineering Materials*, Key Engineering Materials (317-318):271–276, 2006.

[153] F Guiberteau, NP Padture, and H Cai. Indentation fatigue. A simple cyclic Hertzian test for measuring damage accumulation in polycrystalline ceramics. *Philosophical Magazine*, 1993.

[154] N.P. Padture and B.R. Lawn. Fatigue in ceramics with interconnecting weak interfaces: a study using cyclic hertzian contacts. *Acta Materialia*, 43(4):1609–1617, 1995.

[155] N.P. Padture and B.R. Lawn. Toughness properties of a silicon carbide with an in situ induced heterogeneous grain structure. *Journal of the American Ceramic Society*, 77(10):2518–2522, 1994.

[156] Slutsker, A. I. Sinani, A. B. Betekhtin, V. I. Kadomtsev, A. G. and Ordan yan, S. S. Hardness of microporous SiC ceramics. *Technical Physics*, 53(12):1591–1596, December 2008.

[157] E. Feilden-Irving and L. J. Vandeperre. Communita ejection in alumina. A personal conversation, June 2011.

A. Polytypes

Table A.1.: Table showing results of Polytypes calculations. All SPSed samples were sintered at 2100 °C and Hot Pressed at 2050 °C unless stated otherwise.

Sample	**15R**	**6H**	**4H**	**3C**
α-SiC powder	0	94.6	4.7	0.8
α-SiC, 3.75wt%AlN-HP-Dwells	0	29.7	70.3	0
α-SiC, 3wt%C, 3.75wt%AlN-SPS	1.3	94.2	4.4	0
α-SiC, 3wt%C, 2.5wt%AlN-SPS	0	85.9	14.1	0
α-SiC, 3wt%C, 2wt%AlN-SPS	0	81.7	18.3	0
α-SiC, 3wt%C, 1.5wt%AlN-SPS	0	73.7	24.4	1.9
α-SiC, 3wt%C, 0.75wt%AlN-SPS	0	80	20	0
α-SiC, 3wt%C, 3.75wt%AlN-HP-Dwells	0	72.2	27.68	0
α-SiC, 3wt%C, 2.5wt%AlN-HP-Dwells	0	38.3	67.7	0
α-SiC, 3wt%C, 0.75wt%AlN-HP-Dwells	0	89.8	10.2	0
α-SiC, 3wt%C, 3.75wt%AlN-HP-60	0	83.9	16.1	0
α-SiC, 3wt%C, 2.5wt%AlN-HP-60	0	82.6	17.4	0
α-SiC, 3wt%C, 0.75wt%AlN-HP-60	0	86.6	13.4	0
α-SiC, 3wt%C, 3.75wt%AlN-HP-30	0	77.8	22.2	0
α-SiC, 3wt%C, 2.5wt%AlN-HP-30	0	86.1	13.9	0
α-SiC, 3wt%C, 0.75wt%AlN-HP-30	0	87.4	12.6	0
α-SiC, 3wt%C, 3.75wt%AlN-HP-1850 °C	0	94.7	5.3	0
α-SiC, 3wt%C, 3.75wt%AlN-HP-1700 °C	0	95.5	4.5	0
α-SiC, 3wt%Y, 3.75wt%AlN-SPS	3.1	87.9	9	0

B. Densities Table

Table B.1.: Densities of sintered samples measured using Archemedes method. The values are relative to the theoretical densities of the compositions.

Sample	Relative Density
α-SiC, 3.75wt%AlN-HP-Dwells	96.8 ± 0.07
α-SiC, 3wt%C-HP-Dwells	65.6 ± 0.006
α-SiC, 3wt%C, 3.75wt%AlN-SPS	99.1 ± 0.01
α-SiC, 3wt%C, 2.5wt%AlN-SPS	98.6 ± 0.02
α-SiC, 3wt%C, 2wt%AlN-SPS	97.4 ± 0.03
α-SiC, 3wt%C, 1.5wt%AlN-SPS	97.2 ± 0.03
α-SiC, 3wt%C, 0.75wt%AlN-SPS	98.6 ± 0.02
α-SiC, 3wt%C, 3.75wt%AlN-HP-Dwells	97.4 ± 0.01
α-SiC, 3wt%C, 2.5wt%AlN-HP-Dwells	98 ± 0.03
α-SiC, 3wt%C, 0.75wt%AlN-HP-Dwells	88.3 ± 0.02
α-SiC, 3wt%C, 3.75wt%AlN-HP60	97.9 ± 0.03
α-SiC, 3wt%C, 2.5wt%AlN-HP60	97.3 ± 0.03
α-SiC, 3wt%C, 0.75wt%AlN-HP60	94.9 ± 0.06
α-SiC, 3wt%C, 3.75wt%AlN-HP30	97.1 ± 0.02
α-SiC, 3wt%C, 2.5wt%AlN-HP30	97.2 ± 0.05
α-SiC, 3wt%C, 0.75wt%AlN-HP30	96 ± 0.02
α-SiC, 3wt%C, 3.75wt%AlN-HP-1700	58.4 ± 0.02
α-SiC, 3wt%C, 3.75wt%AlN-HP-1850	75.2 ± 0.03
α-SiC, 3wt%Y, 3.75wt%AlN-SPS	99.2 ± 0.06

C. Hardness

Table C.1.: Table showing Hardness of all the samples. The hardness was measured using 1 Kg load on Vickers indenter converted into projected area (Berkovich).

Sample	Hardness (GPa)
α-SiC, 3.75wt%AlN-HP-Dwells	19.78 ± 1.52
α-SiC, 3wt%C-HP-Dwells	2.04 ± 0.22
α-SiC, 3wt%C, 3.75wt%AlN-SPS	29.17 ± 2.45
α-SiC, 3wt%C, 2.5wt%AlN-SPS	28.3 ± 1.28
α-SiC, 3wt%C, 2wt%AlN-SPS	25.85 ± 1.76
α-SiC, 3wt%C, 1.5wt%AlN-SPS	26.91 ± 1.11
α-SiC, 3wt%C, 0.75wt%AlN-SPS	27.7 ± 4.43
α-SiC, 3wt%C, 3.75wt%AlN-HP-Dwells	24.52 ± 1.52
α-SiC, 3wt%C, 2.5wt%AlN-HP-Dwells	24.73 ± 1.36
α-SiC, 3wt%C, 0.75wt%AlN-HP-Dwells	21.24 ± 1.44
α-SiC, 3wt%C, 3.75wt%AlN-HP60	29.71 ± 2.21
α-SiC, 3wt%C, 2.5wt%AlN-HP60	22.82 ± 1.71
α-SiC, 3wt%C, 0.75wt%AlN-HP60	26.94 ± 0.88
α-SiC, 3wt%C, 3.75wt%AlN-HP30	31.5 ± 4.72
α-SiC, 3wt%C, 2.5wt%AlN-HP30	24.3 ± 1.4
α-SiC, 3wt%C, 0.75wt%AlN-HP30	27.06 ± 1.35
α-SiC, 3wt%C, 3.75wt%AlN-HP-1700	1 ± 0.9
α-SiC, 3wt%C, 3.75wt%AlN-HP-1850	8.4 ± 3.6
α-SiC, 3wt%Y, 3.75wt%AlN-SPS	24.11 ± 1.21

Publications

List of papers published in various journals and conference proceedings during the course of Phd:

1. Ur-rehman, N Brown, P. and Vandeperre, L. J., Evolution of the AlN distribution during sintering of AlN doped SiC. Ceramic Engineering and Scence Proceedings. 31(5), 231-238 (2010).

2. Ur-rehman, N Brown, P and Vandeperre, L. J., The role of carbon in processing hot pressed aluminium nitride doped silicon carbide. Ceramic Engineering and Science Proceedings. 31(2), 27−34 (2010).

3. Vandeperre, L. J. Ur-Rehman, N. and Brown, P., Strain rate dependence of hardness of AlN doped SiC. Advances in Applied Ceramics, 109(8):493497, November 2010.

4. Ur-rehman, N Brown, P and Vandeperre, L. J., The Strain−Rate Dependence of the Hardness of AlN Doped SiC, Ceramic Engineering and Science Proceedings, 32, 11−19 (2011)

5. Bhakhri V. Wang, J. Ur-rehman, N. Ciurea, C. Giuliani, F. and Vandeperre L. J., Instrumented Nanoindentation Investigation into the Mechanical Behaviour of Ceramics at Moderately Elevated Temperatures. Journal of Materials Research, 27(1), 65-75, January 2012.